Clemson University
TigerPrints

All Theses Theses

12-2017

Design and Analysis of a Mechanical Driveline with Generator for an Atmospheric Energy Harvester

Sneha Ganesh
Clemson University

Follow this and additional works at: https://tigerprints.clemson.edu/all_theses

Recommended Citation
Ganesh, Sneha, "Design and Analysis of a Mechanical Driveline with Generator for an Atmospheric Energy Harvester" (2017). *All Theses*. 2794.
https://tigerprints.clemson.edu/all_theses/2794

This Thesis is brought to you for free and open access by the Theses at TigerPrints. It has been accepted for inclusion in All Theses by an authorized administrator of TigerPrints. For more information, please contact kokeefe@clemson.edu.

DESIGN AND ANALYSIS OF A MECHANICAL DRIVELINE WITH GENERATOR FOR AN ATMOSPHERIC ENERGY HARVESTER

A Thesis
Presented to
the Graduate School of
Clemson University

In Partial Fulfillment
of the Requirements for the Degree
Master of Science
Mechanical Engineering

---

by
Sneha Ganesh
December 2017

Accepted by:
Dr. John Wagner, Committee Chair
Dr. Yue (Sophie) Wang
Dr. Todd Schweisinger

ABSTRACT

The advent of renewable energy as a primary power source for microelectronic devices has motivated research within the energy harvesting community over the past decade. Compact, self-contained, portable energy harvesters can be applied to wireless sensor networks, Internet of Things (IoT) smart appliances, and a multitude of standalone equipment; replacing batteries and improving the operational life of such systems. Atmospheric changes influenced by cyclical temporal variations offer an abundance of harvestable thermal energy. However, the low conversion efficiency of a common thermoelectric device does not tend to be practical for microcircuit operations. One solution may lie in a novel electromechanical power transformer integrated with a thermodynamic based phase change material to create a temperature/pressure energy harvester. The performance of the proposed harvester will be investigated using both numerical and experimental techniques to offer insight into its functionality and power generation capabilities.

The atmospheric energy harvester consists of a ethyl chloride filled mechanical bellows attached to an end plate and constrained by a stiff spring and four guide rails that allow translational motion. The electromechanical power transformer consists of a compound gear train driven by the bellows end plate, a ratchet-controlled coil spring to store energy, and a DC micro generator. Nonlinear mathematical models have been developed for this multi-domain dynamic system using fundamental engineering principles. The initial analyses predicted 9.6 mW electric power generation over a 24 hour period for ±1°C temperature variations about a nominal 22°C temperature. Transfer

functions were identified from the lumped parameter models and the transient behavior of the coupled thermal-electromechanical system has been studied. A prototype experimental system was fabricated and laboratory tested to study the overall performance and validate the mathematical models for the integrated energy harvester system. The experimental results agree with the numerical analyses in behavioral characteristics. Further, the power generation capacity of 30 mW for a representative electrical resistance load and emulated rack input which correspond to 50 cyclic bidirectional temperature variations (~175 hours of field operation) validated the simulation models.

This research study provides insight into the challenges of designing an electromechanical power transformer to complement an atmospheric energy harvester system. The mathematical models estimated the behavior and performance of the integrated harvester system and establishes a foundation for future optimization studies. The opportunity to power microelectronic devices in the milliwatt range for burst electric operation or with the use of supercapacitors/batteries enables global remote operation of smart appliances. This system can assist in reducing/eliminating the need for batteries and improving the operational life of a variety of autonomous equipment. Future research areas have been identified to improve the overall system capabilities and implement the harvester device for real-world applications.

DEDICATION

This thesis is dedicated to my parents and my brother for always being there to support my career goals and dreams.

ACKNOWLEDGMENTS

This research project was a very important milestone at a personal level because I believe in sustainable and green energy technologies that do their part to prevent alarming rates of environmental degradation. I would like to thank everyone who has made this possible, including the Mechatronics Research Team at Clemson University. My advisor, Dr. John Wagner, has supported and guided my research and graduate education. He has always pushed to me to achieve my best and has helped me become more organized as a researcher. I would also like to thank my committee members, Dr. Schweisinger, and Dr. Wang, for their guidance and help in the evaluation of my thesis.

I am grateful to Michael Justice, who works in the machine shop with the Department of Mechanical Engineering. I have learned how to take designs from paper to the bench and identify solutions to production practicalities. I would also like to thank David Moline of the Electrical and Computer Engineering Department for his help with the generator tests and designs.

I am grateful to my parents for everything they have done in supporting my career goals. Lastly, I am forever indebted to my brother, Venkataraman Ganesh, for pushing me when I needed it the most and for being my best critic; it has made me a better person.

TABLE OF CONTENTS

Page

TITLE PAGE i

ABSTRACT ii

DEDICATION iv

ACKNOWLEDGMENTS v

LIST OF TABLES viii

LIST OF FIGURES ix

NOMENCLATURE LIST xiv

CHAPTER

I. BACKGROUND AND LITERAURE REVIEW 1

Introduction 1
Literature Review 4
Importance of Research 8
Research Goal and Hypothesis 9
Approach and Thesis Outline 10

II. CONVERSION OF ATMOSPHERIC VARIATIONS INTO ELECTRIC ELECTRIC POWER – DESIGN AND ANALYSIS OF AN ELECTRIC POWER GENERATOR SYSTEM 13

Introduction 14
Design of Energy Harvester 17
Mathematical Model 21
Numerical Results 35
Summary 42

III. DEVELOPMENT OF THE EXPERIMENTAL SYSTEM AND TEST BENCH DESCRIPTION 43

Table of Contents (Continued)

Page

Introduction 43
Experimental System Development 44
Test Bench Description 45

IV. LINEAR MODEL AND TEST OF AN ATMOSPHERIC ENERGY HARVESTER SYSTEM 60

Introduction 61
Atmospheric Energy Harvester System 65
Benchtop Experimental System 71
Numerical and Experimental Results 76
Summary 81

V. CONCLUSION AND RECOMMENDATIONS 82

Mathematical Models and Analyses 84
Experimental Results and Discussion 86
Recommendations 87

APPENDICES 90

A: Derivation of Transfer Functions for Harvester System 91
B: MATLAB Programs 98
C: Simulink Model 105
D: CAD Images of Power Transformer Components 110
E: Development of Encoder Circuit to Measure Generator Shaft Speed 113
F: LabVIEW Program for the Experimental DAQ and Control 115
G: Supplementary Graphs from Testing 118
H: Numerical Analysis – Case Studies on Design Parameters 120
I: Bill of Materials 124

REFERENCES 134

LIST OF TABLES

Table Page

1.1 Performance of Energy Harvesters 7

2.1 System Simulation Design Parameter Values and Units 38

4.1 Design Parameter Values in the Numerical and Experimental Study 75

I.1 Parts List for Fabrication of Drivetrain 124

I.2 Part List and Description of Mainspring with Barrel 128

I.3 Description of the DC Micro Generator 128

I.4 Parts List for Encoder Circuit Components 129

I.5 Parts List of Supplementary Items 130

I.6 Parts List for Machining Tools 132

LIST OF FIGURES

Figure Page

1.1 World Renewable Energy Consumption (quadrillion British thermal units), World Net Electricity Power Generation by Energy Source (trillion kWh) (Adapted from [1]) 2

2.1 Self-contained Drivetrain, Coil Spring, and DC Generator Assembly Model With Input Rack Displacement 17

2.2 Atmospheric Driven Ethyl Chloride Filled Mechanical Bellows with End Plate Displacement to Move Attached Rack [37] 19

2.3 Mechanical Gear Train, Mainspring, and Electrical Generator Schematic 21

2.4 Forces Acting on Bellows End Plate and Translational Rack 25

2.5 Elements of the Drivetrain with Bellows Expansion and Contraction Pathways 28

2.6 DC Generator Electrical Circuit 35

2.7 Dynamic Response of Energy Harvester – (a) Ambient Temperature and (b) Rack Displacement 39

2.8 Dynamic Response of Energy Harvester – (a) Spring Shaft Rotational Displacement and (b) Generator Torque Input for 'Hold' Duration of 24 Hours 40

2.9 Dynamic Response of Energy Harvester – (a) Generated Current and Corresponding Generator Shaft Rotation, and (b) Generated Power 41

3.1 Experimental Spring with Barrel 46

3.2 Spring Shaft Coupling 46

3.3 Rack and Pinion 47

3.4 One-Way Bearings Fitted Inside Gear Hub 47

List of Figures (Continued)

Page

3.5 Grooved Shaft Assembly with One-Way Bearing inside Gear with Set Screw 48

3.6 Retaining Ring 48

3.7 Mounted Pillow Block with Bearings 49

3.8 Experimental Plate 50

3.9 Plastic Insert and Rack 50

3.10 Cap Screw and Set Screw 50

3.11 Ratchet 51

3.12 Spring Wire to Hold Ratchet 52

3.13 DC Generator Set (borrowed from eBay) 53

3.14 Gear Shaft Coupling 53

3.15 Generator Mount/Housing 54

3.16 Linear Actuation Unit 56

3.17 Rack-Piston Interface 56

3.18 Pillars to Raise Electromechanical Assembly 57

3.19 Test System 57

3.20 Linear Potentiometer 58

3.21 Encoder Circuit 58

3.22 Data Acquisition and Control Board – NI SCB 68 59

4.1 Energy Harvester Device Overview 63

4.2 Micro-scale Atmospheric Energy Harvester Based on Linear Displacement Input 65

List of Figures (Continued)

Page

4.3 Energy Flow Diagram for the Atmospheric Energy Harvester 71

4.4 Experimental Prototype of the Drivetrain and Spring Assembly, and DC Generator Set Assembled onto a 15cmx15cmx0.6cm Aluminium Plate..... 72

4.5 Ethyl Chloride Filled Mechanical Bellows Assembly (20cmx25cmx20cm) which Generates End Plate Displacement 73

4.6 Numerical Results – (a) Bellows End Plate Response, x, to a Step Temperature, T, and (b) Spring Rotational Displacement, θ_6, for a Step Rack Linear Displacement, x, after θ_{max} 77

4.7 Numerical results – (a) Generated Current, i_a, versus Impulse Temperature Input, T, after θ_{max}, and (b) Power Generation Response, P, to an Impulse Temperature Input, T, after θ_{max}..... 78

4.8 Experimental Results – (a) Rack Input Profile, x, and (b) Generated Electric Power, P 79

A-1 First Order Polynomial Curve Fitting (Coefficients a_1 = 5088, a_2 = -1.353e06)..... 93

A-2 Second Order Polynomial Curve Fitting (Coefficients a_1 = 69.08, a_2 = -3.569e04, a_3 = 4.66e06)..... 93

C-1 High Level Diagram of Harvester System with Power Transformer 105

C-2 Second Level Diagram (Ethyl Chloride Filled Mechanical Bellows) 106

C-3 Second Level Diagram (Drivetrain, Spring, and DC Generator Assembly) 106

C-4 Third Level Diagram (Ethyl Chloride Behavior)..... 106

C-5 Low Level Diagram (Riedel Model)..... 107

C-6 Low Level Diagram (Bellows End Plate Dynamics)..... 107

C-7 Low Level Diagram (Rack and Pinion Dynamics)..... 108

C-8 Low Level Diagram (Gear Train Dynamics)..... 108

List of Figures (Continued)

Page

C-9 Low Level Diagram (Spring Dynamics) 109

C-10 Low Level Diagram (DC Generator Dynamics) 109

D-1 Aluminium Plate (6'' x 6'' x 0.25'') with Holes and Cuts to Accommodate Gears, Spring, and Generator Mount 110

D-2 Rack Gear 110

D-3 Pinion Gear (48 Teeth) with Drilled Center to Accommodate One-Way Bearing 111

D-4 Secondary Gear (60 Teeth) on Shaft B with One-Way Bearing Placed Inside 111

D-5 Shafts of the Compound Gear Train (From Top Left: A, B and C) 111

D-6 Mainspring Barrel and Key 112

D-7 Ratchet Assembly 112

D-8 DC Micro Generator 112

E-1 Rotary Encoder Experimental Circuit Key Components (Op-Amp and IR LED Emitter-Receiver Pair) 114

E-2 Encoder Circuit Diagram 114

E-3 Physical Encoder Circuit 114

F-1 Block Diagram of Visual Interface (VI) for Data Acquisition 115

F-2 Front Panel of Visual Interface for Data Monitoring 116

G-1 Encoder Output Voltage (V) vs Time (s) 118

G-2 Generated Voltage 119

G-3 Generated Current 119

H-1 Effect of Pinion Radius, r_1, on Generated Power, P 120

H-2 Effect of Gear Ratio, R_{56}, on Generated Power, P 121

List of Figures (Continued)

Page

H-3 Effect of Spring Coil Stiffness Rate, k_s, on Generated Power, P 121

H-4 Effect of Gear Ratio, R_{78}, on Generated Power, P 122

H-5 Effect of Equivalent Generation Circuit Resistance, $\check{R}$ on Generated Power, P 122

H-6 Power Generation Capacities using Superior Parameters from Design Case Studies and Varying Load Resistance, R_L 123

NOMENCLATURE LIST

a	Polynomial Coefficient (*Pa*)
A	Area (m^2), Riedel's Constant (-)
b	Damping Coefficient (*Ns/m*)
B	Riedel's Constant (-)
c	Viscous Damping (*Ns/m*)
C	Riedel's Constant (-)
D	Riedel's Constant (-)
E	Riedel's Constant (-)
f	Mathematical Functions of Reference Temperature (*Pa*)
F	Force (*N*)
G	Gear (-)
i	Current (*A*)
J	Inertia (kgm^2/rad)
k	Stiffness Rate (*N/m, Nm/rad*), Generator Constants (*Nm/A, V/rpm*)
L	Inductance (*H*)
m	Mass (*kg*)
n	Number of Moles (-)
N	Number of Gear Teeth (-)
P	Pressure (*Pa*), Power (*W*)
r	Gear radius (*m*)

Nomenclature List (Continued)

R	Universal Gas Constant (J/Kmol), Electrical Resistance (Ω), Generator Internal Gear Ratio
s	Laplace Operator (-)
t	Time (*s*)
T	Temperature (*K*)
V	Volume (m^3), Voltage (*V*)
x	Linear Displacement (*m*)
$\dot{x}$	Velocity (*m/s*)
β	System gain
Δ	Change or Variation (-)
μ	Mathematical Constant of Riedel's Constant A (-)
θ	Angular Displacement (*rad*)
τ	Torque (*Nm*), Time Constant (*s*)
ω	Angular Speed (*rad/s*)

Subscripts:

a	Armature
atm	Atmosphere
amb	Ambient
b	Viscous Damping, Bellows
bs	Bellows Spring
d	Bellows End Plate Damping

Nomenclature List (Continued)

e	Euler Number, Equivalent Value
ec	Ethyl Chloride
es	External Spring
G	Generator
GT	Gear Train
i	Gear Index
in	Input
j	Pinion Index, Internal Gear Ratio
L	Electrical Load
max	Maximum
out	Output
p	Bellows End Plate
r	Rack
s	Spiral Spring
sa	Shaft to Armature Gear Ratio
t	Generator Torque Constant
0	Reference Value

Superscripts:

*	Gear Ratio between Gear G_3 and G_4
~	Equivalent Value

CHAPTER ONE

BACKGROUND AND LITERATURE REVIEW

Introduction

The energy sector is an integral part of our everyday lives. World energy consumption is projected to rise 48% by 2040, which is majorly attributed to economic growth, rising population and developing infrastructures, transportation, and industrial demands [1]. A vast portion of the world energy demands are still met with nonrenewable energy sources such as fossil fuels, in spite of the growth in hydro, wind, solar and nuclear power. With rising environmental awareness on a global scale and concerns about energy security, implementation of stricter energy policies will likely reduce fossil fuel consumption by a considerable margin in the coming decades. International communities have agreed to develop dedicated green energy policies, provide better access to funding and higher cost-competitiveness for renewable energy technologies, as well as seek advancements in energy efficiency [2]. Therefore, to avoid energy shortfall while protecting the environment, the focus of the energy sector is shifting toward establishing renewable energy as the prominent source to satisfy customer energy demands.

Renewable energy is obtained from natural sources including solar, thermal, wind, and hydro that are continually replenished. Renewable energy is typically unlimited, with minimal stress to the environment, but the power density may be lower than fossil fuels. Solar photovoltaics, wind turbines, and hydropower dominate the renewable energy section of the power sector, adding to the global renewable power capacity. The market projections

for the renewable energy sector, shown in Figure 1.1 indicate substantial growth in this sector in the coming decades. Renewable energy sources are an efficient and environment friendly alternate to fossils for mitigating global energy demands and it is important to foster growth and research in this field.

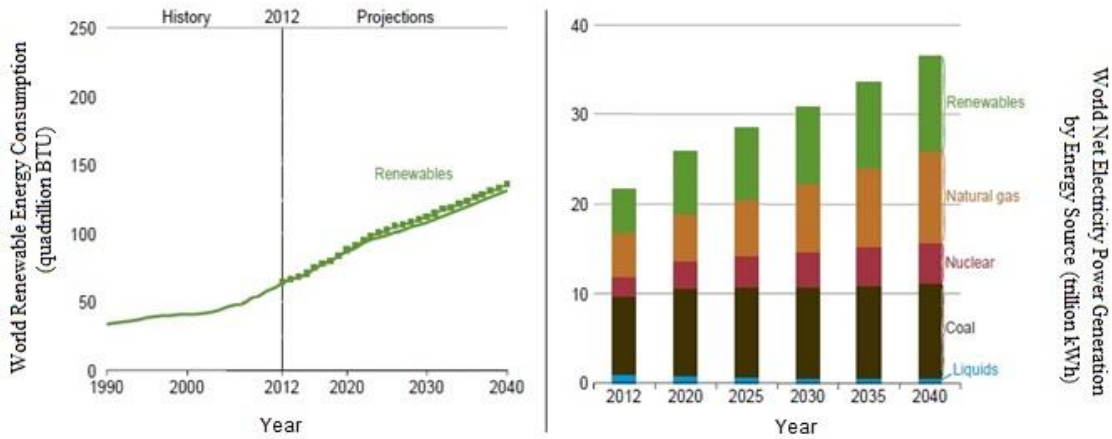

Figure 1.1: World Renewable Energy Consumption (quadrillion British thermal units), World Net Electricity Power Generation by Energy Source (trillion kilo Watt hours) (Adapted from [1])

The development and wide spread adoption of low power microelectronics, wireless nodes, and autonomous systems in a variety of applications have spurred the growth of energy harvesting technologies as the most attractive power [3,4]. Energy harvesting is the process through which ambient energy is harnessed and converted into useable electric power. Commonly used energy harvesting technologies capture thermal, vibrational, optical, and dynamic energy, and convert them into electricity [5]. Energy harvester technologies fall under the renewable energy category and are predominantly

used for low power applications, which typically consist of micro electro-mechanical systems (MEMS) and mass produced electronics that are used in a wide spectrum of applications. The most restrictive element of microelectronics and devices implemented in remote applications are batteries, which impose high maintenance requirements and adversely affect the efficiency and operating lives of such equipment. Considering the several disadvantages associated with battery operated devices, energy harvesting technologies are increasingly replacing or supplementing batteries, catering to the power demands of microelectronics and smaller electrical devices [6]. Energy harvesters improve the power efficiencies of such devices, rendering them self-sufficient with reduced maintenance requirements. Energy storage is also an active research area in energy harvesting and is crucial to the development of devices using energy harvesters, to accommodate for storing any excess power that is generated and/or assist in the operation of certain energy harvesters that may not be capable of delivering sufficient power continuously. In general, research and development in energy harvesting technologies is crucial in its contribution to alleviate energy demands and environmental concerns.

Literature Review

To explore the current trends and technologies in energy harvesting with respect to low power applications, articles and previous studies are briefly reviewed in this section. There are several ambient energy sources available for energy harvesting. Major energy sources include solar, thermal, vibrational, dynamic, and hybrid energy.

Solar energy is currently utilized for both large scale applications and in microelectronic operation. There are two methods of utilizing solar energy—solar thermal generation (large scale) and photovoltaic energy harvesting (low power). Photovoltaic systems have proven to be very reliable energy harvesting technologies that are largely employed in microelectronics applications. In this type of harvesting the solar cells convert sunlight directly into electricity in accordance with the photovoltaic principle, with power densities typically ranging between 10 μW to 15 mW/cm^3 [7]. Although it has been established as a major renewable energy contributor in the market, there has been constant progress in this field with respect to materials, cost-effectiveness, energy efficiencies, and technology over the last several decades [8-10]. On a global scale, solar energy is one of the most widely used renewable energy source, but has several limitations associated with it due to its dependencies on weather patterns, installation site and specific design factors (angle to sun, humidity, etc.), and associated energy storage capacity; and low conversion efficiencies, complex production methods, and limited life.

Vibrational or electromechanical energy harvesters are mainly divided into piezoelectric, electrostatic and electromagnetic technologies. Piezoelectric harvesters generate electricity from mechanical stress to piezoelectric materials. Such harvesters are largely employed in a variety of microelectronics and there is active research in this field [11-14] due to its wide scope of applications including piezoelectric harvesting for Bio MEMS applications as shown by Ramsey and Clark [15] as well as wireless sensor nodes [16]. As piezoelectric harvesters mature as an attractive energy scavenging technology with the development of materials and designs [17-19], they incur several limitations including

low conversion efficiencies, limited operational frequencies, dependence on the input forces and orientation, extensive supplementary circuitry/storage and low power density in the range of microwatts across a smaller volume [20].

Electrostatic harvesters operate on capacitive properties of dielectric materials. Mechanical vibration induces a structure deformation and is converted to electricity through the variation of capacitance. There are two main categories of electrostatic energy harvesters—electret-free and electret-based—where the main difference between the two types is the material and its response [21]. Advancements in MEMS technologies are used in enhancing the performance of electrostatic harvester systems. Wang and Hansen [22] explored a variable gap MEMS electrostatic energy harvester with improved output at a broader frequency band. More recently, Tao *et al.* [23] proposed a performance improvement to electret-based harvesters using a sandwich-structured MEMS configuration. In comparison to piezoelectric and electromagnetic energy harvesters, electrostatic devices offer the advantages of lower costs and easier material accessibility. Electrostatic energy harvesters have several limitations such as low frequency bandwidth, material constraints, and integration, although their ability to withstand higher temperatures is an important advantage.

Electromagnetic energy harvesters utilize the principles of magnetism to convert mechanical energy into electricity. Induced voltages in electromagnetic devices are - impractical without supporting voltage amplifying circuitry [24]. A polymer beam structure attached to a PCB with multiple copper coils was developed by Yang *et al.* [25] and it was shown that such a harvester can be used over multiple vibrational frequencies

generating up to 3.2 μW of power. Gupta *et al.* [26] studied harvesting electromagnetic energy from stray AC power lines that could generate 1-2 mW of power with an efficient power conversion circuit. Due to the low power outputs and inefficient conversion of electromagnetic energy harvesters, a lot of development is still required to establish this technology as a dependable ambient energy scavenging device.

Thermal energy harvesters and thermoelectric devices are well established energy scavenging systems that are currently being implemented for a variety of applications ranging from simple consumer electronics to complex vehicle and industrial environments. Typical thermal energy harvesters utilize the Seebeck effect in which semiconductors act as the harvesting and power generation plant. Such harvesters are constrained largely by the requirements of large temperature gradients and exposed area, as well as complex design and production for practical uses [27]. Thermoelectric generators for large temperature gradients are widely implemented and there is active research to improve the conversion efficiency [28-30]. More recently there is also a lot of interest in the development of solar thermal energy coupled with photovoltaic thermoelectric generators [27] as well as pyroelectric generators in work similar to that done by Zhu *et al.* [31]. Thermal energy harvesters investigated for harvesting body heat and motion generate sufficient energy to operate wearable sensors, electronics, and medical equipment [32-34]. The major drawback of thermal energy harvesters is the low thermal to electric conversion efficiency irrespective of the operating principles. There are limited applications where such harvesters are practically utilized to scavenge natural or ambient temperature/pressure differences [35-38]. There is a lack of research in utilizing environmental

temperature/pressure variations from ambient energy and effectively converting them into usable electric power in spite of the potential for such devices.

A summary of the power generation capacities of common energy harvesters is presented in Table 1.1, borrowing information from the comprehensive literature sources reviewed in this study.

Energy Source	Power Density/Performance
Acoustic Noise	0.003 – 0.96 μW/cm^3
Ambient Light	0.1 – 100 W/cm^2
Ambient Pressure/Temperature	6 – 21 mJ
Electromagnetic	μW – 2 mW
Electrostatic	90 pW – 25 mW
Human Body	0.1 – 10 mW
Piezoelectric	200 μW
Radio Frequency	1 μW/cm^2
Solar	100 mW/cm^2
Thermal	60 μW/cm^2

Table 1.1: Performance of Energy Harvesters

Importance of Research

The current global environmental concerns emphasize the need for 'green' energy technologies. Although a variety of harvesters (piezoelectric, thermoelectric, solar, etc.) are actively being used, the power generation capacities are considerably low for collecting and utilizing naturally occurring (or artificially generated) small environmental fluctuations. There are several disadvantages associated with current energy harvester technologies arising from material limitations, design constraints, operational ranges, and irregular source availability. Thermal energy may be considered an indefinitely available energy source given the daily heating and cooling cycle of the earth's surface by the sun. This renders it as one of the most attractive options for energy harvesting. Therefore, it is important to alleviate the low conversion efficiencies of current temperature/pressure-based harvester devices. Efficiently capturing and converting ambient temporal variations into useable energy has long been used in the Atmos clock, which is one of the earliest and most innovative practical applications of an ambient energy harvester. Borrowing from the operational concepts—vapor phase change pressure response and mechanical transmissions—from the Atmos clock, an electromechanical device integrated to a vapor based energy harvester has been innovated, studied, and tested for its functionality and power generation performance.

Research Goal and Hypothesis

The fundamental goal of this research is to investigate the performance of an electromechanical power transformer unit attached to a Phase Change Material (PCM) based energy harvester to collect and convert small atmospheric variations (pressure and temperature) into useable electric power. Useable electric power was considered to be in the range of milliwatts for this study. Specific objectives of this study were to determine the design and development of the electromechanical assembly, establish mathematical models for the harvester device, and analyze the system behavior through dynamical simulations. Though this system has been developed targeted at implementing the proposed device to operate standalone microelectronics, this work is limited to development and analyses of the concept and establishing the electric power potential of the proposed device. The research hypothesis is that the proposed device can generate sufficient power to operate a microelectronic circuit or equivalent load.

There are two main important aspects to note in this study. First, the ethyl chloride vapor filled bellows used as the energy harvester in this study is very capable of generating pressure outputs for very low ambient thermal changes sufficient enough to be captured and converted to useable electric power, given the very low power requirements of modern microelectronics. Although, for this research, ambient thermal fluctuations analogous to those expected in regions with high diurnal temperature variations have been used to investigate the power generation capacity of the harvester for a 24 hour harvesting period. Furthermore, the atmospheric pressure was assumed to be constant in this study and the

experimental prototypes have been scaled to accommodate testing in controlled laboratory environments to study the fundamental operation and power generation capabilities of the system. Therefore, the environment as well as the design variables are not necessarily optimal.

Approach and Thesis Outline

Numerical and experimental techniques have been used in this study to establish a basic understanding of the power transforming, harvester system. Borrowing inspiration from mechanical clock operation, mechanisms have been identified for the electromechanical power transformer unit to effectively utilize the bellows linear motion occurring from phase change of the ethyl chloride vapor in response to temperature differences.

Mathematical equations (ordinary differential equations and algebraic ideal gear relations) have been developed using classical dynamics and Laplace/continuous-time models have been used in simulation and analyses on Mathworks software MATLAB/Simulink. Transfer functions were developed from the dynamical equations and step response plots were studied to analyze the transient characteristics of the multi-domain system.

A prototype of the power transformer unit was fabricated and scaled for easier benchtop experimental testing. Analogous actuation corresponding to the operating environment of the standalone system was identified and sensors were implemented to

record crucial parameters in tests. National Instruments equipment (NI SCB 68) and software (LabVIEW) were used for data control, data acquisition, and visualization. The system was subject to multiple experimental cycles, experimental data was collected, and the performance of the system was studied.

So far, Chapter 1 has provided an understanding of the background and motivations for this study, the goals and hypotheses for this research, and the approach used in solving the research problem. The subsequent sections of this thesis provides details involving the methods used in the study and test of the proposed harvester device.

First, Chapter 2 discusses the development of the physical system and the associated mathematical models. Detailed discussions of the components in the electromechanical power transformer and three-dimensional Computer Aided Design (3D CAD) models are provided. Equivalent free body diagrams, operational schematics, and circuit diagrams are provided with detailed modeling of the dynamical system equations. With a defined set of design parameters, initial analysis results of the dynamical simulation are presented and the performance of the proposed harvester system is discussed. Based on the design and analysis, further investigations are proposed and the importance of the results of the research are discussed.

The next step in the research was to develop an experimental system that can be tested and used to validate the numerical models. Chapter 3 discusses the development of the experimental subsystems for the device, focusing on a standalone electromechanical power transformer unit. A detailed test bench description used to study the experimental

prototype is provided including accompanying sensor circuitry, data acquisition, and control.

Chapter 4 discusses control system designs for describing fundamental relationships among the multi-domain elements involving the harvester and corresponding transient behavioral analyses of the dynamic system. Energy flow in the system is also highlighted and brief explanations for the experimental systems and test bench are given. The experimental results from testing the standalone electromechanical unit is presented and the performance of the system is discussed. Finally, the potential of the overall system is considered with its limitations, and possible advances to the system are proposed.

Chapter 5 concludes the study and its results. Recommendations for future work are suggested to automate the design as well as to improve the efficiency and application scope of the ambient energy harvester.

The Appendix expands further on the detailed understanding of the approach, methods, software codes, and dynamical models used in the study. Descriptions of supporting equipment and supplementary information about the experimental system are provided.

CHAPTER TWO

CONVERSION OF ATMOSPHERIC VARIATIONS INTO ELECTRIC POWER – DESIGN AND ANALYSIS OF AN ELECTRIC POWER GENERATOR SYSTEM

Given its abundant availability, ambient thermal energy harvesting has the potential to power standalone microelectronic systems. The challenge in efficiently harvesting temperature and pressure variations is the low thermal to electric conversion ability of current harvesters. Most thermal harvesters require high temperature gradients. This paper presents the design, analysis, and implementation of an energy harvesting system that effectively harnesses naturally occurring temperature variations using ethyl chloride filled mechanical bellows. A mechanical drivetrain amplifies the bellows motion and a coil spring stores the potential energy. This energy is periodically released and converted into useable electric power by a DC generator. A series of mathematical models are developed and accompanying numerical analyses completed on the harvester system. For a low frequency sinusoidal temperature cycle of ±1°C about 22°C, 9.6 mW of electrical power was produced using a 1.5V micro DC generator for a 24 hour harvesting period. The power generation capacity of the proposed harvester is sufficient to indefinitely operate low power sensors and microelectronics in environments with small temperature gradients.

Introduction

The process of harnessing or "capturing" energy from ambient sources that are natural or artificial, and converting it to useable electric power is referred to as energy harvesting. Strict environmental regulations and rising interest in power capability of electronic devices, wireless sensor networks and autonomous devices have created a rising market for energy harvesting technologies. Currently, mass manufactured energy harvesting devices are targeted to run a range of low-power and mid-power electronic equipment. Energy harvesting allows implementation of self-sustaining, portable smart devices that have increased life and minimal maintenance requirements [39]. These energy harvesters can facilitate the use of smart computers, low power sensors [40] and LED lighting systems in remote regions throughout the world with minimal battery storage requirements. Ideally energy harvesters are compact, miniature systems that can be integrated into devices without significant structure or space requirements. Advanced material technologies, micro-manufacturing and three dimensional (3D) printing have enabled the development of micro components that satisfy functional requirements, at lower costs. Energy storage techniques have also received considerable attention in offering dense power capacities for uninterrupted power when coupled with energy harvesting systems.

Commonly used piezoelectric, electrostatic and electromagnetic harvesting devices have found applications in low-power personal devices. Similarly, ambient temperature variations can be harvested for electric power generation but at a lower frequency

consistent with natural cyclical behaviors. Thermal energy harvesters have the advantage of power scalability but the disadvantage of space requirements. Typical thermoelectric harvesters operate on the Seebeck effect and produce very small voltages [41]. Some thermoelectric harvesters studied for low-power autonomous electronics were observed to be inefficient in converting large temperature gradients into useable electric power [42]. One approach to increase the power output is to use vapor pressure changes to harvest atmospheric energy (pressure and temperature). The proposed design incorporates an intermediate mechanical drivetrain linked to a coiled spring storage system between a thermal driven bellows and an electric generator. J. L. Reutter patented a mechanism for converting temperature and pressure variations of a vapor into mechanical motion in 1928, which was implemented in the Atmos Clock, and J. Lebet [43] reviewed the development of the atmospheric clock. In 1934, the power generation capacities and performance of the clock designs were also extensively discussed [44]. Ali *et al.* [37] used an ethyl-chloride filled mechanical bellows with a return spring to harness atmospheric temperature variations. The resulting mechanical motion of the bellows, due to the thermodynamic behavior of the vapor, is slow and irregular since it follows the thermal variations. It was unable to effectively couple energy directly into a micro generator [45]. Therefore, the proposed system is connected to an energy storage device which is then interfaced to the micro generator for electric power production. The proposed energy harvester is versatile in that the electric generator has been decoupled from the energy harvester, to allow accumulation of mechanical energy from multiple atmosphere cycles and then released for a controlled burst of electrical power production. The research problem is to identify if

small temperature and pressure gradients can be harvested and efficiently used to power microelectronics through a coupled electric power generator set.

The renewable energy device consists of an ethyl chloride filled mechanical bellows which is linked through a mechanical drivetrain to store energy from low frequency temperature variations in a coil spring over a defined time period. The mechanical drivetrain serves two purposes. First, the translational motion of the bellow's end plate is converted into rotational motion that is accommodated by the storage element (e.g., coil spring) [36]. Second, the gear ratios amplify the displacement to maximize the potential energy stored given the large bellow's force. The release of the stored potential energy in the spring winding is controlled and transferred to a DC generator to provide sufficient voltage and current for battery charging. A 'hold and release' ratchet mechanism periodically engages and disengages to isolate and engage the DC generator circuit and the storage component. The design of the drivetrain, spring and generator (refer to Figure 2.1), may be optimized into a compact and portable unit with size scalability to accommodate bellows of varying sizes.

The feasibility of attaching an electric generator with an accompanying mechanical driveline, to the atmospheric sensitive bellows will be evaluated through studies based on dynamical models in MATLAB/Simulink. The remainder of this section describes the energy harvester system in terms of the mechanical bellows, drivetrain and coil spring assembly, and electrical generator, provides a comprehensive lumped parameter system mathematical model, and representative numerical results which is followed by the conclusion.

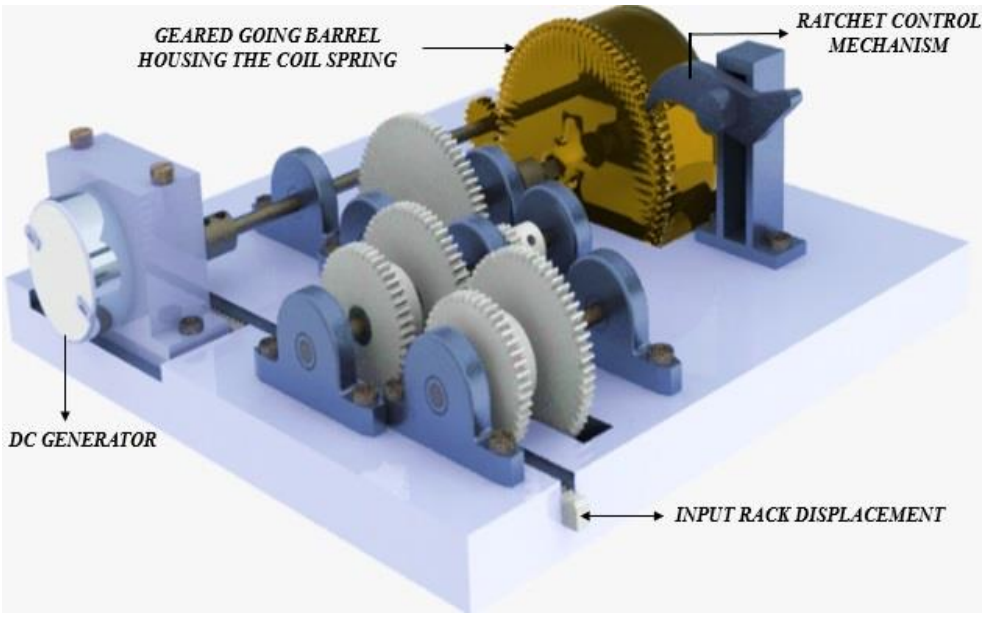

Figure 2.1: Self-contained Drivetrain, Coil Spring and DC Generator Assembly Model with Input Rack Displacement

Design of Energy Harvester

The concept of using an ethyl chloride filled mechanical bellows to harvest atmospheric temperature and pressure variations with conversion to useable mechanical energy was first implemented in Atmos Clocks. Ethyl chloride is a stable saturated gas that has a very low boiling point of 12.3°C and shows high pressure variations in phase change [46]. Similar to the functioning of the Atmos movement, the bellows is a hermetically sealed canister, which allows the vapor to expand and contract for minute variations in temperature, as low as 1°C.

To maximize the motion capture when the bellows expands and contracts, a mechanical drivetrain is designed to convert the oscillatory translational displacement into

rotational motion to wind a coil spring. The compound gear train design features a rack and dual pinion gears. The coil spring is wound in the same direction regardless of the direction of the rack motion through the utilization of unidirectional (one-way) bearings. Lighter materials were chosen for the drivetrain components to reduce its inertia. The storage element (coil spring) stiffness was estimated based on available system torque.

A. Mechanical Bellows

A pressure difference between the surrounding atmosphere and the ethyl chloride due to external temperature and pressure variations produces changes in bellows' length [47]. The bellows system (shown in Figure 2.2) was attached within two plates; the motion of one of which was fixed while the other (end plate) was free to travel along guide rails. An external spring was inserted to maintain an equilibrium position and restore the end plate to its initial location. The end plate moves back and forth allowing for the expansion and contraction of the vapor in the bellows, providing the mechanical equivalent of the work done by the vapor due to the temperature change. The reader is referred to Ali *et al.* [37] for further details regarding the bellows design.

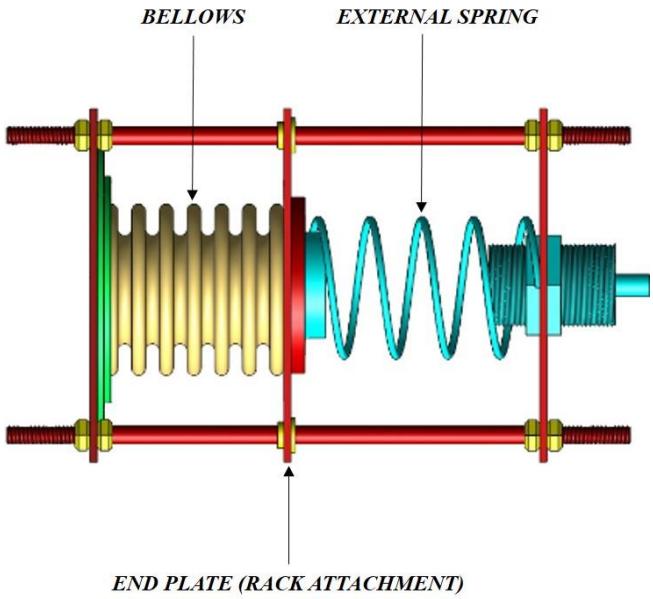

Figure 2.2: Atmospheric Driven Ethyl Chloride Filled Mechanical Bellows with End Plate Displacement to Move Attached Rack [37]

B. Drivetrain and Coil Spring Assembly

The mechanical drivetrain consists of six spur gears on parallel shafts connected to a torsional spring that acts as the energy storage system and drives the power generation unit. The storage unit consists of the torsional spring wound through a shaft or key, linked to a barrel gear. Figure 2.3 depicts all of the components in the drivetrain and spring assembly. The rack, attached to the bellows' end plate, is subject to the external force from the bellows contraction and expansion. This bidirectional translational motion is converted to rotational motion of the two pinion gears (G_1 and G_2). The gears, G_1, G_2 and G_4 are mounted on unidirectional bearings such that the overall motion transmitted across the drivetrain is only in the direction of the spring winding. The meshing of gears G_3 and G_4

enable the transmission of unidirectional rotation at mainspring shaft for the change in direction of the bellows motion.

When the rack moves in the direction of torque transmission on shaft A, gear G_3 on shaft B is in free spin while gear G_4 remains disengaged. In the other direction, the gears on shaft B are engaged while gear G_1 is in free spin. Concurrently, gear G_3 engages gear G_4 in the same direction as before (i.e. direction of the spring winding). The unidirectional bearing on gear G_4 now engages shaft A to transmit motion to wind the spring. The 'hold and release' mechanism (pawl) holds gear G_7 of the mainspring while it is being wound, preventing release of the stored energy till the desired time. Once sufficient amount of potential energy is stored, the release mechanism allows the gear G_7 to rotate. Gear G_7 then meshes with gear G_8, which is linked to the generator shaft, to produce electric power via the DC generator. An additional unidirectional bearing on gear G_8 can be used to prevent the backlash during spring release. By design, the motion of the rack is restricted by a stiff linear spring, k_r. The rotation of the spring coil is restricted by its torsional spring constant, k_s. The release mechanism can be solenoid operated or controlled manually.

C. Electrical Generator

The linear micro generator or load device [48] inserted into this system, is rigidly attached to the shaft secured to gear G_8. As the spring unwinds, the barrel gear G_7 meshes with gear G_8. A cylindrical shaft coupling transmits the rotational motion of gear G_8 to the DC generator, exciting the coil set inside the generator. This coil rotates between permanent magnets inducing an electromagnetic force, hence producing a current in the load circuit.

The critical design parameters contributing to the power output magnitude from the electrical subsystem are the gear ratio, R_{78}, and the generator constants, k_b and k_t.

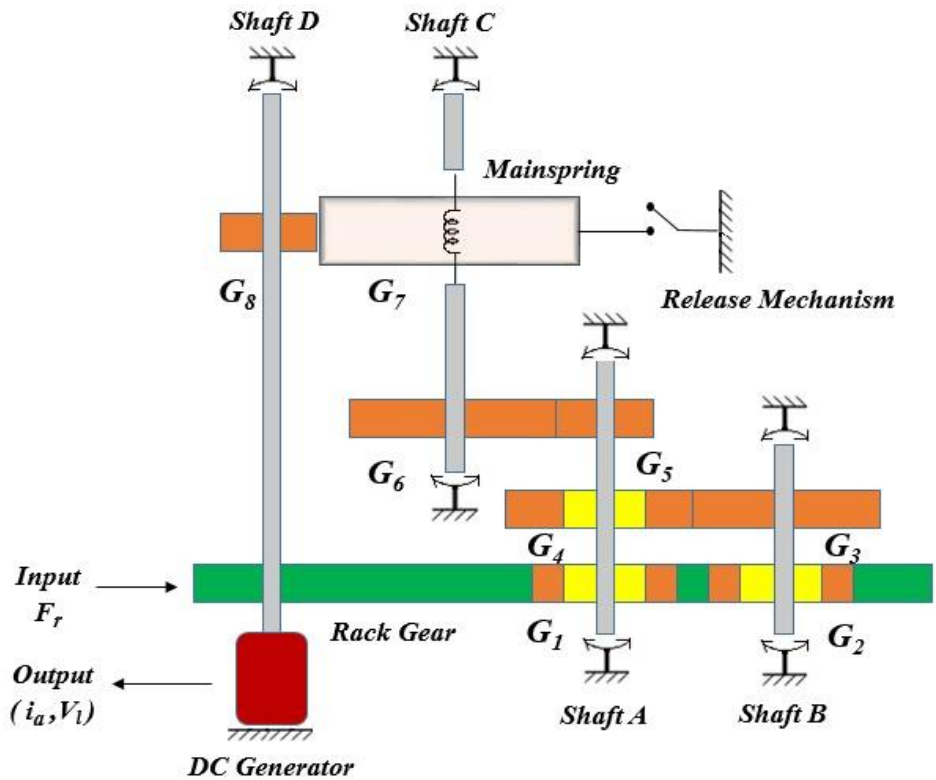

Figure 2.3: Mechanical Gear Train, Mainspring, and Electric Generator Schematic

Mathematical Model

A lumped parameter mathematical model can be derived to describe the dynamics of the energy harvester system. The process may be divided into three sections – thermodynamics, mechanical dynamics and electrical dynamics.

A. Thermodynamics – Bellows' Force

The displacement of the bellows' end plate, and hence the rack, depends on the total force output from the bellows due to the changing vapor pressures as a function of temperature variations. The thermodynamic behavior of the bellows was modeled based on the following assumptions:

A1: Ambient temperature variation was modelled as a sinusoidal wave whose amplitude and frequency may be experimentally defined.

A2: No ethyl chloride leakage occurs from the bellows.

A3: Frictional effects are minimal and may be lumped with viscous damping effects.

A4: External and bellows springs exhibit linear behavior.

A5: No heat loss exists between the bellows and the atmosphere (i.e., temperature inside and outside the bellows is equal).

A6: Ethyl chloride is subject to sufficient pressure at initial charge for both liquid and gas to exist in the bellows [35].

A7: No trapped air exists inside the bellows from the initial fluid charge.

The partial vapor pressure, P_{ec}, of the ethyl chloride in the bellows is defined using Riedel's equation [49] as

$$P_{ec} = e^{(A+\frac{B}{T}+ClnT+DT^{E})} \tag{2.1}$$

where *A*, *B*, *C*, *D*, *E* are Riedel's constants and *T* is the ambient temperature. When the liquid in the bellows has completely vaporized, the ethyl chloride exhibits ideal gas behavior and the gas pressure can be given by

$$P_{ec} = \frac{nRT}{V_b} \tag{2.2}$$

The parameter *n* denotes the number of moles of the gas, *R* is the universal gas constant, *T* is the temperature of the gas, and V_b is the volume of the bellows gas.

If the surface area of the end plate of the bellows is given by A_p, then the driving force, F_{ec}, exerted on the bellows end plate due to the ethyl chloride pressure becomes

$$F_{ec} = A_p P_{ec} \tag{2.3}$$

The force, F_{atm}, due to the atmospheric pressure, P_{atm}, acting on the bellows surface area is given by

$$F_{atm} = A_p P_{atm} \tag{2.4}$$

B. Translational Dynamics of Bellows End Plate

The bellows end plate motion occurs as a result of the bellows length variation due to changes in the vapor pressure. This dynamic behavior is dependent on the system forces as shown in Figure 2.4. The bellows' structure also acts as a linear spring that exerts a force, F_{bs}, which can be expressed as

$$F_{bs} = k_{bs} x \tag{2.5}$$

One end of the bellows is fixed while the end plate is attached to an external spring. During the expansion and contraction of the bellows, the force exerted by the external restoring spring, F_{es}, acting against the end plate motion is given by

$$F_{es} = k_{es}x \tag{2.6}$$

The moving end plate encounters viscous damping force, F_d, due to the translational motion along the four structural supports so that

$$F_d = c\frac{dx}{dt} \tag{2.7}$$

An external force, F_r, is exerted on the bellows end plate and modelled as a very stiff spring that allows the rack to move independent of the plate displacement. The dynamics of the end plate can then be described as a second-order mass-damper-spring system which produces a displacement, $\boldsymbol{x}$, such that

$$m\frac{d^2x}{dt^2} + c\frac{dx}{dt} + (k_{es} + k_{bs})x = A_p(P_{ec} - P_{atm}) - F_r \tag{2.8}$$

A small change in the ambient temperature will result in a vapor pressure change which is converted into a mechanical force and subsequent displacement by the bellows.

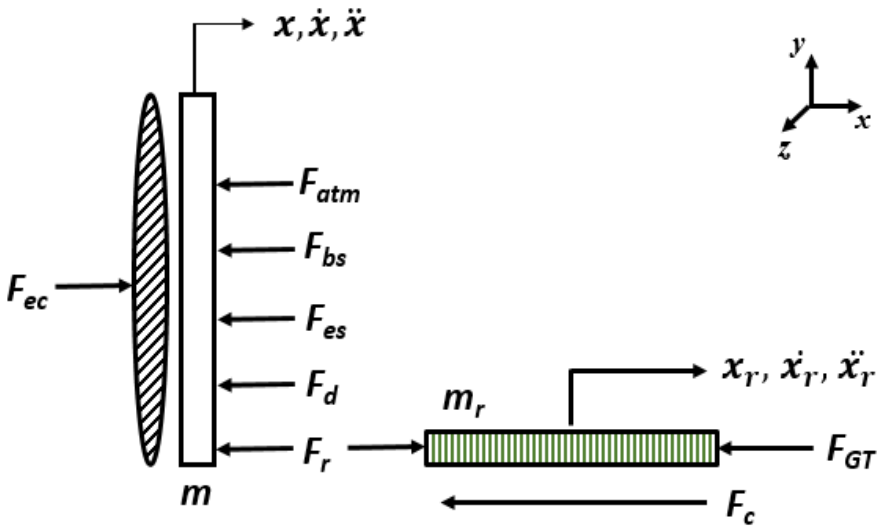

Figure 2.4: Forces Acting on the Bellows End Plate and Translational Rack

C. Mechanical Dynamics of the Rack and Gear Train

The rack can be modelled as a second order mass spring damper system that accepts the bellow force as the input while amplifying the resulting motion. The dynamic equations may be derived based on the following assumptions:

A8: No mechanical losses occur at the interface between the rack and bellows end plate.

A9: Drivetrain transmission losses are negligible.

A10: Individual gears are ideal.

A11: Unidirectional bearings have zero slip and no transmission losses when engaged or under free spin.

A12: Moments of inertia and accelerations of the rotational elements are negligible.

A13: Coiled mainspring exhibit linear behavior.

A14: Sign of rotational displacement and velocity are positive in bellows expansion and negative in contraction.

The rack force, F_r, considers the stiffness of the connecting interface, k_r, and the displacement difference between the rack and the bellows such that

$$F_r = k_r(x - x_r) \tag{2.9}$$

Similarly, the viscous damping force, F_c, due to the motion of the rack within the machined groove in the plate can be expressed using the damping coefficient of the rack, c_r, and rack speed such that

$$F_c = c_r \frac{dx_r}{dt} \tag{2.10}$$

Let the variable F_{GT} denote the force acting on the rack due to the gear train. Therefore, using (2.9) and (2.10), the mechanical dynamics of the rack becomes

$$m_r \frac{d^2x_r}{dt^2} + c_r \frac{dx_r}{dt} + k_r x_r + F_{GT} = k_r x \tag{2.11}$$

The translational rack motion triggers the rotational displacement of the drivetrain elements. The angular displacement and torque of gears G_1 and G_2 are functions of the gear radii, r_j, and rack displacement, x_r. The rotational velocities and displacements of the pinion gears, ω_j and θ_j, can be written as

$$\omega_j = \frac{1}{r_j}\left(\frac{dx_r}{dt}\right),\ \theta_j = \left(\frac{x_r}{r_j}\right);\ j=1, 2 \tag{2.12}$$

The force acting on the rack due to the gear train, F_{GT}, may be expressed in terms of the gear torque, τ_j, and gear radius as

$$\mathrm{F_{GT}} = \begin{cases} \frac{\tau_1}{r_1}, \frac{dx_r}{dt} \geq 0 \\ \frac{\tau_2}{r_2}, \frac{dx_r}{dt} < 0 \end{cases} \tag{2.13}$$

The algebraic drivetrain kinematics can be explicitly described by the gear ratio, R_i, which relates the angular velocities, gear radii, number of teeth, N_i, and torques as

$$R_i = \frac{\omega_{in}}{\omega_{out}} = \frac{\theta_{in}}{\theta_{out}} = \frac{r_{out}}{r_{in}} = \frac{N_{out}}{N_{in}} = \frac{\tau_{out}}{\tau_{in}} \tag{2.14}$$

where *in* and *out* denote the generic input and output gears.

For the system drivetrain, the gear ratios involve different set of gears that transmit torques for the positive and negative motions of the rack. The two different paths through which the torque is transmitted, reflecting the expansion and contraction of the bellows, are shown below in Figure 2.5.

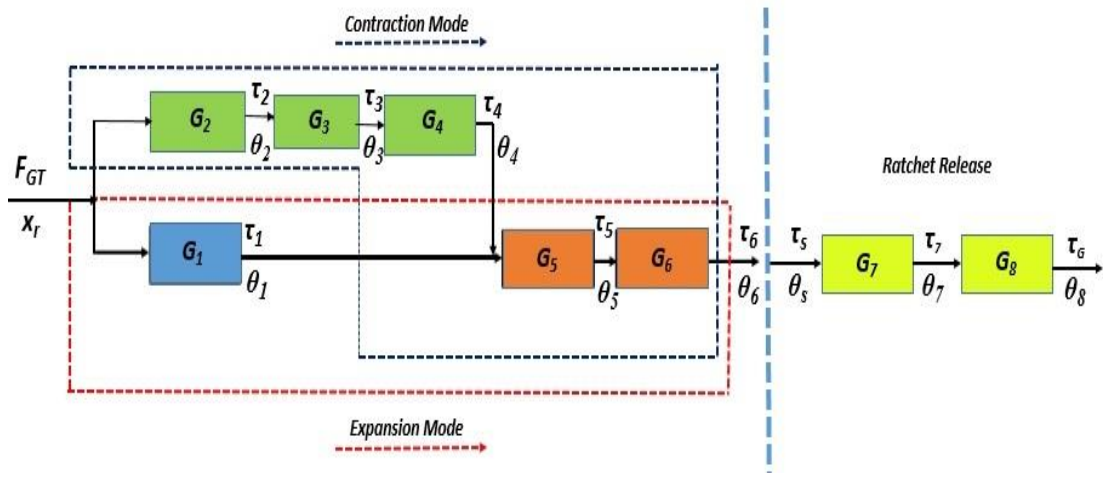

Figure 2.5: Elements of the Drive Train with Bellows Expansion and Contraction Pathways

Bellows Expansion Mode $\left(\frac{dx_r}{dt} \geq 0\right)$

When the rack moves in the positive direction, Gear G_1 transmits torque while Gear G_2 is in free spin due to the placement and functionality of the one way bearings. The rack and pinion relationship driving the gear train can be expressed using (2.12) as

$$\omega_1 = \frac{1}{r_1}\left(\frac{dx_r}{dt}\right), \theta_1 = \left(\frac{x_r}{r_1}\right) \tag{2.15}$$

where r_1 is the radius of Gear 1. The unidirectional bearings on shaft A (refer to Figure 3) ensure that the torque transmission and rotational displacement of Gear 5 occurs in one direction, regardless of the direction of the rack motion. Gear G_5 meshes with gear G_6 on shaft C, which winds the torsional mainspring. Gear G_4 remains disengaged during this motion due to the internal bearing (the unidirectional bearings allow motion transmission or free spin only when actuation is directly provided).

Gears 1, 4 and 5 are on the same shaft. Since the inertia and damping of all rotational elements are assumed to be negligible, the angular velocities and transmitted torques are similar, respectively, for a given axle or

$$\omega_1 = \omega_5 \; ; \tau_1 = \; \tau_5 \tag{2.16}$$

The input torque to the spring, τ_6, and the amount the spring is wound, θ_6, at Gear 6 may be defined using the relationship between Gears 5 and 6 as

$$R_{56} = \frac{r_6}{r_5} = \frac{N_6}{N_5} = \frac{\tau_6}{\tau_5} = \frac{\omega_5}{\omega_6} \tag{2.17}$$

Using (2.16) and (2.17), the drivetrain relation between the rack input at gear G_1 and the angular displacement of gear G_6, which determines the spring input becomes

$$R_{56} = \frac{\tau_6}{\tau_5} = \frac{\tau_6}{\tau_1} = \frac{\omega_5}{\omega_6} = \frac{\omega_1}{\omega_6} \tag{2.18}$$

Similarly, the rotational displacement of gear G_6, θ_6, can be written using (2.15) as

$$\theta_6 = \frac{1}{R_{56}}\theta_1; \; \theta_6 = \frac{1}{r_1 R_{56}} x_r \tag{2.19}$$

The input torque to the mainspring, τ_6, can be expressed using (2.18) as

$$\tau_6 = \; R_{56}\tau_1 \tag{2.20}$$

Therefore, the force acting on the rack due to the gear train in the positive direction of the bellows motion becomes

$$F_{GT} = \frac{1}{r_1 R_{56}}\tau_6; \; \frac{dx_r}{dt} \; \geq 0 \tag{2.21}$$

Bellows Contraction Mode $\left(\frac{dx_r}{dt} < 0\right)$

In the negative direction of rack motion, gear G_1 free spins on the shaft via the one way bearings. Gear G_2 transmits power along shaft B and gear G_3 meshes with gear G_4 on shaft A. Torque is transmitted through Gears 2-6 to effectively continue winding the mainspring. The rotational displacement of gear G_2 can be expressed using (2.12) as

$$\omega_2 = \frac{1}{r_2}\left(\frac{dx_r}{dt}\right), \theta_2 = \left(\frac{x_r}{r_2}\right) \tag{2.22}$$

The gears G_2 and G_3 are on the same shaft and therefore their torques and angular velocities may be given by

$$\omega_2 = \omega_3 \; ; \tau_2 = \tau_3 \tag{2.23}$$

From (2.14), the torque, τ_4, of gear G_4 in the negative direction of rack motion can be written in terms of the gear ratio, R_{34}, as

$$R_{34} = \frac{r_4}{r_3} = \frac{N_4}{N_3} = \frac{\tau_4}{\tau_3} = \frac{\omega_3}{\omega_4} \tag{2.24}$$

Using the relationships in (2.16), (2.18) and (2.23), the gear ratio, R_{34}, can be rewritten as

$$R_{56} = \frac{\omega_3}{\omega_4} = \frac{\omega_2}{\omega_5} = \frac{1}{R_{56}}\frac{\omega_2}{\omega_6} \tag{2.25}$$

Therefore, the rotational displacement of gear G_6, θ_6, for a negative rack cycle can be expressed as

$$\theta_6 = \frac{1}{R_{34}R_{56}} x_r \tag{2.26}$$

The unidirectional bearings on the shafts ensure that the torque is transmitted only in one direction, which implies that the rotational displacement at gear G_6 is always in the direction of winding the spring as long as the ratchet is fixed. Using (2.19), (2.26) can be rewritten in terms of rack displacement as

$$\theta_6 = \frac{1}{r_2 R_{34} R_{56}} |x_r| \tag{2.27}$$

The torque acting on the rack due to the gear train in the direction of negative rack motion is given by

$$\tau_2 = \frac{1}{R_{34} R_{56}} \tau_6 \tag{2.28}$$

For contraction of the bellows, the drivetrain force acting on the rack due to the gear train becomes

$$F_{GT} = \frac{-1}{r_1 R_{34} R_{56}} \tau_6 ; \frac{dx_r}{dt} < 0 \tag{2.29}$$

General Case for Bellows Motion

The generalized equations governing the dynamics for the spring rotational input, θ_6, and gear train force acting on the rack, F_{GT}, can be summarized as

$$\theta_6 = \begin{cases} \frac{1}{r_1 R_{56}} x_r & , \frac{dx_r}{dt} \geq 0 \\ \frac{1}{r_2 R_{34} R_{56}} |x_r| & , \frac{dx_r}{dt} < 0 \end{cases} \tag{2.30}$$

$$F_{GT} = \begin{cases} \frac{1}{r_1 R_{56}} \tau_6 & , \frac{dx_r}{dt} \geq 0 \\ \frac{-1}{r_2 R_{34} R_{56}} \tau_6 & , \frac{dx_r}{dt} < 0 \end{cases} \tag{2.31}$$

D. Spring Torque and Potential Energy

The translational displacement of the rack engages the drivetrain elements which produces a torque at the mainspring coil. The coil winding stores this torque as potential energy which is dependent on the displacement of this coil from an initial position. The spring torque can be generally expressed in terms of the spring rate, k_s, and the rotational displacement at its input on shaft C or the rack displacement as

$$\tau_6 = k_s \vartheta_6 = \frac{k_s}{r_1 R^* R_{56}} |x_r| \; ; \; R^* = \begin{cases} 1 & , \frac{dx_r}{dt} \geq 0 \\ R_{34} & , \frac{dx_r}{dt} < 0 \end{cases} \tag{2.32}$$

This torque can be used to calculate the force acting on the rack through the gear train as

$$F_{GT} = sgn\left(\frac{dx_r}{dt}\right) \frac{k_s}{(R^* r_1 R_{56})^2} x_r \tag{2.33}$$

In most cases, the gear ratio, R_{34}, can be taken as unity so that the R^* term becomes one.

Lastly, the potential energy stored in the spring, E_s, can now be expressed as

$$E_s = \frac{1}{2} k_s \theta_6^2 \tag{2.34}$$

Pre-compression effects for the mainspring are not considered in this model. It is also assumed that the mainspring is wound completely and then released for all power generation cycles.

E. Coiled Spring Release to Drive DC Generator

The spring dynamics at release are governed by the rotational displacement and torques related to the meshing of the gears, G_7 and G_8, as shown in Figure 2.3. If the spring

is wound and released at each power generation cycle, then the state of the ratchet mechanism may be defined by

$$ratchet = \begin{cases} engage; (\theta_6 - \theta_7) < \theta_{max}, \forall\, \omega_8 > 0 \\ release; (\theta_6 - \theta_7) \geq \theta_{max}, \omega_8 = 0 \end{cases} \tag{2.35}$$

where ω_8 is the angular velocity of the generator shaft, and θ_{max} is the maximum mainspring displacement.

The mainspring drive torque released to the generator shaft, τ_7, is dependent on the spring constant, k_s, and the difference between the rotational displacement of the barrel, θ_7, and mainspring input shaft displacement, θ_6, so that

$$\tau_7 = \begin{cases} 0 & ; (\theta_6 - \theta_7) < \theta_{max}\,, \forall\, \omega_8 > 0 \\ (\theta_6 - \theta_7)k_s & ; (\theta_6 - \theta_7) \geq \theta_{max}\,, \omega_8 = 0 \end{cases} \tag{2.36}$$

The barrel gear, G_7, meshes with gear G_8 and the corresponding gear ratio, R_{78}, is given by

$$R_{78} = \frac{r_8}{r_7} = \frac{N_8}{N_7} = \frac{\tau_8}{\tau_7} = \frac{\omega_7}{\omega_8} \tag{2.37}$$

Thus, the available torque, τ_8, to drive the generator becomes

$$\tau_8 = R_{78}\tau_7 \tag{2.38}$$

F. DC Generator Dynamics

The DC generator input is supplied by the stored mainspring potential energy as shown in Figure 2.6. The generator's mechanical dynamics is described using the equivalent inertia, J_e, the equivalent viscous damping of the generator, c_e, the torque, τ_8, and the generator load torque, τ_G, such that

$$J_e \frac{d^2\theta_8}{dt^2} + c_e \frac{d\theta_8}{dt} + \tau_G = \tau_8 \tag{2.39}$$

The generator torque, τ_G, may be expressed as a function of the armature current, i_a, and motor torque constant, k_t, as

$$\tau_G = k_t i_a \tag{2.40}$$

The electrical behavior of the DC generator is affected by the inductance, L_a, total resistance, R_G, and generator voltage constant, k_b. The resulting equation is given by

$$L_a \frac{di_a}{dt} + R_a i_a + V_L = k_b \frac{d\theta_8}{dt} \tag{2.41}$$

where V_L is the voltage produced across the load. The generator's the load resistance, R_L, could ideally be made equal to the internal resistance or armature resistance of the generator, R_a, to obtain maximum power, or

$$R_L = R_a \tag{2.42}$$

The voltage measured across the load, V_L, is given in terms of the current, i_a, and the load resistance, R_L, as

$$V_L = R_L i_a \tag{2.43}$$

Finally, the power output from the generator depends on the current, i_a, and the voltage, V_L, so that

$$P = V_L i_a \tag{2.44}$$

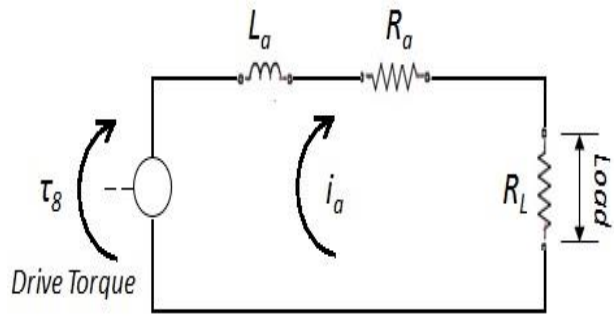

Figure 2.6: DC Generator Electric Circuit

It is evident that the main factors influencing the electric power output are the circuit resistance and the inductance, R_a and L_a, the gear ratio, R_{78}, the coiled spring stiffness, k_s, and the maximum spring displacement, θ_{max}.

Numerical Results

The energy harvester mathematical model was implemented in MATLAB/Simulink to investigate the system dynamic behavior. To drive the system, a sinusoidal temperature profile was applied to the bellows' ethyl chloride vapor. The resulting pressure changes were converted into a force that actuates the bellows expansion and contraction. The bellows end plate provides a bidirectional displacement to the rack. This displacement is converted into unidirectional rotational motion and supplied to the shaft that winds the coiled mainspring. The ratchet, or pawl, was designed to operate as defined in (2.35). When the pawl is disengaged, the potential energy in the coil spring is

transferred to the DC generator as kinetic energy, to produce electric power. The simulation model parameters are summarized in Table 2.1.

The dynamic behavior of the mechanical driven generation system was investigated through computer simulations. The input temperature profile features a ±1°C amplitude variation every 3.5 hours about a constant temperature of 22°C as viewed in Figure 2.7(a). The system was operated for 24 hours before the release mechanism was triggered to generate electricity. In actual operation, atmospheric temperature and pressure variations based on the geographic location will dictate the winding period. It is important to note that the ethyl chloride vapor pressure and bellows output force follow the temperature curve.

A minimum and maximum force of 297 N and 277 N are transferred to the bellows end plate for the given temperature variations and bellows' end plate area. The end plate displacement transferred to the rack produces a maximum rack displacement of 3.25 cm as shown in Figure 2.7(b). There is a very minute gear train force acting on the rack which is attributed to the resistive back torque from the spring winding. The angular rotation of the coil spring, θ_6, increases and holds for each cycle as shown in Figure 2.8(a). The discrete steps correspond to the peaks in the temperature cycle until the release mechanism is engaged. For this study, the spring is wound more for one rack direction than the other, since R_{34} is greater than 1. Also, the given spring is considered to be fully wound at 2 turns for this study. At release, the power generation occurs at a higher frequency (e.g., within a span of 5 seconds). The torque input to the generator, shown in Figure 2.8(b), is typical mainspring behavior. A maximum of 2 Nmm drive torque is increased 5 folds by the internal gear ratio, R_j, between the generator shaft and the armature. The maximum current

and voltage produced in the generator are 44 mA and 0.22 V per Figure 2.9(a), with a 5Ω resistance load. For this design, the maximum power generated was 9.6mW as shown in Figure 2.9(b). The storage element design, load resistance, and the release intervals largely dictate the amount of power that can be generated.

The numerical model in the present study indicates that sufficient electric power can be generated through the DC micro generator to operate low power sensors and electronics over a 24 hour harvesting period, assuming temperature variation between 21°C < T_{amb} < 23°C. Further investigations performed using optimal model parameters predict similar power generation over a 24 hour period for regions experiencing high diurnal temperature variations. The proposed ambient thermal energy harvester generates greater power than typical TEGs, and also eliminates the need for secondary power amplification units and external voltage supplies which are typical to currently employed thermoelectric devices [50].

SYMBOL	VALUE	UNITS	SYMBOL	VALUE	UNITS
A	44.67	-	N_1, N_2	48	-
A_p	2e-3	m^2	N_3, N_4	30.90	-
B	-4026	-	N_5	20	-
c	18	Ns/m	N_6	33	-
C	-3.37	-	N_7	72	-
c_r	2	Ns/m	N_8	144	-
c_e	3e-5	Ns/ rad	P_{atm}	1.10e5	Pa
D	2.27e-17	-	r_1, r_2	26.50	mm
D_b	2.50e-2	M	r_3, r_4	32.40	mm
E	6	-	r_5	11	mm
J_e	8.00e-5	kgm^2/rad	r_6	16.50	mm
k_b	6.00e-3	V/rpm	r_7	38	mm
k_{bs}	120	N/m	r_8	42.80	mm
k_{es}	500	N/m	R	8.31	J/Kmol
k_r	1500	N/m	R_{34}	3	-
k_s	9.75e-5	Nm/rad	R_{56}	1.65	-
k_t	6.00e-3	Nm/A	R_{78}	2	-
L_a	3.00e-5	H	R_a	1	Ω
m	2.00e-1	kg	R_j	5	-
m_r	2.00e-2	kg	R_L	5	Ω
n	2.80e-1	mol	θ_{max}	13	rad

Table 2.1: System Design Parameter Values and Units

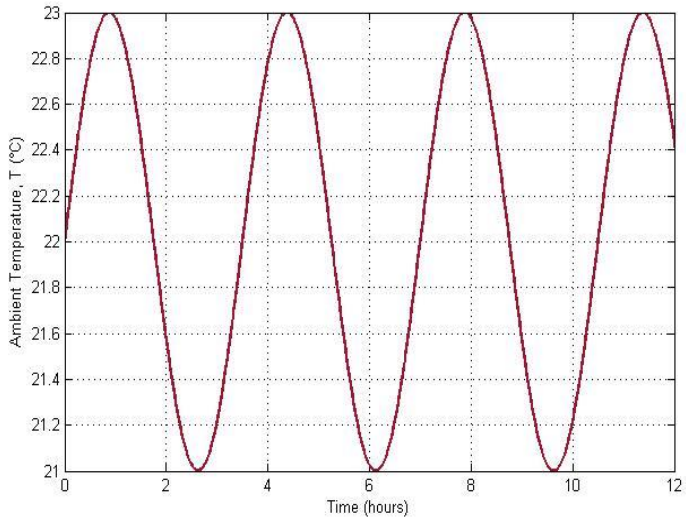

(a)

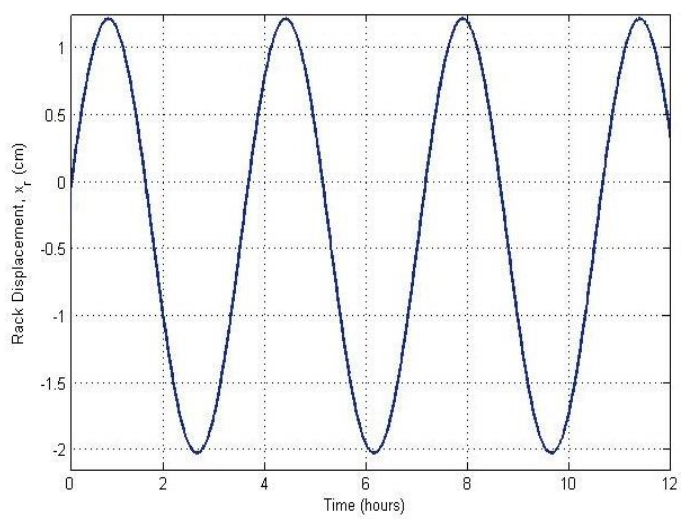

(b)

Figure 2.7: Dynamic Response of Energy Harvester – (a) Ambient Temperature and (b) Rack Displacement

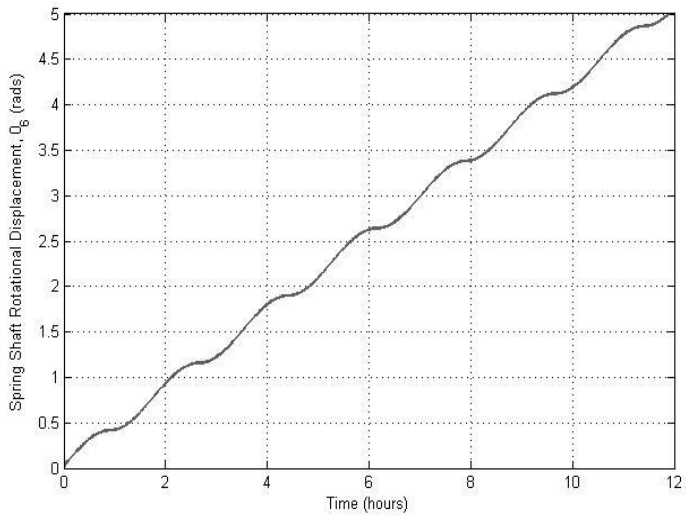

(a)

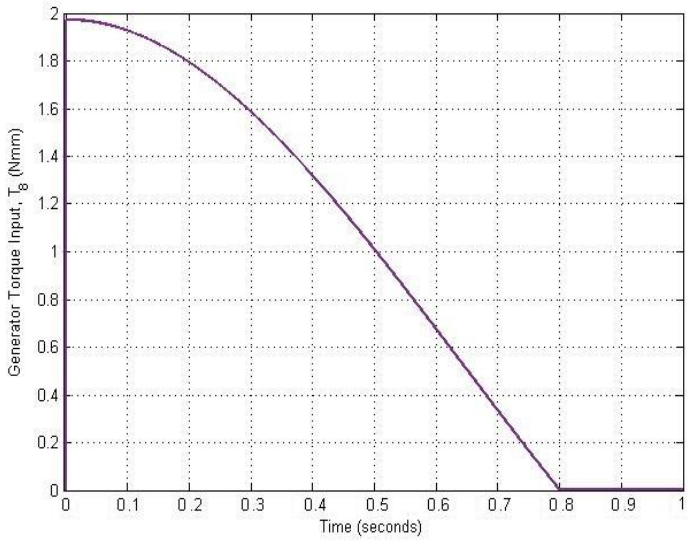

(b)

Figure 2.8: Dynamic Response of Energy Harvester – (a) Spring Shaft Rotational Displacement and (b) Generator Torque Input for 'Hold' Duration of 24 Hours

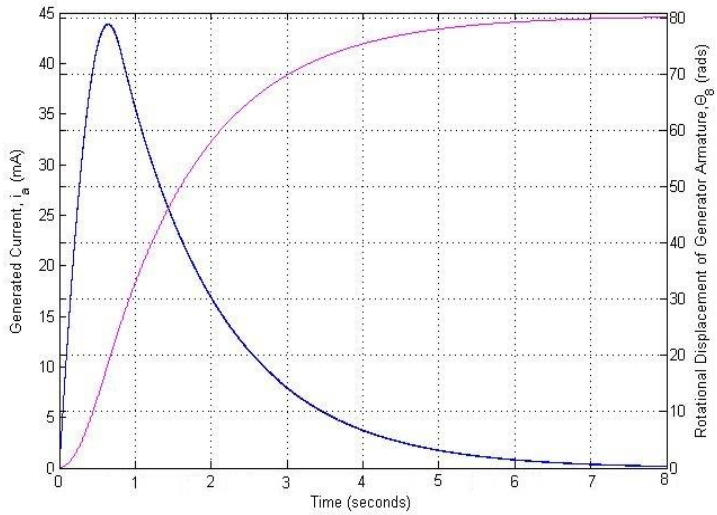

(a)

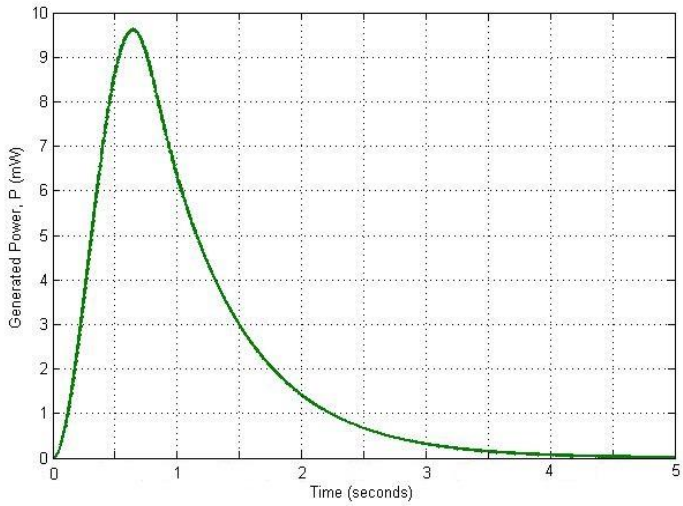

(b)

Figure 2.9: Dynamic Response of Energy Harvester – (a) Generated Current and Corresponding Generator Shaft Rotation, and (b) Generated Power

Summary

The proposed energy harvester is a self-contained device that operates on atmospheric temperature and pressure variations to produce “clean” electric power. Although the amount of power is relatively small, it is sufficient to run miniature electronic circuits. The integration of the mechanical drivetrain, storage spring, and DC generator with the thermodynamic driven bellows has been mathematically modelled and numerically simulated to explore the functionality of the system. Such a green energy device can be deployed in remote regions where considerable diurnal temperature variations exist, in industrial processes that generate low frequency, low temperature cyclical waste heat, and waste heat from engine operation [51]. The vapor in the bellows can be chosen to suit the available temperature profile, and the entire system (e.g., bellows, drivetrain, spring, and generator) can be scaled to operate within the desired application in a sustainable manner.

CHAPTER THREE

DEVELOPMENT OF THE EXPERIMENTAL SYSTEM AND TEST BENCH DESCRIPTION

The experimental harvester system was developed in three stages such that the individual components—the bellows system and the drivetrain-spring-generator assembly—can be tested separately. In previous research, a prototype bellows system was tested and its development has been discussed [37]. This study focuses more on the mathematical modeling of the multiple harvester domains for analyzing the behavior of the device through simulations, as well as experimentally testing a prototype drivetrain-spring-generator assembly to verify efficient utilization of the bellows bidirectional motion in generating electric power. This section specifically discusses the development of the prototype drivetrain-spring-generator assembly with the accompanying ratchet mechanism. It is important to note the experimental systems of the harvester device have been scaled as required to be able to observe the system behavior and for easier testing in the laboratory environment. The experimental designs are not optimal models.

Introduction

The drivetrain-spring-generator assembly design is crucial to the device development since it is responsible for the manipulation and storage of the harvested ambient thermal energy, and for electric power production. The design process begins with

identifying a storage unit to collect sufficient amount of the low frequency harvested thermal energy and produce electric power across the DC machine. The intermediate mechanical system is also required to capture the bidirectional behavior of the bellows linear motion and effectively scale the large force provided by the vapor to be stored as potential energy at the storage element. A mechanism is needed to govern or control the collection and release of stored energy from the storage unit. The DC micro generator needed to be snugly mounted to hold the frame stationary through the entire duration of burst electric power production and handle the high torque input. It is important that this assembly be robust and stable through multiple harvesting and power generation cycles, since it serves the primary purpose of the entire device. The key idea in this research was to create a mechanical intermediate system between the harvesting and power generation unit to improve the thermal-electric power conversion efficiency of the ambient thermal harvester. The solutions developed in addressing the design requirements, detailed discussion of the mechanical intermediate system design, and the issues handled during production are discussed below.

Experimental System Development

The first step in the development of the power transformer was to identify a robust storage element that can collect the available potential energy and provide considerable power generation at release. This element needed to be incorporated with the DC machine and provide rotational motion at higher frequencies to actuate the generator armature and

produce useable electric power. Borrowing inspiration from older spring-driven clock movements, a mainspring contained inside a barrel was used as the energy storage unit. A mainspring is a metallic torsional spring that can store potential energy when wound into a spiral. The mainspring used in this study was housed inside a cylindrical drum or barrel with a geared rim called the going barrel, and one end of the spring was attached with the inner wall of the barrel while the other end hooked onto a central axle to the drum called the arbor. The mainspring had very small dimensions in thickness and width, lower stiffness rates but larger lengths to allow multiple 360° winding motions. The spring was wound by turning the arbor while holding the going barrel stationary and releasing it would convert the potential energy contained in the spring to kinetic energy of the barrel gear. It is important to note here that the spring should be wound to maximum allowed by design, and not full capacity since this could cause the spring to break or be displaced from the drum due to very high tension.

The potential energy contained in winding can then be transferred to the DC generator shaft by employing a spur gear (gear G_8) to mesh with the going barrel gear. Typically employed in watches, the entire assembly is very compact and also an efficient power source over several cycles. The experimental steel mainspring with a brass going barrel was borrowed from a vintage timepiece and is shown in Figure 3.1. The steel arbor contained a small gear which has not been utilized in this experiment—the coupling between the drivetrain shaft and the arbor was designed to directly lock the arbor and the small gear frame with the shaft containing the end gear in the drivetrain. The coupling is shown in Figure 3.2.

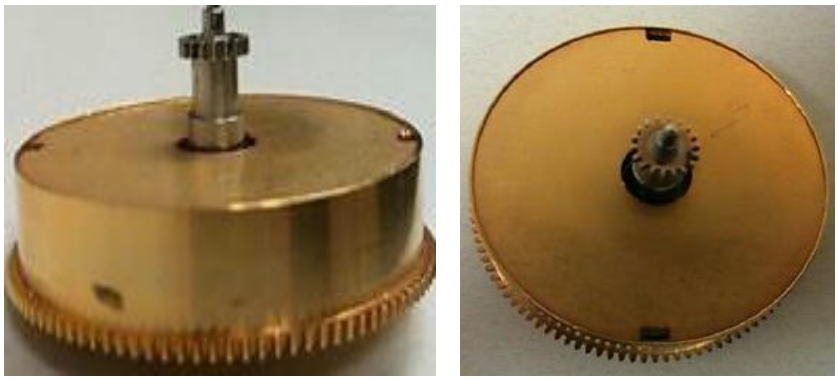

Figure 3.1: Experimental Spring

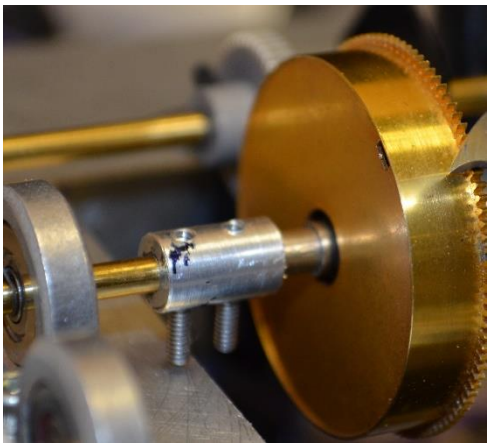

Figure 3.2: Spring Shaft Coupling

The next step in developing the assembly was to identify a system to convert the linear motion of the bellows end plate into rotational motion for a proposed energy storage component (the mainspring). A simple rack and pinion mechanism has been employed for this purpose (Figure 3.3). Another mechanism was required to utilize the bidirectional

bellows end plate motion through the rack and pinion. A compound gear train transmission with a single stainless steel rack and two pinion gears mounted on parallel brass shafts housing secondary acetal spur gears, and strategically placed one-way bearings were implemented. The one-way bearings used in the system (Figure 3.4) are such that motion is transmitted to the shafts only for external actuation of the gear inside which they are placed. Depending on which way the bearing face was inserted on the shaft, it transmitted motion for one direction and allowed the gear to disengage from the shaft (free spin) in the opposite direction.

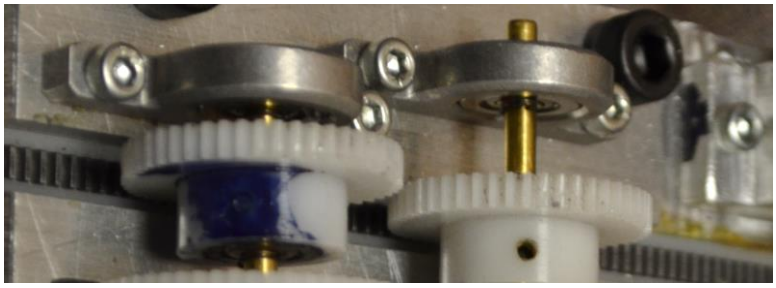

Figure 3.3: Rack and Pinion

Figure 3.4: One-Way Bearing Fitted Inside Gear Hub

For the experimental system, holes were drilled into the gear to accommodate the bearings. Grooves were cut into the shafts and snap rings were fixed into it to eliminate unwanted lateral motion of the gears (Figure 3.5). A third shaft with a corresponding spur gear coupled to the mainspring key and wound it. Detailed functionality of the gears and bearings, and the transmission pathways have been discussed exclusively in the harvester design (Chapter 2). The shaft assemblies containing the gears, bearings, and retaining rings (Figure 3.6) were fitted into mounted pillow blocks with bearings (Figure 3.7) that allowed for the shaft rotation and held in place.

Figure 3.5: Grooved Shaft Assembly with One-Way Bearing inside Gear with Set Screw

Figure 3.6: Retaining Ring

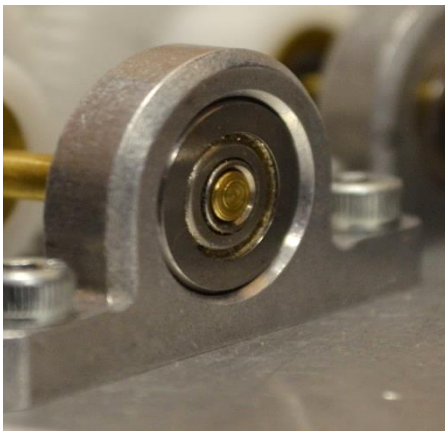

Figure 3.7: Mounted Pillow Blocks with Bearings

The entire drivetrain was mounted onto a 0.25” thick aluminium plate with cuts and holes made to accommodate all components and fixtures (Figure 3.8). A cut was made into the plate and fitted with a machined plastic insert that snugly accommodated the rack to slide back and forth while meshing with the pinion gears (Figure 3.9). This plastic insert was glued onto the aluminium plate surface using strong adhesives and its main purpose was to eliminate unwanted lateral rack motion. Gears and couplings were locked with the shafts using 2-56 set screws as required, and 5-40 cap screws locked the pillow blocks onto the plate (Figure 3.10).

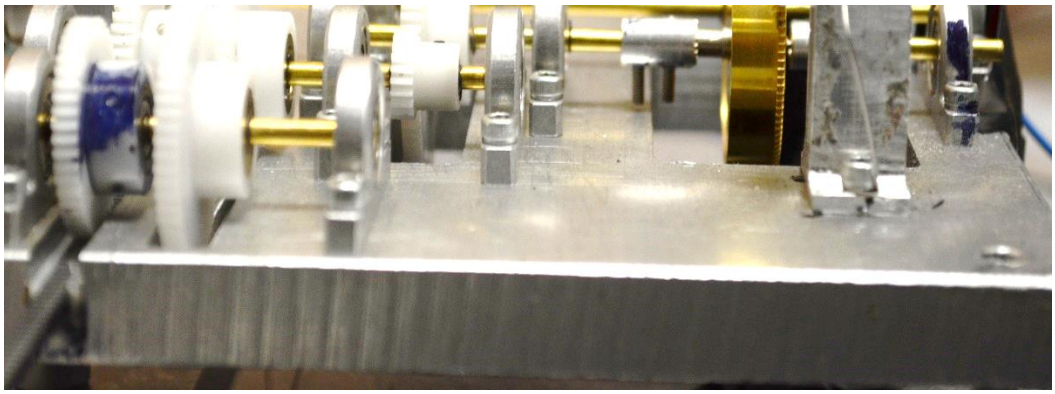

Figure 3.8: Experimental Plate

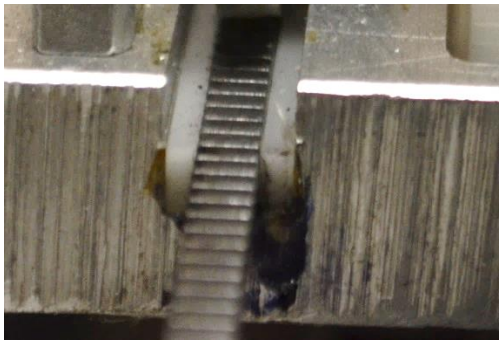

Figure 3.9: Plastic Insert and Rack

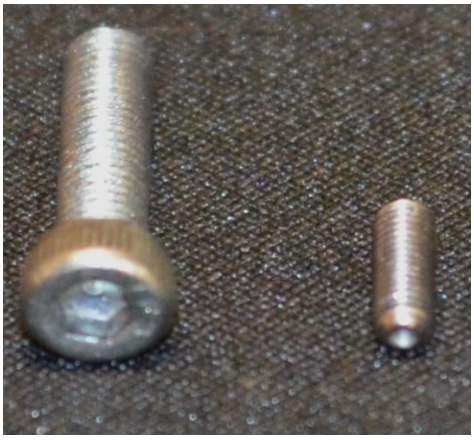

Figure 3.10: Cap Screw and Set Screw

Design of a control mechanism for the mainspring winding and release was also borrowed from the ingenuity of ancient watch making. A custom designed vertically locking, ratchet mechanism with a meshing face to match the barrel gear teeth was developed as shown in Figure 3.11. The ratchet was held in place by a spring wire under tension to lock the barrel gear and this simple mechanism (Figure 3.12) was found to easily tolerate the experimental mainspring tension during winding. With the spring characteristics known, the spring hold and release have been manually controlled for the experimental tests.

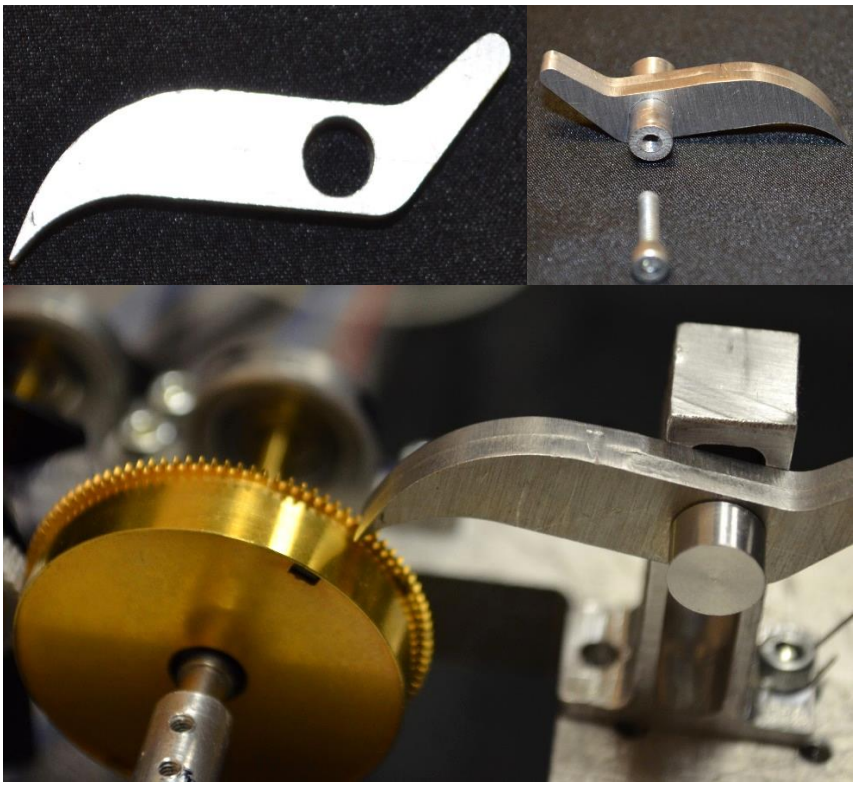

Figure 3.11: Ratchet

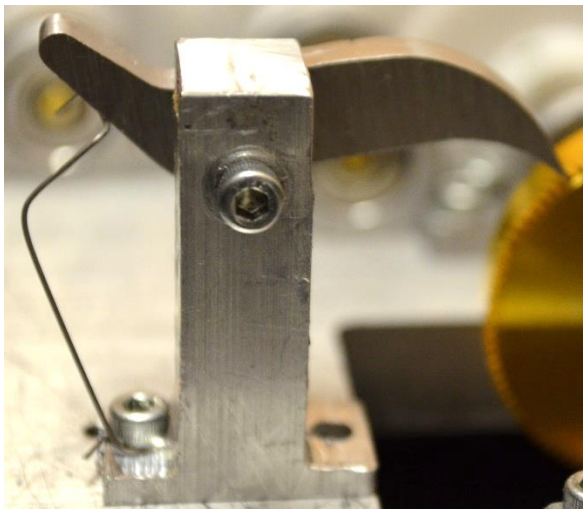

Figure 3.12: Spring Wire to Hold Ratchet

The experimental DC generator is a Swiss made linear micro generator rated at 1.5 V as shown in Figure 3.13. Wires extended from the back of the generator and could be connected to an external load. From load tests, it was observed that there was an internal gear ratio of 4.7:1 associated with the DC generator between the shaft and the armature. The shaft of the generator had a secondary gear and was offset from the housing's center. An aluminium coupling similar to that of the mainspring arbor was made to interface the gear shaft with the brass shaft (driven by gear G_8) delivering power as shown in Figure 3.14. An aluminium mount was custom designed and fabricated for holding the DC generator as shown in Figure 3.15.

Figure 3.13: DC Generator Set (borrowed from eBay)

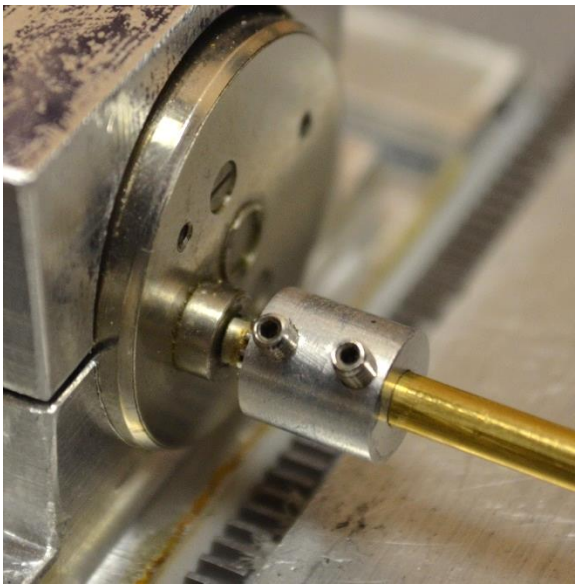

Figure 3.14: Gear Shaft Coupling

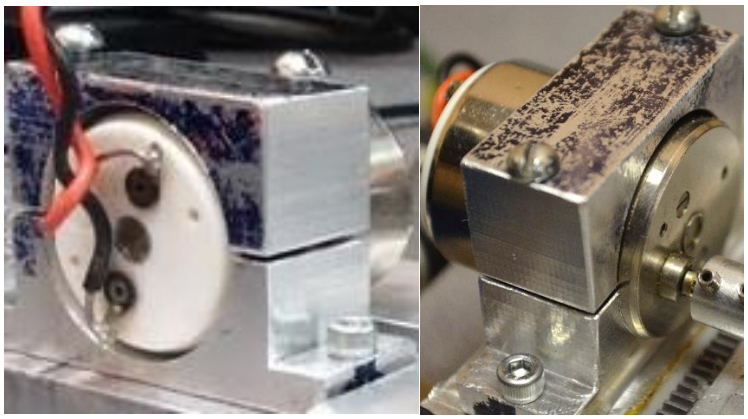

Figure 3.15: Generator Mount/Housing

The target was to identify a compact lightweight drivetrain-spring-generator design that can be easily tested in a laboratory environment. To achieve the lightweight design criteria, all the experimental drivetrain components were precision micro-manufactured units made of stainless steel, aluminium, brass, and plastics. All component functionalities were simultaneously tested throughout the development process and the final design was developed over a few iterations. The developed prototype assembly can be tested easily across an allowable range (i.e., without unseating the rack from the plastic insert or disengaging from the pinion gears using a simulated bidirectional linear motion of the bellows).

Test Bench Description

For testing and validating the electromechanical subsystem of the harvester, the bellows end plate motion that linearly actuates the rack had to be experimentally actuated.

The most important variables that needed to be captured are the rack displacement, the speed of the generator shaft, and the generated voltage output from the DC generator. Other variables could be easily calculated by measuring these values and extensive sensing circuitry could thus be avoided.

The bellows end plate displacement was emulated using a linear actuation unit that consisted of a DC motor, cam, spring, and linear piston running on a standard power supply as shown in Figure 3.16. The rotational motion of the DC motor was converted into linear actuation through the cam and the spring restricted overshooting of the piston. An interface was now required to merge the rack to the piston to utilize the latter's motion. An aluminium interface was designed to lock the rack edge on one end and fasten to the piston on the other end as shown in Figure 3.17. The entire electromechanical assembly had to be raised to effectively connect with the actuation unit and four cylindrical pillars made out of hollow aluminium rods were used near the four edges of the base plate. The pillars were screwed into place through the base plate and actuator base using hex screws as shown in Figure 3.18. The two systems, actuator and prototype, were successfully merged together for testing (Figure 3.19).

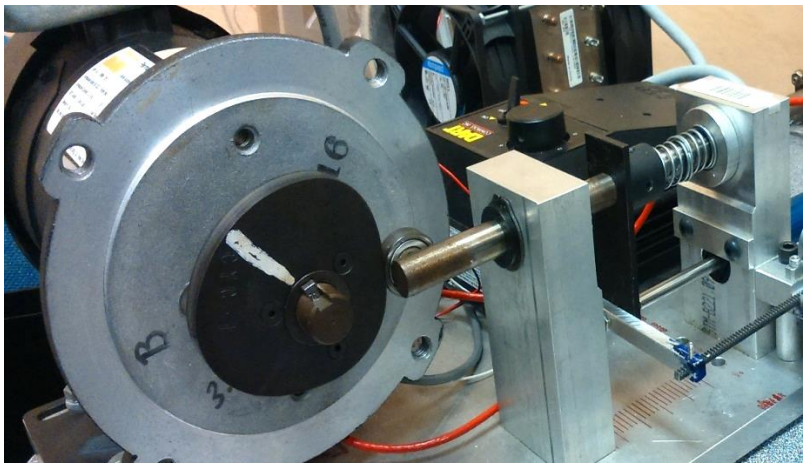

Figure 3.16: Linear Actuation Unit

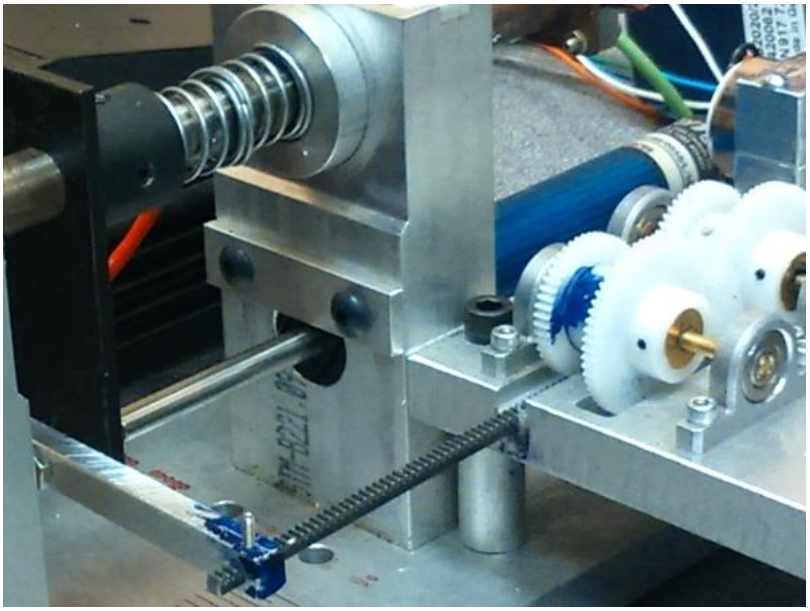

Figure 3.17: Rack-Piston Interface

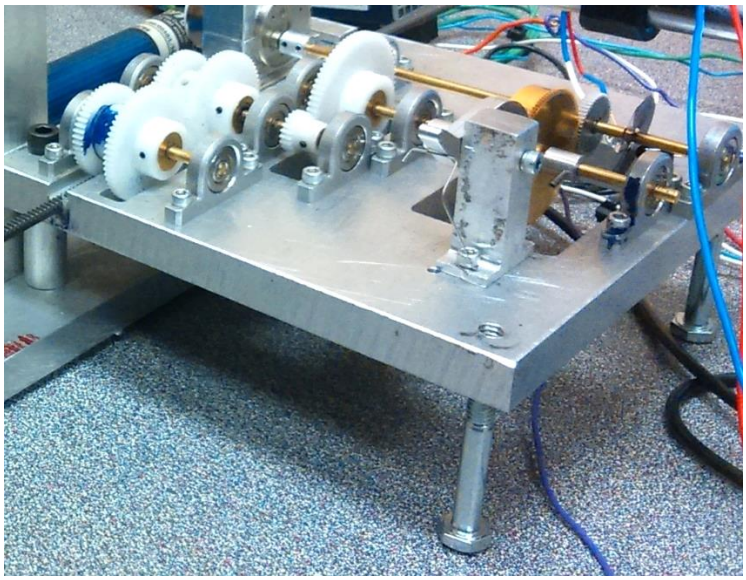

Figure 3.18: Pillars to Raise Electromechanical Assembly

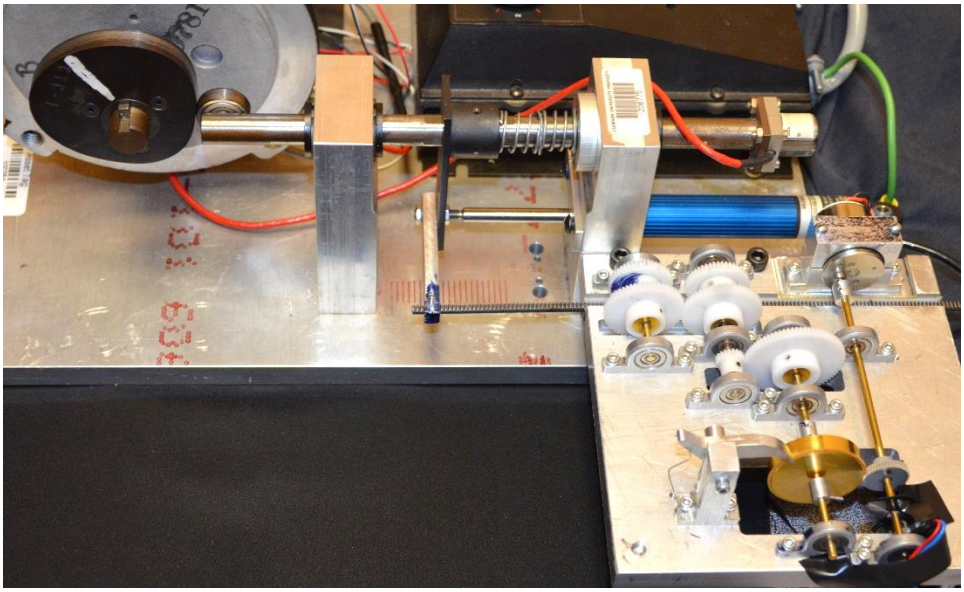

Figure 3.19: Test System

The next step in the test development was to identify sensors to measure the required variables. A linear potentiometer was used to measure the rack displacement (Figure 3.20). A linear encoder circuit was built using IR LEDs and an operational amplifier (Figure 3.21). The voltage from the generator can be directly measured through an analog channel on a data acquisition device or using a voltmeter. National Instruments NI SCB 68 data acquisition board (Figure 3.22) and LabVIEW programming interface were used to collect measurements as well as to power the sensors.

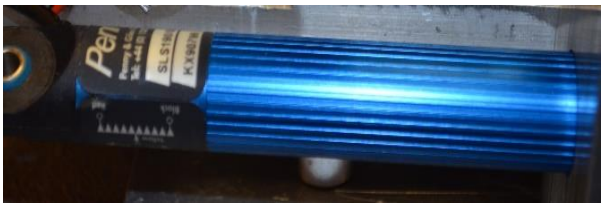

Figure 3.20: Linear Potentiometer

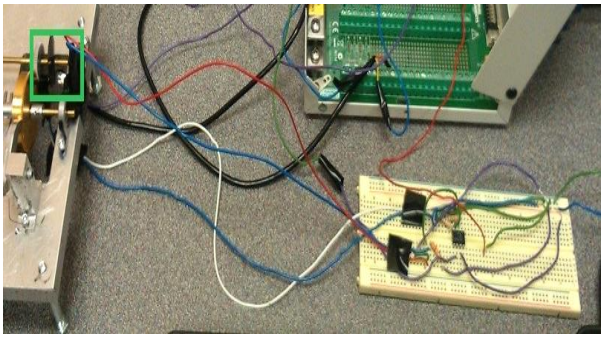

Figure 3.21: Encoder Circuit

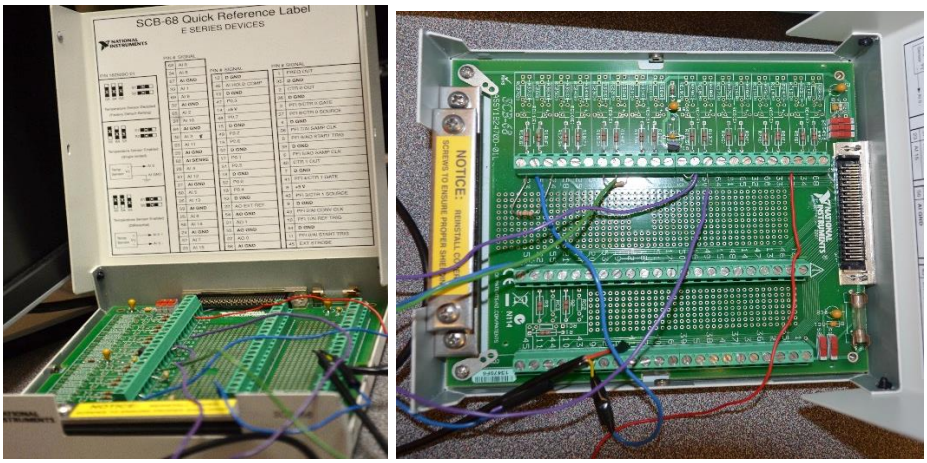

Figure 3.22: Data Acquisition and Control Board – NI SCB 68

Voltage outputs from the LVDT and encoder circuit had to be converted into displacement and speed values, and other parameters needed to be calculated for validation of the numerical models. Therefore, post processing of the experimental results was done, and National Instruments LabVIEW and Mathworks MATLAB softwares have been used. The resulting values and graphs were then compared with the numerical analyses. The experimental process is discussed further and the results are presented in the following chapter.

CHAPTER FOUR

LINEAR MODEL AND TEST OF AN ATMOSPHERIC ENERGY HARVESTER SYSTEM

Energy harvesters are steadily gaining popularity as a power source for microelectronic circuits, particularly in wireless sensor nodes and autonomous devices. Energy harvesting from small temperature and/or pressure variations, coupled with an appropriate energy storage unit, can generate sufficient electric power to operate low power electronics. Ongoing research in this area seeks to improve the power capacity and conversion efficiencies of such systems. In this project, a phase change vapor based atmospheric energy harvester with an electromechanical power transformer has been developed. An ethyl chloride fluid system converts the pressure generated, in response to nominal environmental changes, into usable electric power through a mechanical driveline-spring unit and attached DC generator. Published numerical results have indicated 9.6 mW power generation capacity over a 24 hour period for a low frequency sinusoidal temperature input with ±1°C variation at standard pressure (refer to Chapter 2). A prototype electromechanical unit was fabricated and experimentally tested; 30 mW electric power for a resistance load was recorded for an emulated input corresponding to 50 bidirectional cyclic atmospheric variations. Linearized models were derived to help evaluate the system's transient characteristics and these results agreed favorably with the experimental system behavior.

Introduction

Energy harvester systems capture ambient energy in the form of sunlight, vibration, heat, and biological sources, to name a few, to generate electric power [16]. Renewable energy technologies have received consideration in global markets that tend to be motivated by rising environmental consciousness and implementation of dedicated green energy policies by governing entities [2]. Scavenging energy from ambient sources remains an attractive research field with application to wireless sensor nodes, internet of things, and connected autonomous devices [52]. Investigators are striving to improve the operational efficiency of harvesters, and onboard energy storage continues to be an important aspect in the designs [53]. One of the most abundant renewable energy source is atmospheric energy (e.g., pressure and temperature variations). Efficiently harvesting and converting environmental variations into electricity has tremendous potential, especially in standalone operation of devices located in isolated or inaccessible regions. Thermal energy harvesting applications range from the aerospace industry to low power consumer electronics [54].

Most thermoelectric devices, typically operating on the Seebeck effect, require large temperature gradients ($\Delta T \geq 50°C$) and electronic circuitry to generate practical amounts of power (≥ 0.1mW) [11]. The development of thermoelectric generators featuring significant thermal gradients (($\Delta T \geq 25°C$)) have been widely reported [20,55,56]. Yildiz and Coogler [57] discussed thermocouple arrays that can generate electric power in the range of microwatts for ambient temperatures between 15 – 27°C. An interesting study by Leonov [32] regarding the integration of thermophiles into textiles observed that body heat

can be harnessed to generate milliwatt power over several months if worn for 10 hours per day. Phase change materials may also be used for thermal energy harvesting as well to improve thermal storage units [58-60]. The main drawback of harnessing atmospheric energy tends to be the low conversion efficiencies of current harvesters for small thermal gradients [61]. Given the potential of thermal harvesters, a need exists to improve the thermal-electrical conversion efficiency to advance the power generation capacities of such devices for microcircuit operation [6].

The combinations of ambient pressure changes with low temperature gradients may improve the performance of thermal harvesters, especially in chemical based systems. One of the most brilliant employment of volatile vapors in harnessing and utilizing atmospheric variations may be observed in the Atmos clock operation. Studies by Martt [46] show that the mechanical motion of the clock is entirely powered by atmospheric energy, with temperature changes as low as 1°C, through the use of vapor-filled mechanical bellows. Inspired by the Atmos clock's efficient and self-sustained operation, the dynamic behavior of the clock mechanisms have been reported [38,43]. Our article explores the power generation capabilities of an atmospheric harvester by adapting the concepts of vapor phase change and driveline mechanisms with a generator set for energy harvesting applications. A system is proposed to utilize the pressure response of ethyl chloride vapor to surrounding pressure and temperature changes, and drive a compact electromechanical device that collects, stores, and converts the harnessed atmospheric energy (refer to Figure 4.1).

In the proposed renewable energy system, pressurized ethyl chloride fills the mechanical bellows to harness atmospheric variations as mechanical motion. A compound

drivetrain amplifies and stores this displacement in a coil spring that may be controllably released to operate a DC generator and generate electric power. Using experimental data collected by S. Patel *et al.* [36], the pressurized ethyl chloride operating conditions for energy harvesting were assumed to lie between -1 to 30°C. A series of nonlinear mathematical models have been previously developed to describe the different domains involved in the harvester device–thermal, mechanical, and electrical. Initial numerical analyses predicted 9.6 mW power generation over a 24 hour harvesting period for temperature variations between 21°C and 23°C [62]. The electrical output should be sufficient for burst power operation of micro networks or capacitor energy storage [63].

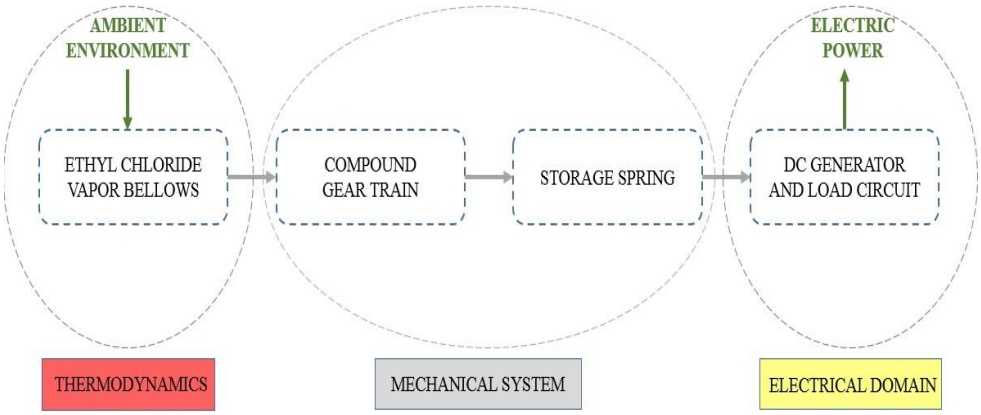

Figure 4.1: Energy Harvester Device Overview

The research goal is to establish a fundamental understanding of the atmospheric energy harvester system by studying the transient behavior as well as validating its performance through experimental testing. The use of individual transfer function

relationships between sequential domains allow a pragmatic understanding of the device. A micro-scale portable device (refer to Figure 4.2) targeting power availability for low power electronics especially in locations with limited access to large scale power grids, has been designed and fabricated. Experimental tests were performed on the prototype system to validate its operation. The remainder of the section is organized as follows. First, the transfer function models are derived for the energy harvester. Then, the experimental hardware is discussed followed by the numerical and experimental results. The conclusion summarizes the work done in this research and Appendix A provides a summary of the governing system equations.

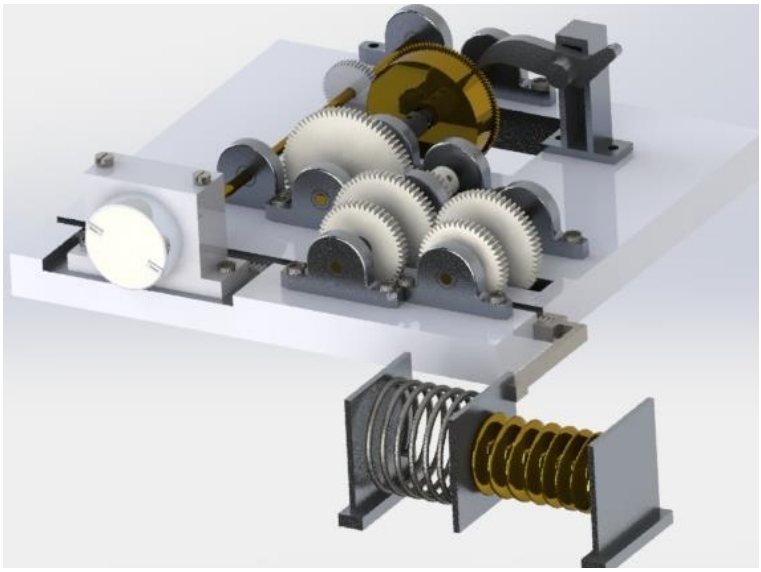

Figure 4.2: Microscale Atmospheric Energy Harvester Device Based on Linear Displacement Input

Atmospheric Energy Harvester System

The atmospheric energy harvester consists of an ethyl chloride fluid filled mechanical bellows compressed by an external spring. Pressure variations occurring due to the ethyl chloride phase change in response to temperature/pressure variations are harnessed as mechanical motion at an attached end plate (refer to Figure 4.2). This plate drives a compound gear train that winds a coil spring contained within a geared drum/barrel. The stored potential energy in the spring is then converted into kinetic energy through the barrel and mechanically transferred to a DC generator shaft to generate electric power. The transfer functions describing the three domains (i.e., thermal, mechanical, and electrical) were identified from the dynamic equations [62] with the imposition of four assumptions:

A1: Ethyl chloride vapor pressure may be approximated using the ambient temperature, T, in a first order polynomial curve fitting of Riedel's equation within the bellows' operating range.

A2: Bellows end plate displacement, x, and the rack displacement, x_r, are essentially equivalent.

A3: Rotational displacement of the coil spring is always positive (unidirectional) in the drivetrain dynamics due to functionality of the unidirectional bearings.

A4: Barrel gear displacement, θ_7, at ratchet release is identical to the wound spring shaft behavior, θ_6.

A. Ethyl-Chloride Filled Mechanical Bellows

The ethyl chloride filled mechanical bellows is an assembly containing a hermetically sealed coiled tube attached to a moveable end plate and constrained with a stiff steel spring (refer to Figure 4.2). The ethyl chloride chemical compound used in this system has a low boiling point of 12.3°C and typically exists as a gas at standard room temperature and pressure [64]. Under the pressurized charge, the ethyl chloride liquid-vapor equilibrium is broken for nominal ambient temperature/pressure variations (ΔT = ~0.25°C) and considerable vapor pressure is generated in the bellows tube from the phase change. The expansion and contraction of the bellows tube results in the end plate translational motion.

To describe the thermodynamic behavior of the ethyl chloride inside the bellows tube, its vapor pressure was modeled using Riedel's equation [49]. First order approximations of the Riedel pressure-temperature relationship were used in the model linearization. For the bellows end plate behavior, the mechanical dynamics were obtained using the applied vapor pressure as the input. The amount of ethyl chloride in the bellows, the initial charge, and the bellows volume were not used explicitly in this model. Instead lumped parameter approximations were considered. Using the vapor thermodynamics and the end plate mechanical dynamics, the relationship between the ambient temperature, T, and the bellows end plate displacement, x, may be described by the transfer function

$$\frac{x(s)}{T(s)} = \left(\frac{1}{ms^2 + cs + (k_{es}+k_{bs})}\right)\left(a_1 A_p\right) \tag{4.1}$$

where a_1 is a mathematical constant from first order polynomial curve fit of Riedel's vapor pressure model. The variables A_p, c, k_{bs}, k_{es}, and m are the bellows system design parameters.

B. Mechanical Drivetrain and Coiled Spring

A compound drivetrain consisting of a rack and pinion accompanied by multiple stages of spur gears transform the mechanical motion from the bellows end plate displacement (refer to Figure 4.2). The low amplitude and frequency of the atmospheric variations resulting in the drivetrain displacement cannot be directly coupled to a DC generator and thus, the drivetrain motion is stored as potential energy in the windings of a 'mainspring' until a sufficient amount is available as required by the given application. The torsional coil spring is contained within a geared drum, or barrel, which is wound through a key (i.e., mechanically coupled to the drivetrain). One-way bearings are utilized in the drivetrain to produce unidirectional rotational motion at the coil spring regardless of the bellows end plate motion direction. A ratchet mechanism constrains the geared barrel during spring winding to collect the input mechanical energy and disengages it (which releases the spring) after a defined interval, thus providing kinetic energy to the generator shaft.

The gear train and spring mechanical dynamics dictate the behavior of this mechanical power transformer which interfaces the harvester and the power producing DC generator circuit. The transfer of motion from the bellows end plate to the spring may be

described by the ratio between the coil spring displacement, θ_6, and the bellows end plate displacement, x, so that

$$\frac{\theta_6(s)}{x(s)} = \left(\frac{m_r s^2 + c_r s + k_r}{J_1 s^2 + b_1 s + \left(\frac{k_s}{r_1 R^* R_{56}}\right)}\right); R^* = \begin{cases} 1 & , \dot{x} \geq 0 \\ R_{34} & , \dot{x} < 0 \end{cases} \tag{4.2}$$

where $\dot{x}$ is the velocity of the rack/bellows end plate and represents the direction of the temperature change. The constants c_r, k_r, m_r, R^* and R_{56} are the drivetrain design variables, while b_1, J_1 and k_s are the spring design parameters.

C. DC Generator

A DC generator converts the mechanical energy from the coil spring into electrical energy. The coil in the generator is excited by the generator shaft rotation, produced by the geared barrel at ratchet release, which generates a current in the output load circuit. The generated electric power is dependent on the output spring displacement, the generator dynamics and the applied load. The transfer function may be modeled as the ratio between the generated current, i_a, and the rotational displacement of the coil spring in the barrel, θ_6, so that

$$\frac{i_a(s)}{\theta_6(s)} = \left(\frac{k_b R_{sa}}{R_{78}}\right)\left(\frac{1}{L_a s + \tilde{R}}\right) \tag{4.3}$$

where R_{78} is the gear ratio between the barrel gear and the generator shaft gear. The other model constants are the power generation electrical system design parameters, k_b, L_a, R_{sa}, and $\tilde{R}$. The electrical circuit can also be represented in the generator dynamics if properly

defined. The power generated across the electrical load will be directly proportional to the current and the voltage in the load circuit.

D. Overall System Model

The overall system consists of the atmospheric harvester attached to the electromechanical assembly as shown in Figure 4.2. The flow of energy between the different domains in the system is illustrated in Figure 4.3. The energy flow process is initiated by atmospheric variations which are converted into mechanical effort by the vapor in the bellows tube. This force results in linear displacement of the bellows end plate and thus, motion of the rack gear. The drivetrain converts this linear movement into torque to wind the coil spring while the ratchet holds the barrel stationary. At release, the barrel gear is disengaged, releasing the coil spring, to provide rotational motion to the generator shaft and generate electric power.

The transfer function between each individual domains and the corresponding energy flow have been used in describing the overall system behavior. To obtain a comprehensive relationship, several assumptions (A.1 – A.4) have been imposed to account for the disconnections between the harvesting system and the storage system as well as the power generation unit and the mechanical power transformer. The fundamental quantities describing the overall system operation are the atmospheric temperature, T, and the current (or power) generated in the output load circuit, i_a. The relationship between the ambient temperature as an input and the electric current generated may be determined using equations (4.1) through (4.3), so that

$$\frac{i_a(s)}{T(s)} = \left(\frac{i_a(s)}{\theta_6(s)}\right)\left(\frac{\theta_6(s)}{x(s)}\right)\left(\frac{x(s)}{T(s)}\right) = \left(\frac{a_1 A_p k_b R_{sa}\beta}{R_{78}}\right) *$$

$$\left(\frac{m_r s^2 + c_r s + k_r}{(L_a s + \tilde{R})\left(ms^2 + cs + (k_{es} + k_{bs})\right)\left(J_1 s^2 + b_1 s + \frac{k_s}{r_1 R^* R_{56}}\right)}\right) \tag{4.4}$$

where gain, β, compensates for the system uncertainties and nonlinearities between the energy harvester and power generator. The amount of stored energy, the generated power, and the duration of the ratchet "hold and release" cycle can be manipulated by varying the various design parameters described in (4.4). Identification of optimal design parameters and automation of the ratchet operation would render an efficient, autonomous atmospheric harvester device running on clean energy.

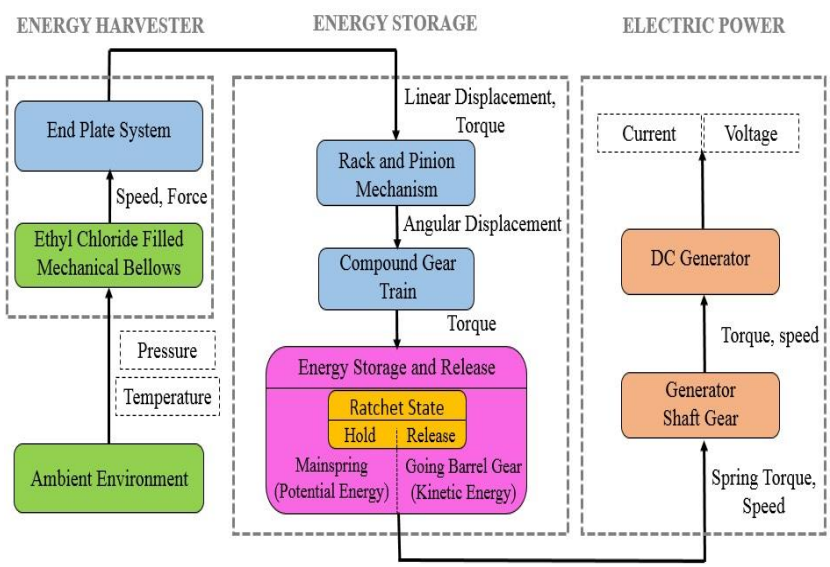

Figure 4.3: Energy Flow Diagram for the Atmospheric Energy Harvester

Benchtop Experimental System

An experimental prototype system has been fabricated to validate the mathematical model and evaluate the proposed design capabilities. Benchtop testing was performed in a controlled laboratory environment to facilitate repeatability. As the drivetrain-spring-generator assembly may function independently from the mechanical bellows end plate, these elements were assembled into a single electromechanical subassembly as shown in Figure 4.4. The two experimental configurations consist of the thermodynamically driven ethyl chloride filled mechanical bellows and the driveline with generator set; the latter will be the study's primary focus. For the experimental tests, data acquisition was performed using National Instruments hardware/software with attached sensors and actuators.

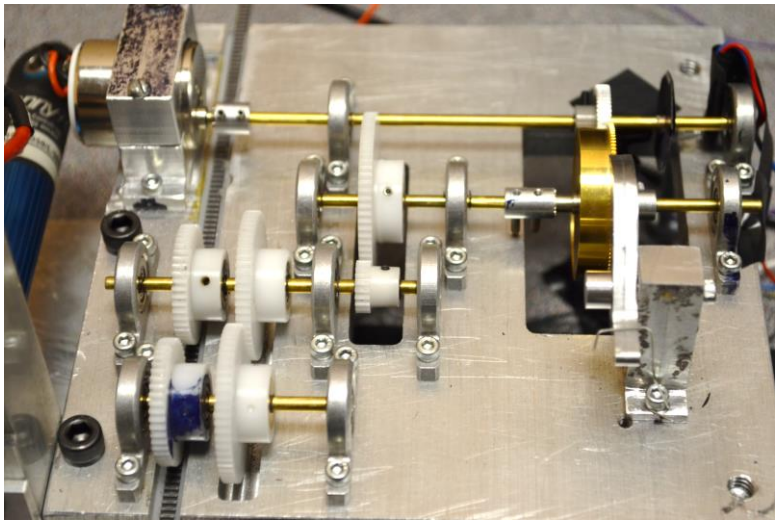

Figure 4.4: Experimental Prototype of the Drivetrain and Spring Assembly, and DC Generator Set Assembled onto a 15cmx15cmx0.6cm Aluminium Plate

A. Ethyl Chloride Filled Mechanical Bellows

The mechanical bellows comprises the ethyl chloride fluid contained within a flexible tube structure which allows it to respond to atmospheric variations. The saturated vapor at room temperature can be considered the energy harvester's prime driver. For the experiment, the bellows was fabricated using a helical coiled bronze tube, an aluminium end plate, and a steel restraining spring. Pressurized ethyl chloride was injected into the tube at room temperature to realize a liquid-vapor equilibrium so that nominal changes in the ambient temperature/pressure will result in end plate displacement. The bellows was placed inside an acrylic chamber to isolate it from the surrounding environment (refer to Figure 4.5). Thermoelectric actuators were introduced to simulate ambient temperature changes. To monitor the system behavior, temperature, pressure, and position sensors were integrated into the plant. The thermodynamic behavior of the bellows was tested for ±2°C temperature variations about 23°C. The bellows' end plate moved up to 4 cm resulting in an available potential energy of 6 J [37].

In this study, the tests focused on validating the electromechanical assembly and identifying the device's power generation capacity. The bellows system was replaced with an electric motor assembly featuring an attached cam resulting in translational displacement to emulate the end plate behavior in moving the rack (i.e., driveline input). Further testing may be performed in similar operating environments with the electromechanical assembly coupled to the bellows assembly to recreate the real time operation of the final harvester device.

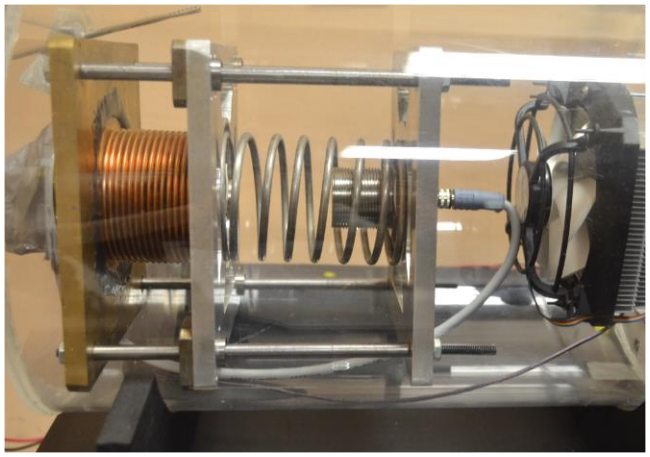

Figure 4.5: Ethyl Chloride Filled Mechanical Bellows Assembly (20cmx25cmx20cm) which Generates End Plate Displacement

B. Drivetrain, Spring Assembly and DC Generator Set

The drivetrain-spring-generator was designed to be a scalable subsystem that stores the harvested energy and converts it into useable electric power. As previously described, a rack and pinion mechanism transforms the end plate's translational displacement into angular displacement. The strategic placement of one-way bearings allowed unidirectional winding of the spring due to both bellows' expansion and contraction. A lightweight design was achieved using micro-manufactured acetal gears, precision brass shafts, stainless steel bearings with plastic locks, and a stainless steel rack. The shaft ends were held in place using mounted pillow blocks with bearings. Grooves were cut into the shaft and snap rings were fitted onto them to prevent unwanted axial movement of the gears/shafts.

The torsional coil spring consisted of spring steel, housed inside a barrel. One spring end attaches to the driveline output shaft, θ_6, and the other was fixed to the inner surface of the barrel. The mechanical coupling between the key and the winding shaft used

a pillow block with inserted bearing for load support. A ratchet mechanism was custom made to mesh with the external teeth of the barrel to lock its motion in the winding cycle and retract easily for release. A 1.5 V DC micro-generator with an associated internal gear ratio was mechanically coupled to the output shaft containing a spur gear that interfaced with the barrel gear. A mount was custom made for the DC generator to hold the housing stationary. All the components were attached to an aluminium plate. The system parameters are listed in Table 4.1.

The DC motor driven cam created bidirectional motion that emulated the bellows end plate displacement supplied to the rack. A linear potentiometer monitored the rack motion while a rotational encoder identified the motor speed. The release ratchet was manually controlled using a thin steel spring. Attached current and voltage sensors measured the electrical performance so that the generated power may be calculated. Multiple cycles of the rack input were considered so that the spring was sufficiently wound before being released to generate electric power.

C. Integrated Harvester Device

The power generating harvester mechanism will be a fusion of the thermodynamic bellows and the mechanical driveline sub-assembly. The overall system requires linking the bellows end plate and the rack gear. For final testing, the bellows system including the hermetically sealed acrylic chamber may be attached to the rack gear without compromising the integrity of the chamber. The ratchet mechanism may be automatically controlled to lock/release when the coil spring is fully wound.

Symbol	Value	Units	Symbol	Value	Units
a_1	5088.00	Pa/K	L	1079.50	mm
A_p	5.00e-03	m^2	L_a	5.50e-05	H
b	5.97	mm	m	2.20e-01	kg
b_1	1.00e-03	Ns/rad	m_r	2.00e-02	kg
c	18.00	Ns/m	r_1	26.50	mm
c_r	2.00	Ns/m	R_{34}	1.00	-
E	2.07e05	MPa	R_{56}	3.75	-
J_1	1.00e-05	kgm/rad	R_{78}	4.70e-01	-
k_b	5.20e-03	Vs/rad	R_{sa}	4.70	-
k_{bs}	2.50e02	Nm/rad	R_L	100.00	Ω
k_{es}	9.00e02	N/m	$\tilde{R}$	101.00	Ω
k_r	195.00	Nm/rad	t	9.00e-02	mm
k_s	6.95e-05	Nm/rad	θ_{max}	31.41	rad
k_t	2.50e-02	Vm/rad			

Table 4.1: Design Parameter Values in the Numerical and Experimental study

Numerical and Experimental Results

The transfer function models previously developed to describe the atmospheric harvester system with the attached electromechanical power generator were used to characterize the transient behavior via computer simulations. A transfer function approach requires linear system descriptions. Thus, the thermal, mechanical, and electrical dynamics have been linearized through approximations and reduced operating spaces. To validate

these simplified governing equations, numerical and experimental results will be compared. The prototype electromechanical assembly was tested for a prescribed rack motion and the experimental generated electrical power was evaluated. A series of MATLAB models were created and the simplified mathematical models validated using test results from the laboratory bench.

The simulation response for the individual domains, as well as the overall harvester system, are presented in Figures 4.6 and 4.7. As shown in Figure 4.6(a), for a unit step change in the ambient temperature, T, the bellows end plate displacement, x, has a short peak before settling within 0.1 seconds. The rotational displacement of the spring, θ_6, for a unit change in the rack displacement showed similar behavior per Figure 4.6(b) due to the system stiffness. The system time constant, τ, was 25 ms. In the power generation cycle, after the coil was wound 5 complete turns to θ_{max} (corresponding to 10π rad rotations of the shaft/spring, θ_6), initially a step change in the rotational spring displacement input to the generator shaft produced a damped current, i_a, which settled to 16 mA within 3 µs. An impulse response was considered to better emulate the burst input to the generator—the current responded to an impulse temperature input by slowly rising to 16.1 mA and dissipating within 0.15 s as displayed in Figure 4.7(a). Finally, the overall system response to an impulse temperature input, after 50 temperature cycles to θ_{max}, indicates that the power, P, slowly rises to a maximum of 35 mW and dissipates to zero, with some backlash as expected from the sudden spring release (refer to Figure 4.7(b)). In practice, the power is dissipated across the given electrical load in similar bursts although a capacitor can help

manage this scenario and backlash is minimal from sufficient mechanical damping. Consequently, the power decays to zero once the stored spring energy decreases to zero.

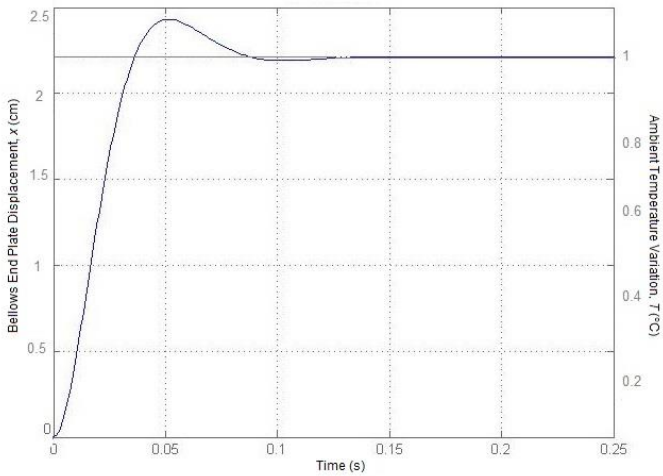

(a)

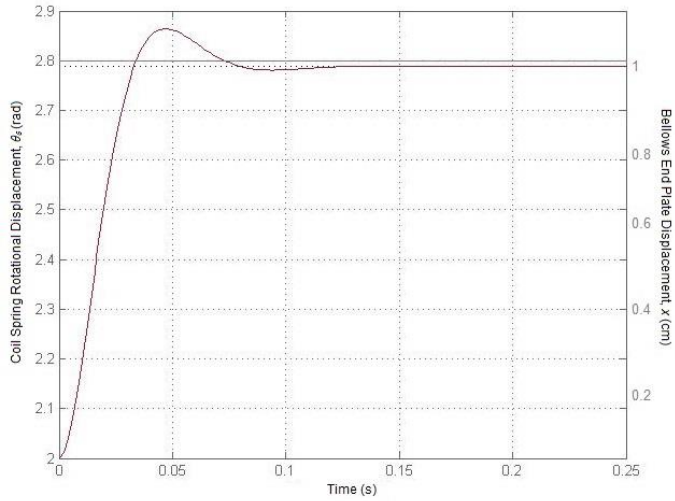

(b)

Figure 4.6: Numerical results – (a) Bellows End Plate Response, x, to a Step Temperature, T, and (b) Spring Rotational Displacement, θ_6, for a Step Rack Linear Displacement, x, after θ_{max}.

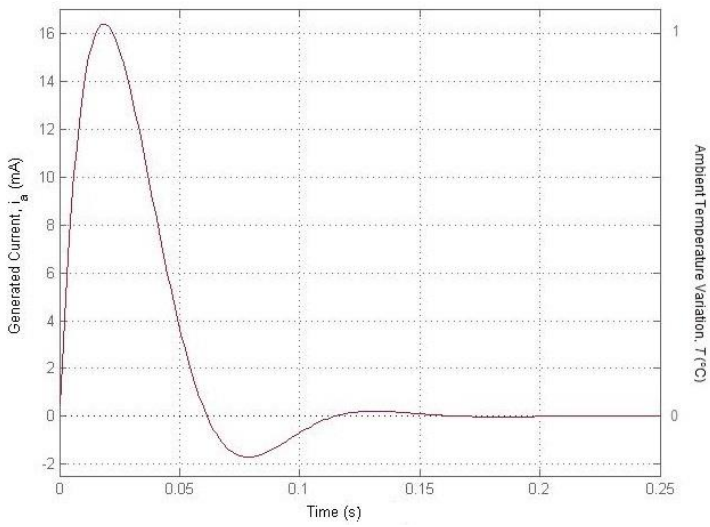

(a)

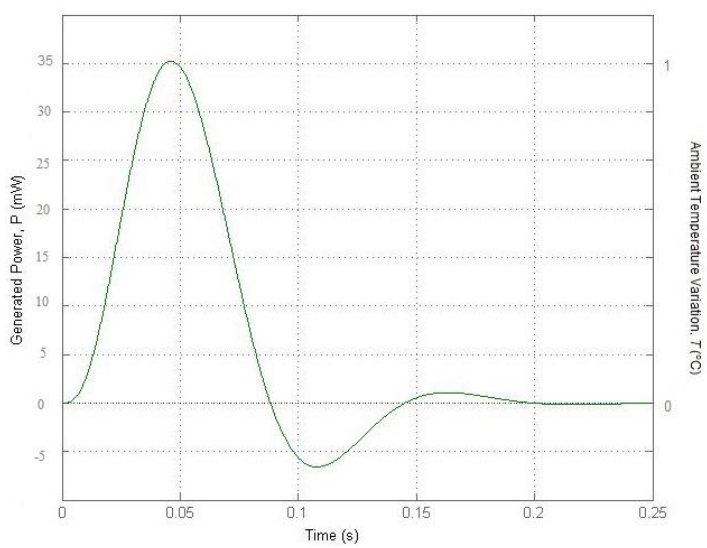

(b)

Figure 4.7: Numerical results – (a) Generated Current, i_a, versus Impulse Temperature Input, T, after θ_{max}, and (b) Power Generation Response, P, to an Impulse Temperature Input, T, after θ_{max}.

To complement the numerical results, representative laboratory testing was performed. The experimental results obtained from testing the electromechanical assembly

for the supplied rack displacement cycle are presented in Figure 4.8. The thermal cycling of the bellows gas produced the original displacement; however, this has been emulated with a DC motor cam system for convenience. For 50 rack displacement cycles (refer to Figure 4.8(a)) with a maximum displacement of ±2 cm, the potential energy stored in the mainspring was 135 mJ. The rack displacements correspond to over 175 hours or 7 days of actual operation based on a ±1.5°C variation per hour. The ratchet was manually released. The generator shaft speed, as measured by an encoder, peaked at 250 rad/s before quickly decaying with a total of 12 complete rotations. The maximum generated voltage, V_L, and current, i_a, across a resistance, R_L, of 100 Ω was 1.88 V and 16 mA, respectively. Therefore, the maximum power, P, generated at the DC unit from releasing the fully wound coil spring was determined to be 30 mW per Figure 4.8(b) (roughly filtered and polynomial fitted). As expected, the generator shaft speed, the output voltage, the output current, and the generated power were all observed to follow similar profiles.

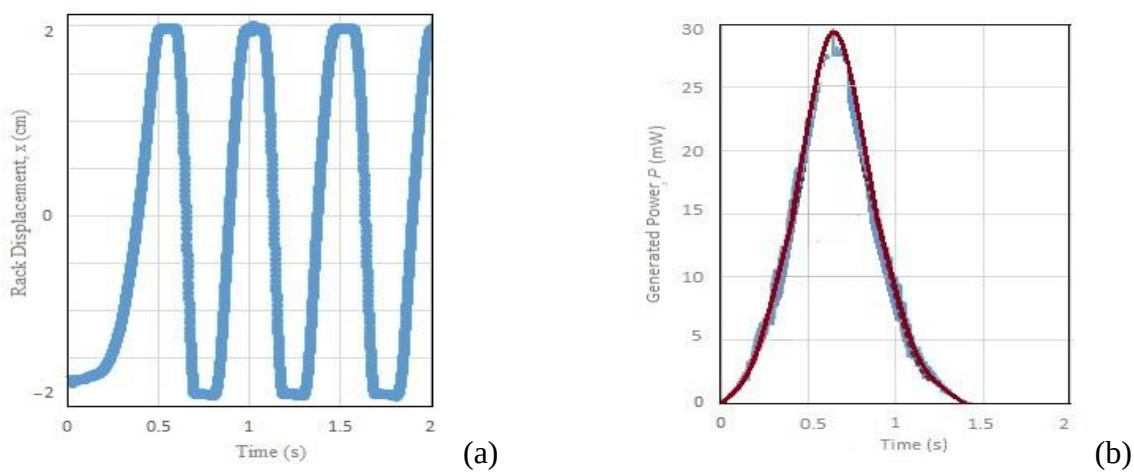

Figure 4.8: Experimental Results – (a) Rack Input Profile, x; and (b) Generated Electric Power, P.

An analysis of the numerical and experimental results indicate that milliwatt electric power can be regularly generated from atmospheric temperature/pressure variations using the proposed energy harvester. The computer simulations initially produced a current of 30 mA rather than the laboratory result of 16 mA; a gain, β, was introduced to compensate for the model uncertainties. The 5 mW (16.78%) difference between the experimental and simulated power may be attributed to the model simplification and database parameters.

The performance of energy harvesters in transforming small ambient changes into electric power may be further enhanced by optimizing the mechanical drive train, energy storage unit, and generator set. For the power generated by the proposed system, a resistor-capacitor network may be introduced to meet continuous power requirements in microelectronics such as low power sensors. There appears to be an abundance of applications using small atmospheric changes that can be captured by the contained vapor, and the potential future for this device in atmospheric energy utilization and waste energy recovery is promising.

Summary

A robust electromechanical system with a phase change material based atmospheric harvester has been developed and tested using both numerical and experimental techniques. Linear transfer functions are proposed and analyzed to establish a fundamental understanding of the system behavior. Experimental tests on a prototype electromechanical device predict milliwatt power generation capabilities. It is evident from the concurring experimental and simulation data that sufficient electrical energy is generated from atmospheric scavenging to be stored in supercapacitors or utilized in burst electric operation for microelectronics. The open challenges of the system are the low frequency of the harvesting process and the eventual wear of mechanical components. The system can be made autonomous by controlling the ratchet release with the rack interface with the bellows end plate, and implemented as a self-sufficient atmospheric energy scavenging, power generation device for standalone applications requiring low average power.

CHAPTER FIVE

CONCLUSION AND RECOMMENDATIONS

Thermal energy harvesting technologies have the potential to charge and/or replace batteries in electronic devices as well as recover waste heat. Although thermal energy harvesters such as thermoelectrics are widely implemented in applications having large thermal gradients, research is still under way to improve the thermal-electrical conversion efficiencies of these systems. Currently, the application spectrum utilizing energy harvesters for small ambient thermal/pressure variations is narrow due to the limitations of thermally responsive materials, insufficient research on pressure responsive devices, and their impractical power generation capacities. Extensive design considerations, increased production costs, and complex power management solutions are other major drawbacks of thermal energy harvester devices. Unlike other energy harvesting sources, thermal energy is not limited by frequency bandwidths or source availability, it is indefinitely accessible. Therefore, improving such energy harvesting technologies can be considered essential for generating growth in the renewable energy industry.

The performance of pressure/temperature responsive materials in energy harvesters offer an alternative to thermal energy systems. An example of such an approach is the Atmos Clock, created by Jaeger-LeCoutlre, where the clock operation is efficiently powered by a vapor-based harvester scavenging low scale environmental variations. Atmospheric energy harvesting, where both pressure and temperature variations are harnessed, can provide electricity for low power electronics in applications ranging from

simple sensor circuits to charging hand held microprocessor devices. This type of a harvester can play a pivotal role in improving the cost and efficiency of remote electronic devices and wireless networks. Research in atmospheric energy harvesting technologies, with a focus on energy storage, can lead to the development of portable systems that efficiently power a wide range of electronics using renewable sources. Pressure and temperature based energy harvester systems may be advantageous in terms of source availability, power generation capacities, scalability, and implementation flexibility.

Avoiding extensive power-consuming circuitry in the operation of thermal/pressure harvester devices is crucial to improving the thermal-electrical conversion efficiency of such systems given the limited harvested energy by current materials. Therefore, an almost exclusively mechanical system has been proposed, developed, and studied to harness/store and convert atmospheric energy to usable electrical power. This system combines phase change material (PCM) responses, gear and driveline transmission mechanisms, and energy storage capacity of springs with a DC generator to achieve an efficient thermal/pressure-electrical conversion system. Initial stages of work previously done for this research elaborated on the design, development and test of the phase change chemical based atmospheric harvester system – an ethyl chloride filled mechanical bellows acted upon by a spring. Controlled testing of a prototype bellows system identified the proportional relationship between ambient temperature variations and the end plate linear displacement. One objective has been to minimize friction losses in the mechanical system.

Mathematical Models and Analyses

Using previous studies on the atmospheric energy harvester and the proposed energy availability for power generation, an electromechanical assembly has been innovated to efficiently convert the bellows end plate linear displacement into usable electric power. Mathematical models were identified for the integrated system (i.e., bellows interfaced connected to the electromechanical assembly by a stiff interface) and transfer functions derived from the dynamical equations to study the behavior and performance of individual sub-systems as well as the overall system. The mathematical models render a fundamental understanding and design for the proposed harvester device. The power production observed is a temporary burst that can be supplied to a storage device such as a supercapacitor. Initial numerical simulations suggested a 9.6 mW power generation capacity across a 5 Ω resistance load, assuming temperature variations between 21°C < T_{amb} < 23°C over a 24 hour period. Further investigations into critical design parameters for the electromechanical system rendered a more optimal model with a power generation capacity of 95 mW for similar temperature cycles.

The transient behavior of the domains in response to the corresponding step inputs using transfer functions were obvious given the modularity of the system. The thermal domain proved comparatively harder to model and linearizing the Riedel vapor pressure equation to simplify the pressure-temperature relationship was necessary. A first order polynomial approximation has been used in linearizing the Riedel's vapor pressure equation to simplify the transfer function relationships. Although, a second order

polynomial approximation of the Riedel model is an appropriate fit and provides more accurate system responses as well as better behavioral insights and control over the design, it is not presented. The mathematical representation of the system can be improved by identifying more accurate thermal models for the phase change material other than the Riedel model and better understand the system capabilities. Pressure studies can be conducted by varying the operational environment to further our understanding of the ethyl chloride vapor in atmospheric energy harvesting. Similarly, investigations into the dynamical models associated with the coil spring behavior, pre-compression effects of the springs, and non-ideal gear interactions may provide better insights into the behavior of the electromechanical system.

While exploring the dynamic relations for this system to obtain the transfer function models, the disconnection between the different domains in the system are evident. The energy harvesting bellows system and the electromechanical assembly, separated by the bellows end plate-rack interface, can function independent of one another. The driveline-spring system is also decoupled from the electrical unit (DC generator) through the ratchet and allowing control over the duration of the energy harvesting process, thus providing a greater range for implementation. In retrospect, the electromechanical system can possibly be implemented as a power transformer for other energy harvesting applications producing a linear displacement output. The DC generator can also be replaced to directly operate a mechanical system at the spring output, generating greater standalone application scope for the atmospheric energy harvester with only the mechanical unit.

Experimental Results and Discussion

The next step in this study was to validate the developed mathematical models and the proposed design for the electromechanical assembly. A prototype system was developed and fabricated for benchtop testing in a laboratory environment. The design for the drivetrain-spring-generator assembly with the ratchet was established over few iterations in trying to efficiently fit all components into a compact 6'' x 6'' plate. The required spring stiffness was approximated from torque results predicted by the numerical simulations, and iterated over two values with the accompanying ratchet face also being modified to mesh with the corresponding barrel gear. The final experimental system used in laboratory testing consistently generated electric power in the milliwatt region. A generated electrical power of 30 mW across a 100 Ω resistance was recorded using a storage element (i.e., coil spring) of 6.95e-03 Nmm/rad stiffness for the emulated rack input corresponding to 50 cyclic atmospheric variations. Representative results from numerical simulations favorably agree with the experimental results and are suggestive of efficient conversion of small atmospheric variations into useable electric power.

The most important advantages of this system include scalability, portability, and higher power generation capacity with the exclusion of extensive power management solutions. The limitations include source irregularity, potentially harmful nature of the vapor as well as its operating limit, and possible increase in production costs with marginal decrease in the system size. Since the ethyl chloride vapor in the bellows is very sensitive to atmospheric variations, such a harvester system can be implemented in any natural

environment to harness ambient energy within the operating range of the vapor. For applications in the upper limit of the milliwatt power spectrum, a more logical implementation would be use the system in regions with high diurnal temperature variations (e.g., southwestern regions of the United States) or in artificial environments with similar thermal/pressure variations.

Recommendations

Future research areas have been identified based on conceptual and intuitive understanding of the system derived from the study. Certain motivating suggestions are listed below for further investigations:

1. Device Automation: An effective mechanism connecting the rack to the end plate with an "engage and disengage" synchronized with the power production cycle (i.e. ratchet) can be identified. The ratchet "hold and release" cycle should also be automated. This can be achieved using mechanical timing elements (e.g., cams, gears) connecting both the rack and the ratchet individually/together, or by using electronically operated actuators (e.g., solenoid operated fluid power systems, springs, etc.).
2. Identification of Optimal System Designs: A smaller, entirely micro-manufactured or 3D printed compact prototype device can be developed and studied. The vapor in the atmospheric energy harvester can be substituted. The mechanical energy transformer unit can be replaced with different transmission

and/or storage mechanisms to better suit application constraints and requirements.

3. Practical Implementation: The performance of an automated system can be tested for different applications (e.g., co-generation, wireless sensors nodes, capacitive charging, etc.) varying the temperature input/operation environment and harvesting period. Specific electrical loads can be investigated as well as on site testing to gather exclusive data.
4. Reduction of System Friction: The critical components (and their operation) comprising the harvester system is mostly mechanical in nature—bellows tube expansion and contraction, end plate linear displacement/sliding on the bellows assembly frame, gear train transmissions, coil spring winding and unwinding, shaft rotations on bearings, and so on. Since the harvesting process is considerably slow, mechanical energy losses are not very large and have not been considered in the designs. It would be interesting to study the product life cycle over several runs and observe the frictional effects, spring slacking, load capacities, and other mechanical behavioral characteristics in the integrated harvester system. To increase the operational life of the harvester system, the mechanical interactions can be augmented by using friction reducing substances (e.g., advanced plastics), as well as by replacing the steel spring coil and the brass bellows tube with better materials having similar properties.
5. Optimization of the DC Generator: The DC micro generator in the experimental system is not optimal. The electrical and mechanical properties were not

approximated from design methods or numerical simulations, but chosen intuitively to suit the compact assembly for easier experimentation. The application voltage, current, and power requirements as well as the spring design and its estimated torque output can be used to reverse engineer the properties of the DC generator for optimal power conversion. A DC generator can be fabricated specifically to suit the operation environment and be constrained in terms of space, type, rpm, and power requirements to obtain a better suited harvester system for any application.

APPENDICES

Appendix A

Derivation of Transfer Functions for Harvester System

A transfer function is a mathematical relationship that describes the response of a system's output to a supplied input. There are three main transfer function relationships that describe the power generation renewable energy device: 1) the mechanical response driven by the thermal domain, 2) the storage element behavior depending on the mechanical motion during the ratchet 'hold' period, and 3) the electrical output produced from the storage element input at ratchet release.

A-1. Transfer Function I

The mechanical output from the bellows (end plate displacement, x) for input ambient temperature change ($T - T_0$) or ΔT, where T_0 and T are the reference temperature and final temperature, respectively, is given by the end plate dynamics in response to the vapor pressure change in the bellows.

Riedel's equation relating vapor pressure, P_{ec}, and temperature, T, is given by

$$P_{ec} = e^{\left(A+\frac{B}{T}+ClnT+DT^{E}\right)} \tag{A.1}$$

where A, B, C, D, E are Riedel's equation 'curve fit' constants for ethyl chloride that have been empirically determined. The expression (A.1) can be rewritten using the mathematical property of Euler's number 'e' as

$$P_{ec} = e^{A}e^{\left(\frac{B}{T}+ClnT+DT^{E}\right)} \tag{A.2}$$

$$P_{ec} = \mu e^{\left(\frac{B}{T}+ClnT+DT^{E}\right)} \tag{A.3}$$

where $\mu = e^{A}$ is a constant multiplier independent of temperature.

Linearizing $e^{\left(\frac{B}{T}+ClnT+DT^{E}\right)}$ using Taylor series expansion about the reference temperature, T_0, results in

$$e^{\left(\frac{B}{T}+ClnT+DT^{E}\right)} = f_1(T_0) + f_2(T_0)(T - T_0) + \text{H.O.T} \tag{A.4}$$

where f_1 and f_2 are functions of reference temperature T_0. The notation H.O.T refers to higher order terms. From empirical calculations, it was noticed that eliminating the higher order terms do not have a significant impact in the approximation of the results and are thus not considered in the final representation of the linearized form, so that

$$P_{ec} = \mu[f_1(T_0) + f_2(T_0)(\Delta T)] \tag{A.5}$$

A simpler reduction of Riedel's equation (A.1) can be obtained by using a polynomial curve fit over the bellows typical operating temperature range. Assuming that the bellows operates between 280 K< T < 310K, the curve fitting was performed using first order and second order polynomials.

(a) First Order Polynomial: $P_{ec} = a_1T + a_2$ (A.6)

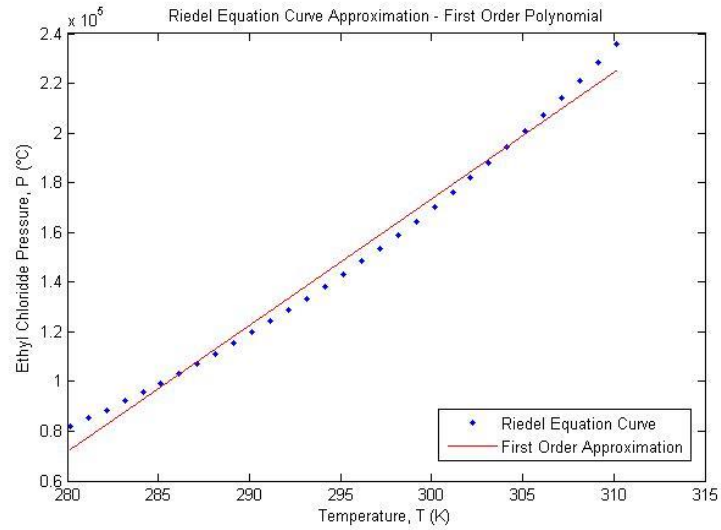

Figure A-1: First Order Polynomial Curve Fitting
(Coefficients a_1 = 5088, a_2 = -1.353e06)

(b) Second Order Polynomial: $P_{ec} = a_1T^2 + a_2T + a_3$ (A.7)

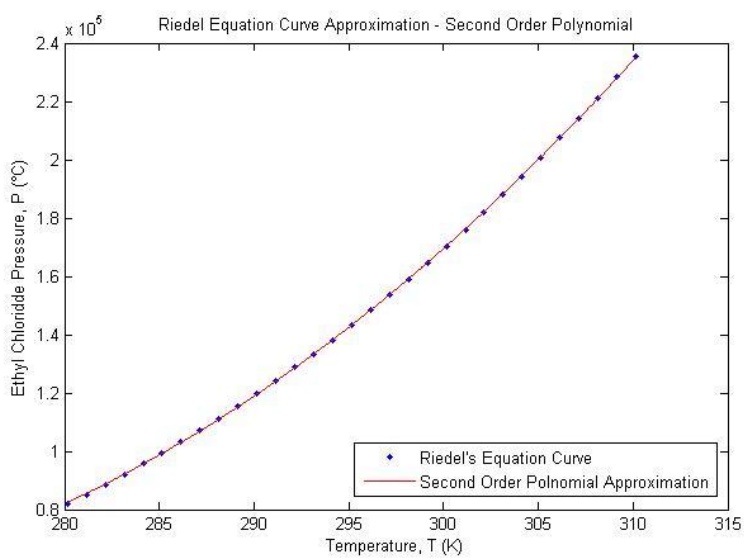

Figure A-2: Second Order Polynomial Curve Fitting
(Coefficients a_1 = 69.08, a_2 = -3.569e04, a_3 = 4.66e06)

The second order approximation can be seen to be more consistent with the Riedel equation model over the bellows operating temperature range but the first order approximation has been used in the calculations for the purpose of obtaining a more simplified expression to establish the basic concepts for this novel system.

It can be noted that the main difference in the results of the two linearization techniques is that Taylor Series expansion can provide insight into the vapor pressure behavior in terms the temperature variation, ΔT, while the polynomial curve fit provides a current temperature to pressure relationship.

The bellows end plate dynamics can be given by

$$m\frac{d^2x}{dt^2} + c\frac{dx}{dt} + (k_{es} + k_{bs})x = A_p(P_{ec} - P_{atm}) \tag{A.8}$$

Replacing the variable P_{ec} in (A.2) with expression (A.6) results in

$$m\frac{d^2x}{dt^2} + c\frac{dx}{dt} + (k_{es} + k_{bs})x = A_p a_1 T + A_p(a_2 - P_{atm}) \tag{A.9}$$

Assuming that the $(a_2 - P_{atm})$ can be written as a delta function and its contribution can be neglected, the transfer function representation of the above expression(s) in the Laplace domain is given by

$$\left(ms^2 + cs + (k_{es} + k_{bs})\right)x(s) = \left(a_1 A_p\right)T(s) + 1 \tag{A.10}$$

Contribution of the delta function is neglected and the above equation(s) can be written as the transfer function

$$\frac{x(s)}{T(s)} = \left(\frac{1}{ms^2 + cs + (k_{es}+k_{bs})}\right)\left(a_1 A_p\right) \tag{A.11}$$

A-2. Transfer Function II

The output coil spring rotational displacement, θ_6, through the drivetrain due to the input bellows end plate displacement, x, may be described by using a transfer function. The rack displacement and the bellows end pate displacement are assumed to be equal (i.e., there is no mechanical loss between the bellows system and the drivetrain assembly). The drivetrain dynamics are given by

$$m_r \frac{d^2x}{dt^2} + c_r \frac{dx}{dt} = F_{GT} \tag{A.12}$$

$$F_{GT} = \frac{k_s}{(R^* r_1 R_{56})} \theta_6 \; ; R^* = \begin{cases} 1 & , \dot{x} \geq 0 \\ R_{34} & , \dot{x} < 0 \end{cases} \tag{A.13}$$

Replacing F_{GT} in (A.12) with (A.13) provides

$$m_r \frac{d^2x}{dt^2} + c_r \frac{dx}{dt} = \frac{k_s}{R^* r_1 R_{56}} \theta_6 \tag{A.14}$$

The representation of (A.14) in the Laplace domain is given by

$$(ms^2 + cs)x(s) = \left(\frac{k_s}{R^* r_1 R_{56}}\right) \theta_6(s) \tag{A.15}$$

Rewriting (A.15) as a ratio of the input to the output (transfer function representation) yields

$$\frac{\theta_6(s)}{x(s)} = \left(\frac{r_1 R^* R_{56}}{k_s}\right) \left(s(m_r s + c_r)\right) \tag{A.16}$$

It can be observed that the above system is anti-causal (poles < zeroes) and only possible as a mathematical description and not in the physical system. This effect is attributed to the assumption of ideal gears in the compound gear train that drives the spring, which is not true in the physical system. Therefore, the stiffness rate, k_r, rotational inertia,

J_1, and damping, b_1, are re-introduced into the dynamic descriptions for the gear train and spring to simulate the response, so that

$$m_r \frac{d^2x}{dt^2} + c_r \frac{dx}{dt} + k_r x = J_1 \frac{d^2\theta_6}{dt^2} + b_1 \frac{d\theta_6}{dt} + \frac{k_s}{R^* r_1 R_{56}} \theta_6 \tag{A.17}$$

This approach allows the transfer function to be expressed as

$$\frac{\theta_6(s)}{x(s)} = \left(\frac{m_r s^2 + c_r s + k_r}{J_1 s^2 + b_1 s + \left(\frac{k_s}{r_1 R^* R_{56}}\right)} \right) \tag{A.18}$$

Finally, the poles arising from the inertia, J_1, and damping, b_1, are assumed to be very small and the response of the system is generated as shown in Figure A.6.

A-3. Transfer Function III

The output current generated in the circuit due to the coil displacement has a corresponding transfer function based on the input shaft rotation, θ_7, and the generator output current, i_a.

The generator electrical dynamics is given by

$$L_a \frac{di_a}{dt} + R_a i_a + R_L i_a = k_b \frac{d\theta_8}{dt} \tag{A.19}$$

The generator shaft is related to the barrel gear through gear ratio, R_{78}, and is given by

$$R_{78} = \frac{N_8}{N_7} = \frac{r_8}{r_7} = \frac{\tau_8}{\tau_7} = \frac{\omega_7}{\omega_8} \tag{A.20}$$

Therefore, the Laplace representation of (A.19) becomes

$$\left(L_a s + \tilde{R}\right) i_a(s) = \left(\frac{k_b}{R_{78}}\right) \theta_7(s) \tag{A.21}$$

Rewriting the θ_7 in terms of θ_6

$$\frac{i_a(s)}{\theta_6(s)} = \left(\frac{k_b}{R_{78}}\right)\left(\frac{1}{L_a s+\tilde{R}}\right) \tag{A.22}$$

A-4. Transfer Function IV

The overall system transfer function can be obtained by replacing *x(s)* in terms of $i_a(s)$ in (A.11) and manipulating the expressions (A.18) and (A.22) such that a transfer function relationship between and generated current, i_a, and temperature, T, can be obtained as

$$\frac{i_a(s)}{T(s)} = \left(\frac{i_a(s)}{\theta_6(s)}\right)\left(\frac{\theta_6(s)}{x(s)}\right)\left(\frac{x(s)}{T(s)}\right) \tag{A.23}$$

Through mathematical substitutions and simplifications, it can be shown that A.23 becomes

$$\frac{i_a(s)}{T(s)} = \left(\left(\frac{k_b}{R_{78}}\right)\left(\frac{1}{L_a s+\tilde{R}}\right)\right)\left(\frac{m_r s^2+c_r s+k_r}{J_1 s^2+b_1 s+\left(\frac{k_s}{r_1 R^* R_{56}}\right)}\right)\left(\left(\frac{1}{ms^2+cs+(k_{es}+k_{bs})}\right)\left(a_1 A_p\right)\right) \tag{A.24}$$

$$\frac{i_a(s)}{T(s)} = \left(\frac{a_1 A_p k_b}{R_{78}}\right)\left(\frac{m_r s^2+c_r s+k_r}{(L_a s+\tilde{R})\left(ms^2+cs+(k_{es}+k_{bs})\right)\left(J_1 s^2+b_1 s+\frac{k_s}{r_1 R^* R_{56}}\right)}\right) \tag{A.25}$$

(NOTE: Generator internal gear ratio can be added as a gain to the electrical generator dynamics if applicable to the system as seen in Chapter 4)

Appendix B

MATLAB Programs

The dynamic model was recreated using the Mathworks software package MATLAB/Simulink. Three algorithms were used throughout the development of the harvester system – 1) Generation of model parameter values for Simulink Model and result collection, manipulation, and data visualization, 2) Riedel vapor pressure model linearization using 1° and 2° polynomial curve fit, and 3) Transfer function response models and visualization.

B-1. Simulation Code with Sample Parameter Values

```
clear all

% Atmospheric Pressure and Temperature
  P_atm = 1.013e-5; % Pa
  temp = 1;         % C
  T_amb = 295.15;   % K

% Ethyl Chloride Properties and Riedel's Equation Constants
  n = 0.28;         % mol
  R = 8.314;        % mol/K
  A = 44.67;        % Riedel's Constant
  B = -4026;        % Riedel's Constant
  C = -3.371;       % Riedel's Constant
  D = 2.273e-17;    % Riedel's Constant
  E = 6;            % Riedel's Constant

% Bellows Design Parameters
  A_p = 0.002;    % End Plate Area (m)
  V_b = 8e-05;    % Volume (m^3)
  m = 0.2;        % End Plate Mass (Kg)
  c = 18;         % End Plate Viscous Damping (Ns/m)
  k_b = 120;      % Bellows Spring Rate (N/m)
  k_es = 500;     % External Spring Stiffness (N/m)

% Bellows End Plate and Rack Gear Interconnect Stiffness (N/m)
  k_r = 1500;
```

```
% Rack and Drivetrain Parameters
 m_r = 0.02;     % Mass of Rack Gear (Kg)
 c_r = 2;        % Viscous Damping of Rack (Ns/m)
 r_1 = 26.5e-03; % Radius of Pinions (m)

% Gear Ratios
 R_34 = 3;
 R_56 = 1.65; %3.75
 R = 1/((r_1*R_34*R_56));

% Mainspring stiffness (Nm/rad)
 k_s = 9.75e-05;

% Gear Ratio: Mainspring Barrel to Generator Shaft Gear
 R_78 = 2;

% Generator Constants
 Phi = 1.5;     % Rated Voltage (V)
 k_t = 6e-03;   % Generator Torque Constant (Nm/A)
 k_v = 6e-03;   % Generator Voltage Constant (Vrad/s)
 L_g = 3e-05;   % Inductance (H)
 J_e = 8e-05;   % Equivalent Inertia (Nm)
 C_e = 3e-05;   % Rotational Damping (Ns/rad)
 R_L = 5;       % Load Resistance (Ohms)
 R_a = 1;       % Armature Resistance (Ohms)
 R_sa = 5;      % Internal Gear Ratio of Generator

% Hold Cycle Time
 time = 15;

% Command Line Simulation Call
 options = simset('SrcWorkspace','current');
 Sim_Res = sim('EH_Dynamic_Simulations',[],options);


% Outputs
 % Temperature in Degree Celsius
  T_C = T - 273.15;
 % Bellows End Plate Displacement and Rack Displacement in cm
  x_cm = x*100;
  x_r_cm = x_r*100;
 % Power Calculations
  Power = i_a*v_l;
 % Data Manipulation for Smaller Ranges
  tau_8_mm = tau_8*1000;
  Power_mW = Power*1000;
  i_a_mA = i_a*1000;


% Output Graphs
 fig1 = figure(1);
```

```
 axis([0,12,21,23])
 plot(T_C)
 %title('Ambient Temperature Profile')
 xlabel('Time (hours)')
 ylabel('Ambient Temperature, T (°C)')

fig2 = figure(2);
 axis([0.05,1,-2.05,1.25])
 plot(x_r_cm)
 %title('Resultant Rack Displacement')
 xlabel('Time (hours)')
 ylabel('Rack Displacement, x_{r} (cm)')

fig3 = figure(3);
 axis([0,12,0,12.5])
 plot(theta_6)
 %title('Input Mainspring Coil Deflection')
 xlabel('Time (hours)')
 ylabel('Spring Shaft Rotational Displacement, {\theta}_{6} (rads)')


fig4 = figure(4);
 axis([23.99,25.5,0,2])
 plot(tau_8_mm)
 %title('Generator Torque Input from Mainspring through Gear G_{8}')
 xlabel('Time (seconds)')
 ylabel('Generator Torque Input, {\tau}_{8} (Nmm)')


fig5= figure(5);
 axis([24,29,0,10])
 plot(Power_mW)
 %title('Generated Power at Output')
 xlabel('Time (seconds)')
 ylabel('Generated Power, P (mW)')


fig6 = figure(6);
 line(i_a_mA.Time,i_a_mA.Data)
 ax1 = gca;
 ax1.XColor = 'k';
 ax1.YColor = 'k';
 axis([24,29,0,45])
 %title('Power Generation Circuit Values')
 xlabel('Time (seconds)')
 ylabel('Generated Current, i_{a} (mA)')
 hold on
 ax2 = axes('YAxisLocation','right','Color','none');
 line(theta_8.Time,theta_8.Data,'Parent',ax2,'Color','m')
 axis([24,29,0,80])
 ylabel('Rotational Displacement of Generator Armature,{\theta}_{8} (rads)')
```

```
saveas(fig1,'Temperature.jpeg');
saveas(fig2,'Displacement.jpeg');
saveas(fig3,'Spring Displacement.jpeg');
saveas(fig4,'Release Torque.jpeg');
saveas(fig5,'Power.jpeg');
saveas(fig6,'Generator Current and Shaft Speed.jpeg');

save('run.mat')
```

B-2. Code for Linear Approximations/Curve Fit for Riedel's Vapor Pressure Equation

```
clear all

% Riedel's Vapor Pressure Equation Constants for Ethyl Chloride
  A = 44.67;
  B = -4026;
  C = -3.371;
  D = 2.273e-17;
  E = 6;

% Bellows (Assumed) Operating Temperature Range
  T = 280.15:1:310.15;
% Riedel's Vapor Pressure Equation
  P_ec = exp(A + (B./T) + (C.*log(T)) + D.*(T.^E));

% Curve Fit to Obtain Linear/Algebraic Model
 [P_ec_LA1,gof1] = fit(T',P_ec','poly1');
 [P_ec_LA2,gof2] = fit(T',P_ec','poly2');

% Output graphs
  fig1 = figure(1);
   plot(P_ec_LA1,T,P_ec)
   title('Riedel Equation Curve Approximation - First Order Polynomial')
   xlabel('Temperature, T (K)')
   ylabel('Ethyl Chloridde Pressure, P (°C)')

  fig2 = figure(2);
   plot(P_ec_LA2,T,P_ec)
   title('Riedel Equation Curve Approximation - Second Order Polynomial')
   xlabel('Temperature, T (K)')
   ylabel('Ethyl Chloridde Pressure, P (°C)')

saveas(fig1,'First Order PolyFit.jpeg');
saveas(fig2,'Second Order PolyFit.jpeg');
save('LA_Riedel.mat');
```

B-3. Code for Transfer Function Response with Sample Parameter Values

```
clear all

  P_atm = 1.013e-5;   % Atmospheric Pressure
  beta_1 = 50;
% First Order Polyfit COnstants
  alpha = 5088;
  beta = abs(-1.353e06 - P_atm);

% Critical Design Variables
  A_p = 0.005;        % End Plate Area(m^2)
  m = 0.2;            % End Plate Mass(Kg)
  c = 18;             % End Plate Viscous Damping(Ns/m)
  k_b = 250;          % Bellows Spring Rate(N/m)
  k_es = 900;         % External Spring Stiffness (N/m)
  k_r = 195;          % Bellows End Plate and Rack Gear Interconnect Stiffness (Nm/rad)
  m_r = 0.02;         % Mass of Rack Gear (Kg)
  c_r = 2;            % Viscous Damping of Rack (Ns/m)
  r_1 = 26.5e-03;     % Radius of Pinions (m)
  R_34 = 1.00;        % Gear ratio between G3 and G4
  R_56 = 3.75;        % Gear ratio between G5 and G6
  %R = 1/((r_1*R_34*R_56));
  k_s = 6.95e-03;     % Coil Spring Stiffness (Nm/rad)
  Theta_max = 31.41;  % Maximum Number of Coil Turns (rad)
  R_78 = 0.47;        % Gear Ratio: Mainspring Barrel to Generator Shaft Gear
  k_t = 2.5e-03;      % Generator Torque Constant(Nm/A)
  k_v = 5.2e-03;      % Generator Volatge Constant(Vrad/s)
  L_g = 5.5e-05;      % Inductance(H)
  J_e = 8e-05;        % Equivalent Inertia(Nm)
  C_e = 3e-05;        % Rotational Damping(Ns/rad)
  R_L = 100;          % Load Resistance(Ohms)
  R_a = 1;            % Armature Resistance(Ohms)
  R_sa = 4.7;         % Internal Gear Ratio

% Constants for Transfer Function
  k_bar = k_es+k_b;                 % Equivalent Stiffness (N/m)
  a1 = (k_s)/(r_1*R_34*R_56);       % Equivalent Stiffness Term (N/rad)
  J_1 = 0.1e-04;                    % Spring Dynamics Inertia (Kgm/rad)
  b_1 = 3e-04;                      % Spring Dynamics Damping (Ns/rad)
  a2 = (k_v/R_78);                  % Generator Dynamics Constant (Vrad/s)
  R_bar = (R_L + R_a);              % Equivalent Resistance (Ohms)

% Temperature Response
  num1 = A_p*alpha;        % Transfer Function Numerator
  den1 = [m c k_bar];      % Transfer Function Denominator
  G1 = tf(num1,den1);      % Transfer Function
  % num1_1= A_p*beta;
  % G5 = tf(num1_1,den1);
  % G6 = G1 + G5;
  % num3_1t = [A_p*beta*m (A_p*beta*c)];
```

```
% Spring Response
 num2 = [m_r c_r 0];            % Transfer Function Numerator
 den2 = [J_1 b_1 a1];           % Transfer Function Denominator
 G2 = 1e-03*tf(num2, den2); % Gain added to decrease x from m to cm

% Generator Response
  num3 = R_sa*a2;       % Transfer Function Numerator
  den3 = [L_g R_bar];   % Transfer Function Denominator
  G3 = tf(num3,den3);   % Transfer Function

% System Response
  G3_1 = Theta_max*G3;
  G4 = G2.*G3_1;                  % Transfer Function Result from Spring to Generator
  H = 0.533*G4.*G1;               % Transfer Function of System, i_a(s)/T(s)
  P = beta_1*(R_bar*H).*H;     % Transfer Function of System, P(s)/T(s)


% Figures
  fig1 = stepplot(G1);
  fig2 = stepplot(G2);
  fig3 = stepplot(G3);
  fig4 = stepplot(H);
  setoptions(fig1,'Normalize','On')
  setoptions(fig2,'Normalize','On')
  setoptions(fig3,'Normalize','On')
  setoptions(fig4,'Normalize','On')
  setoptions(fig5,'Normalize','On')
  saveas(fig1,'x_T','-djpeg');
  saveas(fig2,'Theta6_x','-djpeg');
  saveas(fig3,'Current_Theta6','-djpeg');
  saveas(fig4,'Current_T','-djpeg');

  save('response.mat')
```

Appendix C

Simulink Model

The dynamic equations for the harvester device were used in simulation to study the behavior of the individual system components – the ethyl chloride filled mechanical bellows, the rack-bellows end plate interface, and the electromechanical assembly. These dynamic models were built using continuous time blocks. The input temperature profile for this study was a low frequency sine wave about 22°C.

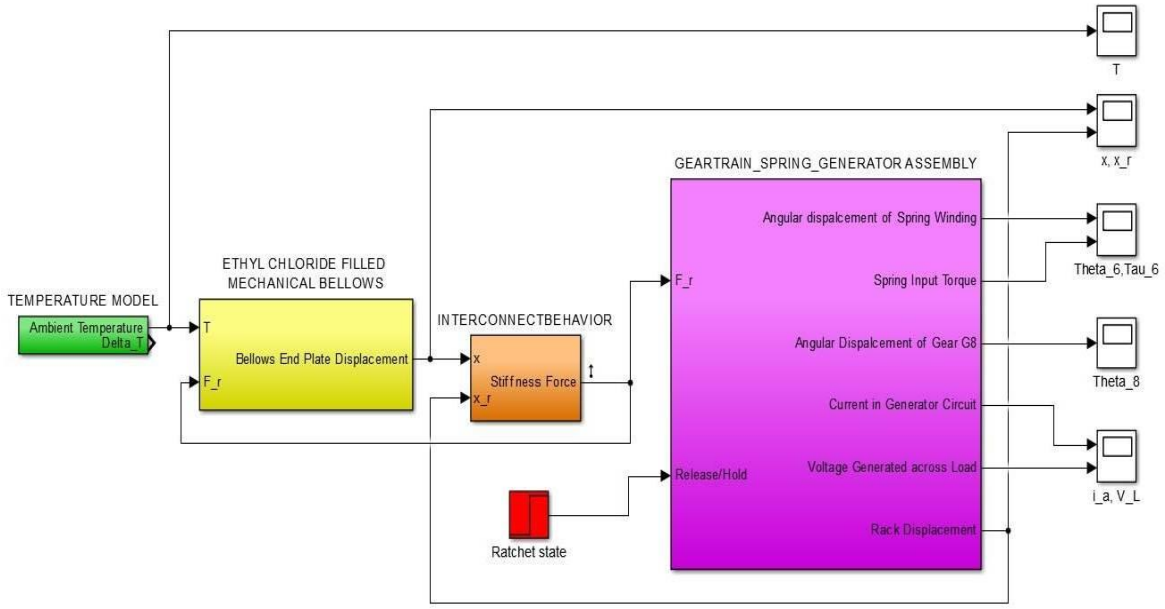

Figure C-1: High Level Diagram of Harvester System with Power Transformer

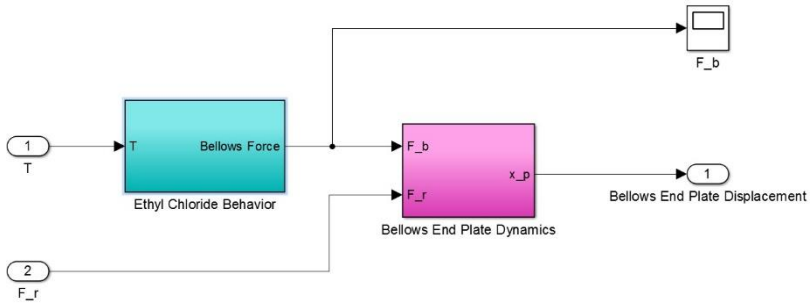

Figure C-2: Second Level Diagram (Ethyl Chloride Filled Mechanical Bellows)

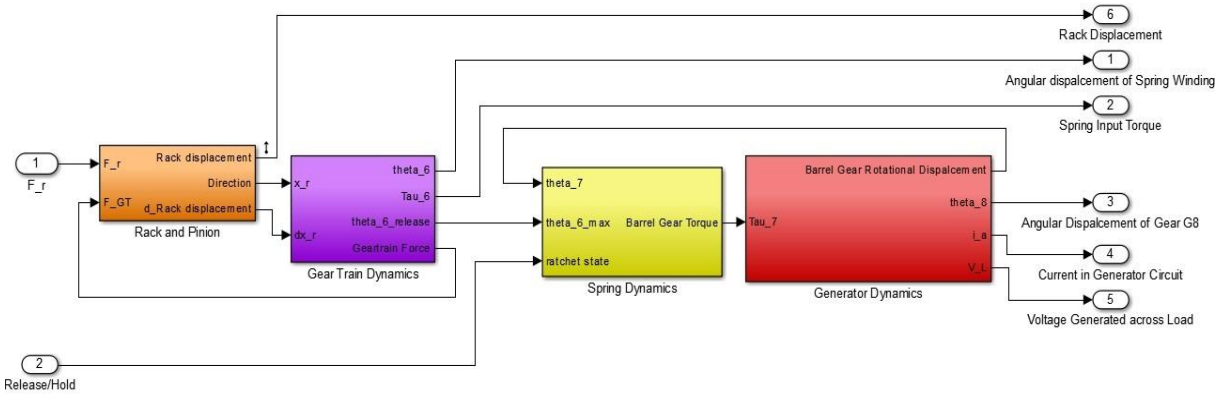

Figure C-3: Second Level Diagram (Gear Train, Spring, and DC Generator Assembly)

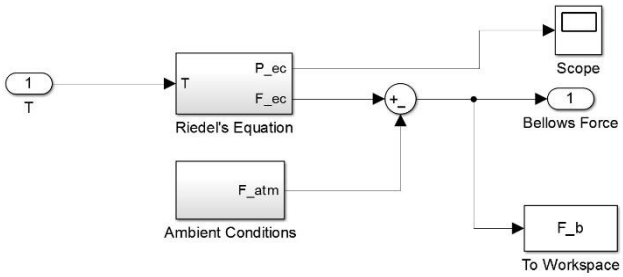

Figure C-4: Third Level Diagram (Ethyl Chloride Behavior)

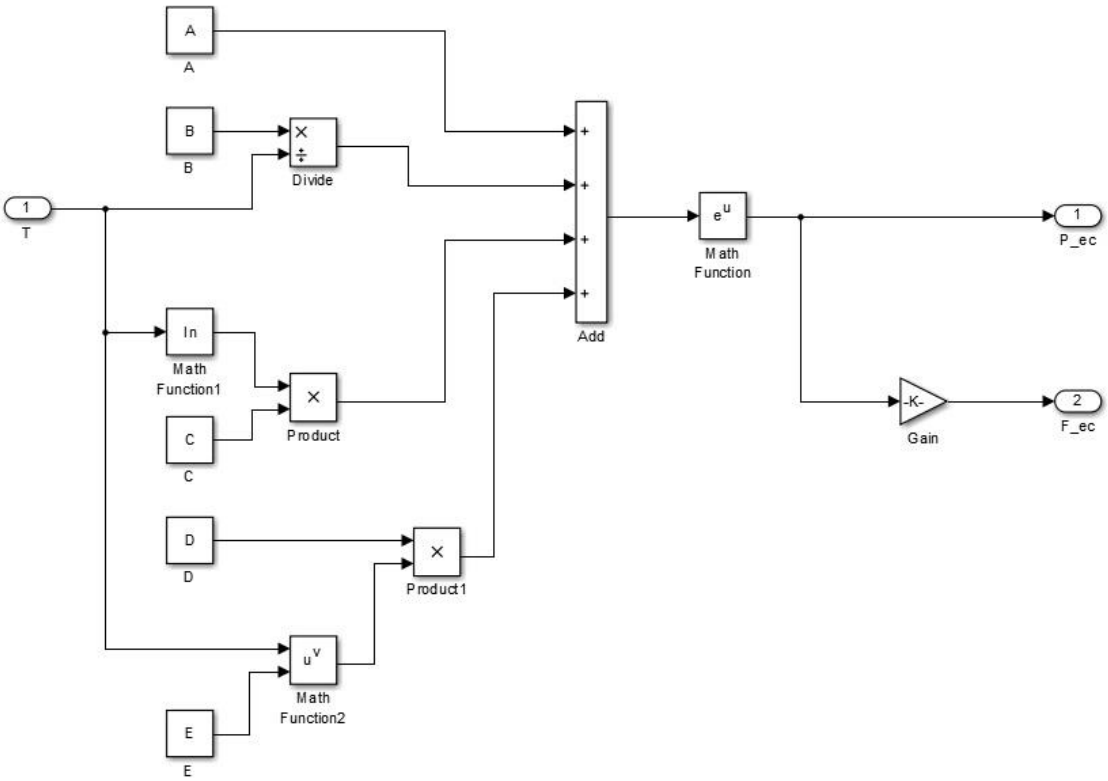

Figure C-5: Low Level Diagram (Riedel Model)

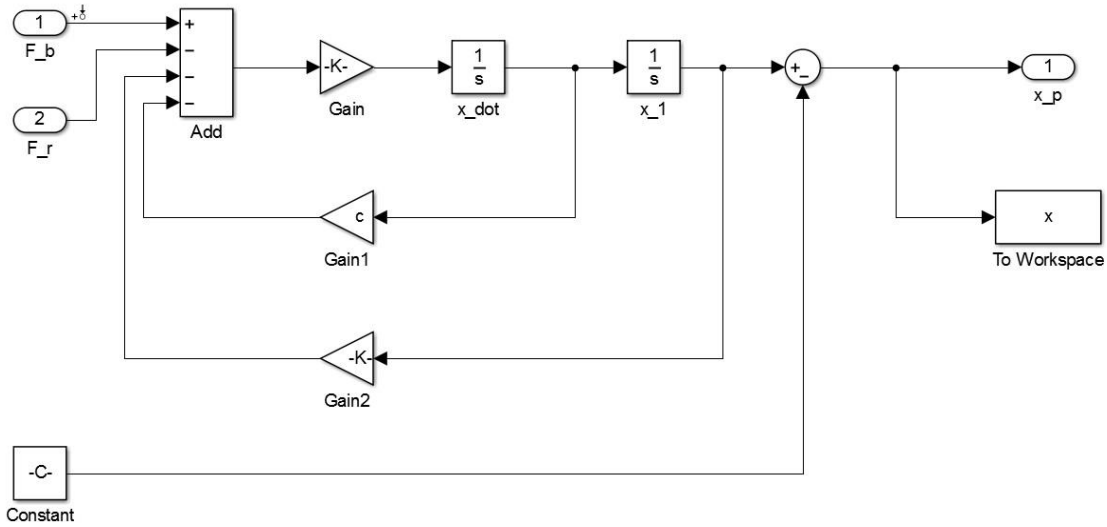

Figure C-6: Low Level Diagram (Bellows End Plate Dynamics)

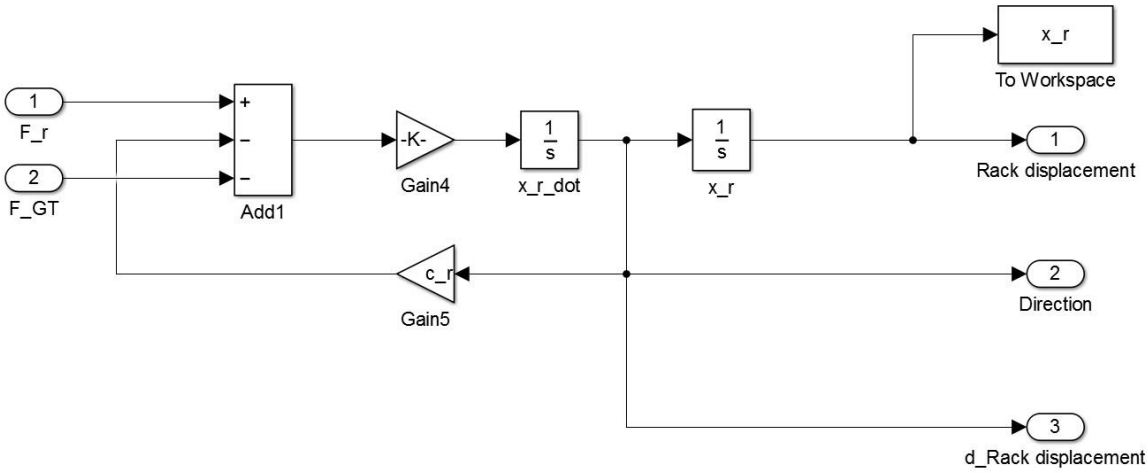

Figure C-7: Low Level Diagram (Rack and Pinion Dynamics)

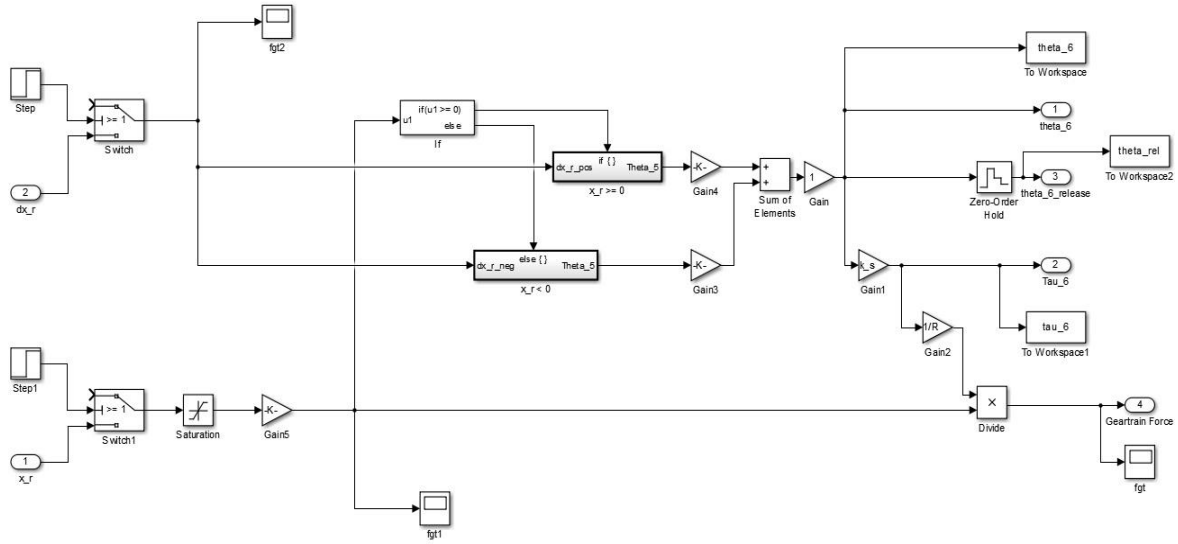

Figure C-8: Low Level Diagram (Gear Train Dynamics)

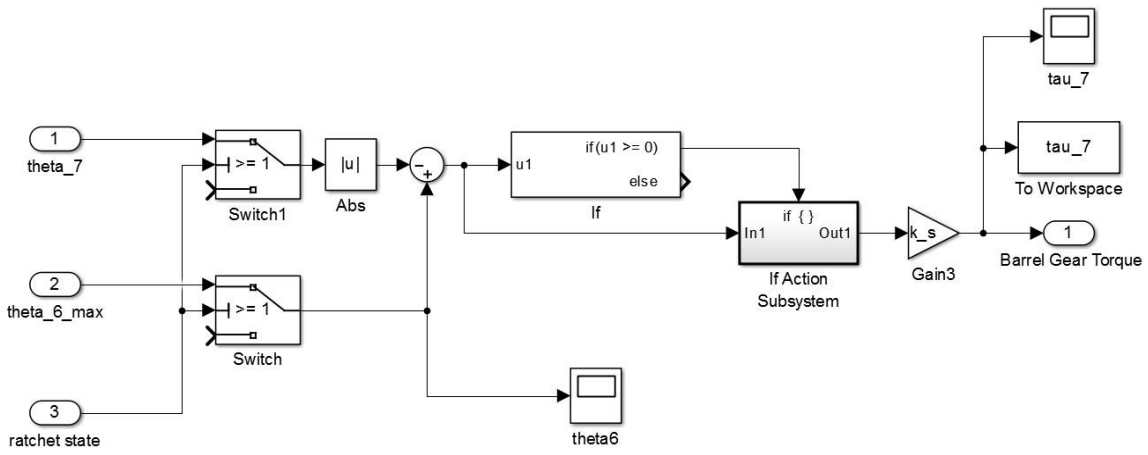

Figure C-9: Low Level Diagram (Spring Dynamics)

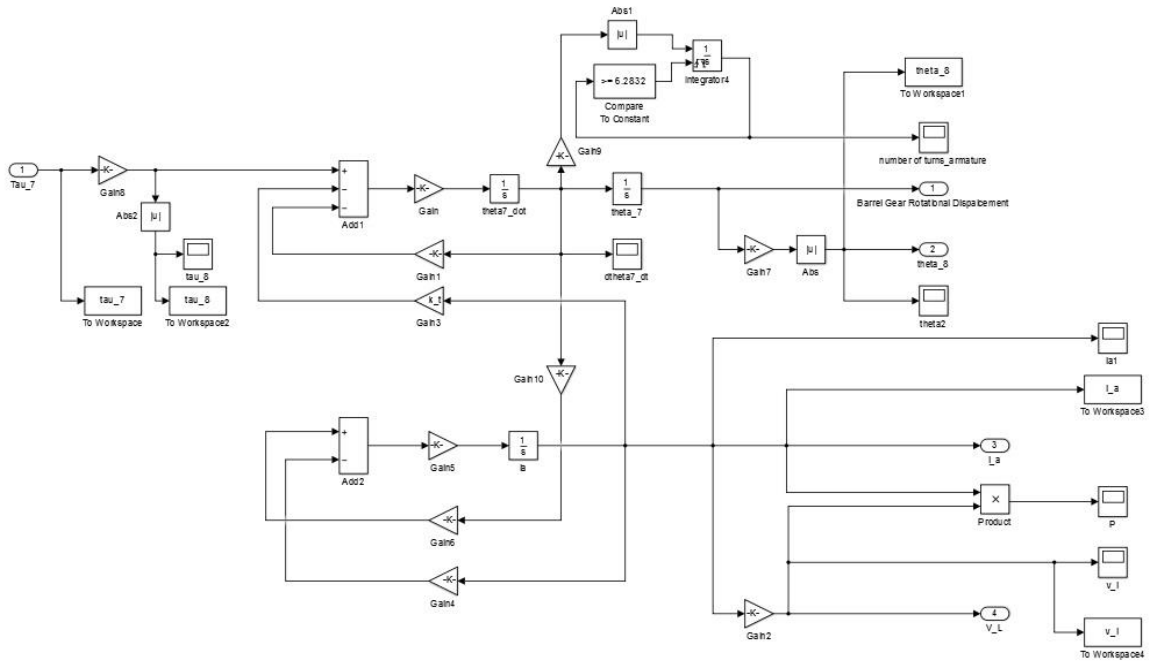

Figure C-10: Low Level Diagram (DC Generator Dynamics)

Appendix D

CAD Images of Power Transformer Components

The design for the power transformer components to build an experimental prototype was developed using Solidworks. This section contains 3D descriptions of some of the important components, especially ones that were not immediately recognizable in the experimental setup in Chapter 3.

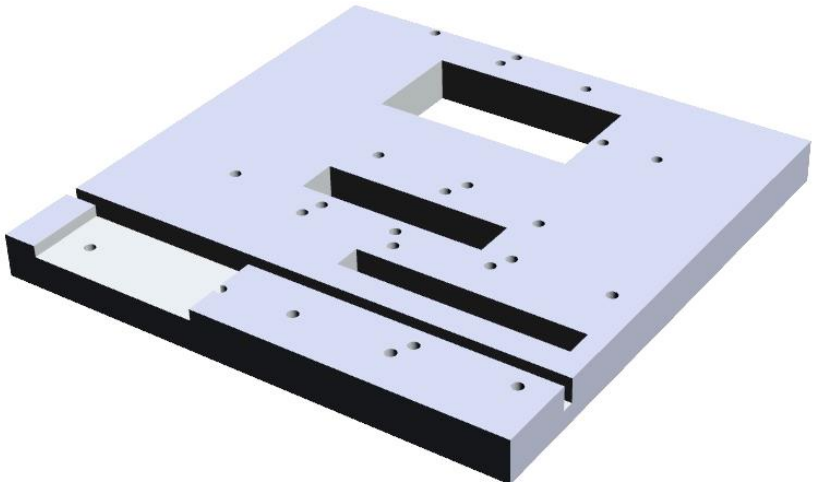

D-1: Aluminium Plate (6’’ x 6’’ x 0.25’’) with Holes and Cuts to Accommodate Gears, Spring, and Generator Mount

D-2: Rack Gear

D-3: Pinion Gear (48 Teeth) with Drilled Center to Accommodate One-Way Bearing

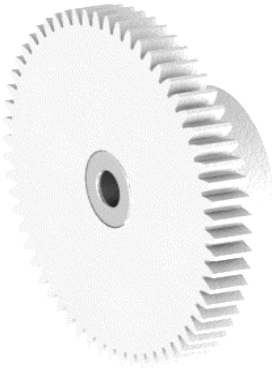

D-4: Secondary Gear (60 Teeth) on Shaft B with One-Way Bearing Placed Inside

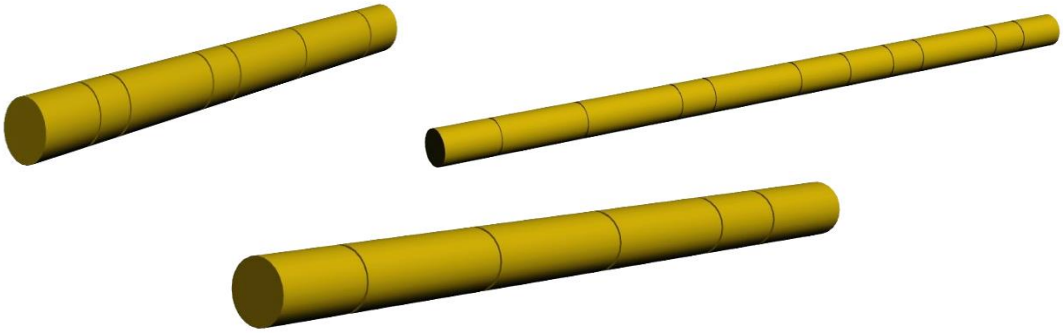

D-5: Shafts of the Compound Gear Train (From Top Left: A, B and C)

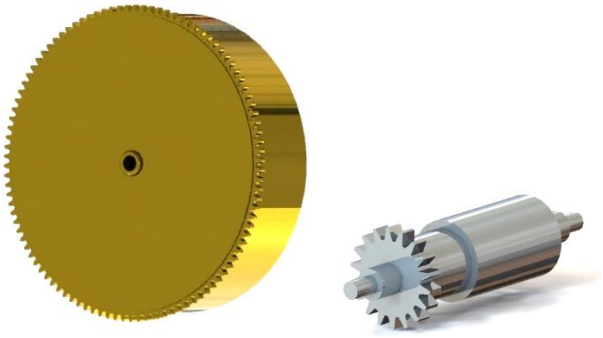

D-6: Mainspring Barrel and Key

D-7: Ratchet Assembly

D-8: DC Micro Generator

Appendix E

Development of Encoder Circuit to Measure Generator Shaft Speed

The generator shaft speed was a crucial quantity needed to be measured and calculate other values in the power generation circuit for the experimental system. To measure the rotational speed, an encoder was built using a Sunkee IR LED Emitter-Receiver pair, a Texas Instruments 747 Operational Amplifier, and Resistors (330 Ω, 1.5 kΩ) as shown in Figure E-1. The circuit was constructed as shown in Figure E-2. A four quadrant rotary encoder disc with one transparent quadrant was built using projector sheets and attached to the generator shaft. The emitter and collector were placed on opposite sides of the disc and held in place using electrical tape. Figure E-3 shows the physical experimental sensor circuit and the encoder disc between the emitter and receiver. The transparent edge of the encoder disc is detected for each revolution of the generator shaft as a voltage change in the receiver output as shown in Figure E-4. Analog 5V supply pins from the NI SCB 68 board powered the LEDs and resistances, and the op-amp was powered by an external power supply of 9V. This simple circuit efficiently detected the rotational motion of the generator shaft for the experimental tests.

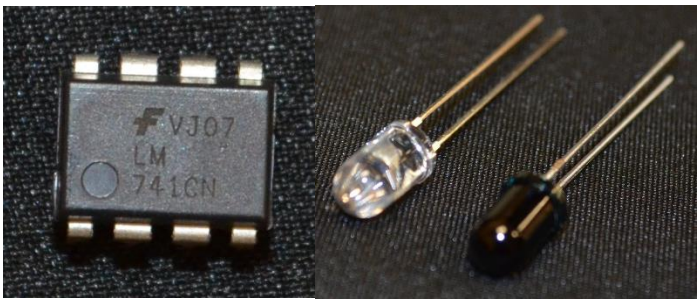

E-1: Rotary Encoder Experimental Circuit Key Components (Op-Amp and IR LED Emitter-Receiver Pair)

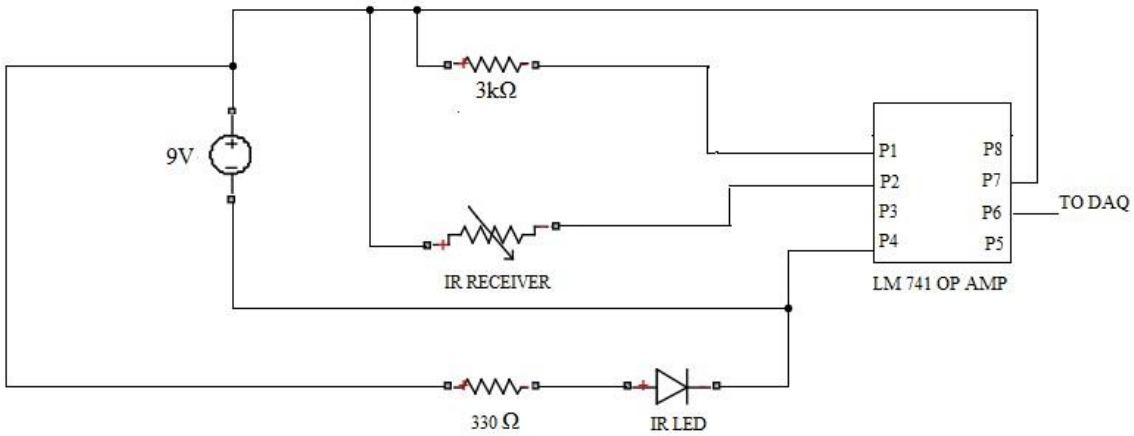

E-2: Encoder Circuit Diagram

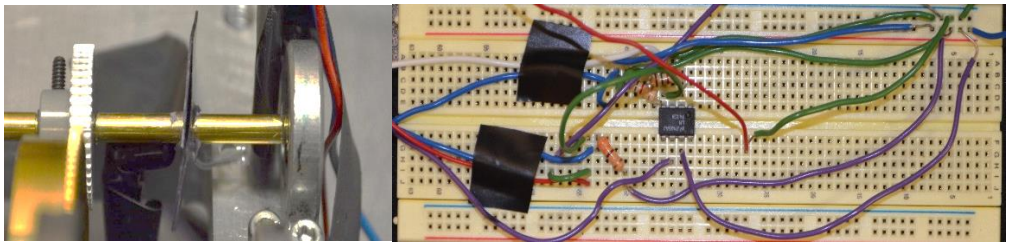

E-3: Physical Encoder Circuit

Appendix F

LabVIEW Program for the Experimental DAQ and Control

For the experimental system, sensors needed to be powered and data needed to be controlled and acquired. Post processing was required to visualize data for further understanding of the results. National Instruments software – LabVIEW – program (refer to Figure F-1 and F-2) was created to control the related I/O equipment, NI SCB 68 E series device which acquired sensory inputs, powered the sensors and controlled data in the experimental environment.

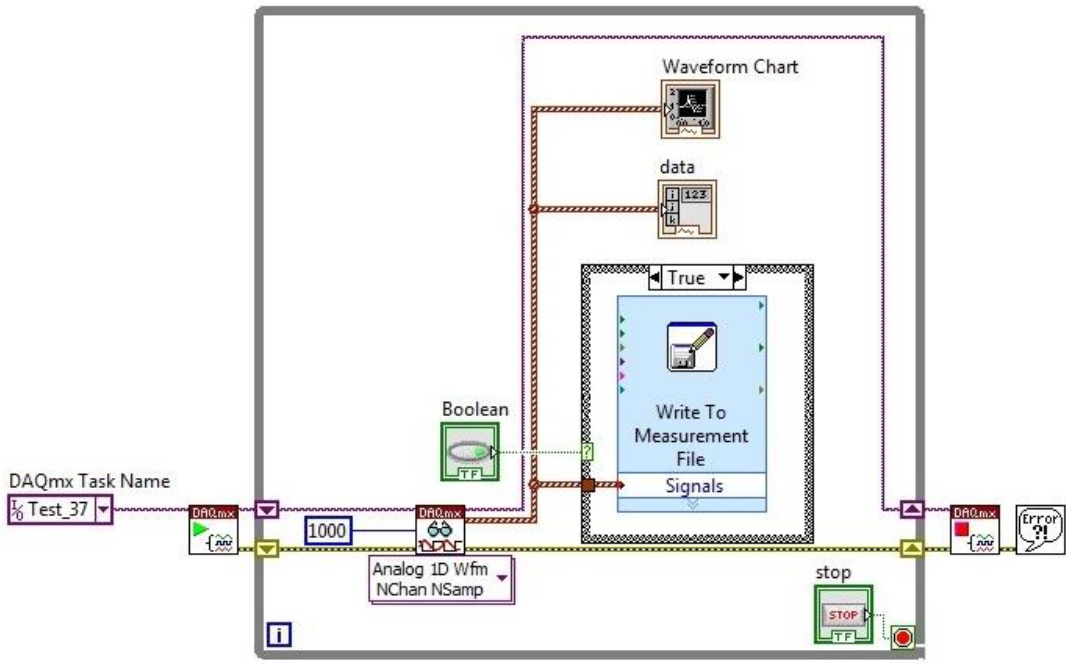

Figure F-1: Block Diagram of Visual Interface (VI) for Data Acquisition

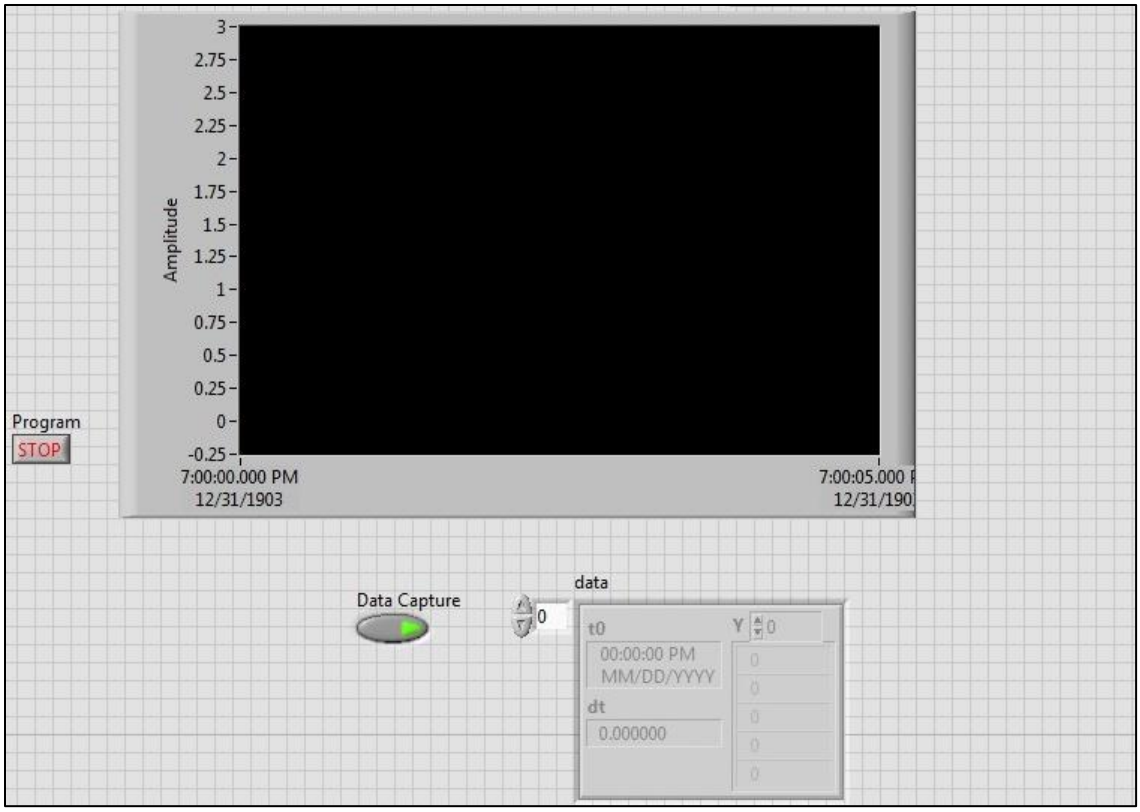

Figure F-2: Front Panel of Visual Interface for Data Monitoring

Description of VI and Panel:

The measurements recorded from the sensors were defined as tasks using the NI Measurement and Automation Explorer software that complements the NI SCB 68 DAQ allowing calibration, test, and visualization of the individual channels and their measurements. Parameters can be set for the data acquisition—desired channel (analog/digital), sampling frequencies, depending on the data points required (number of

sample) and time constraints (sampling rate) on each measurement; voltage/current upper and lower limits, scaling constants, type of input from channel, external resistance, etc.

Once the data acquisition parameters have been set, the process needed to be automated for real time run and data collection. The VI blocks in LabVIEW allow loop functions ('while' loop controlled here by user through the run and stop options/buttons) that enable continuous real time data logging. When the loop is run, the data can be logged into a desired output format (excel, text, etc.) and can be manipulated and visualized outside the program. The continuous time loop was run manually for each measurement separately and Boolean control (1-start and 0-stop) was used since the ratchet operation was not automated in the experimental system and the DAQ Analog-to-Digital (ADC) is blocked for each individual measurement. Three different tasks were created to obtain the outputs from the potentiometer, encoder, and voltage sensor to measure rack displacement, generator shaft speed, and output current/power, respectively. The front panel for the program is typically used to allow user inputs, control, and data processing/understanding. In this experiment, to understand, verify, and visualize real time data, waveform charts were used with numeric tables that displayed changing values for the measurement being recorded.

The code generation in the NI LabVIEW software is completely automated and the VI components used inherit all the required libraries to effectively run the program and automate/simplify the data acquisition process. The recorded data was converted to text files and imported into Microsoft Excel Spreadsheets/MATLAB to obtain graphical models and calculate critical parameters.

Appendix G

Supplementary Graphs from Testing

The encoder output voltage graph representing the number of complete revolutions of the generator shaft, the voltage and current graphs used in the power generation calculation in experimental testing are presented in this section. From the encoder output as shown in Figure G-1, the peaks correspond to complete revolutions of the generator shaft and the shaft speed can be measured.

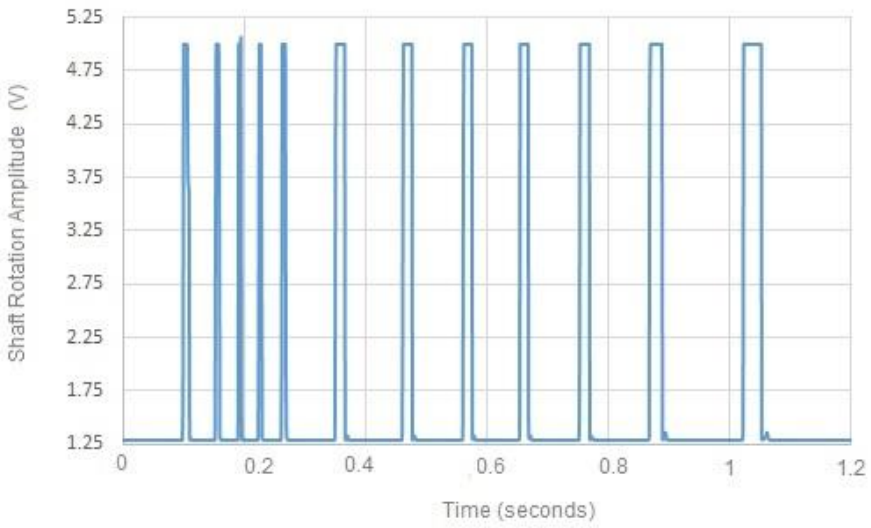

Figure G-1: Encoder Output Voltage (V) versus Time (s)

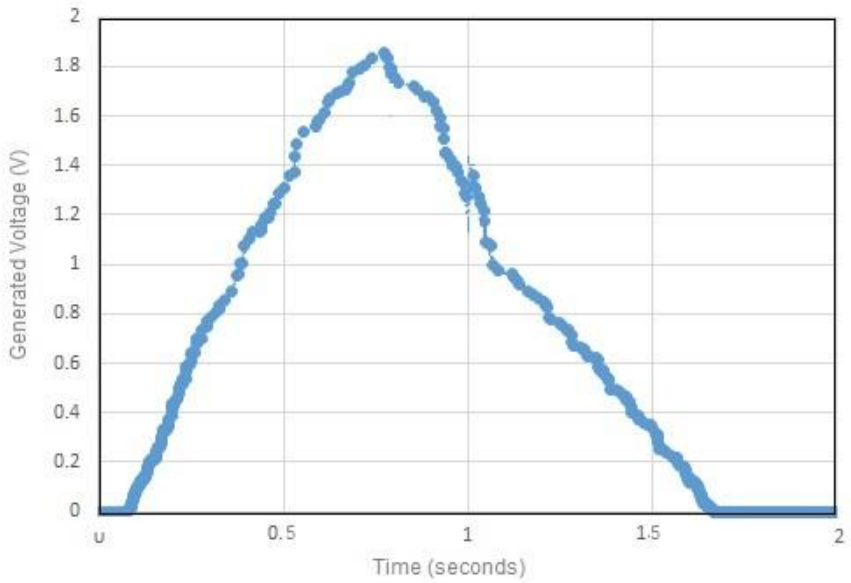

Figure G-2: Generated Voltage

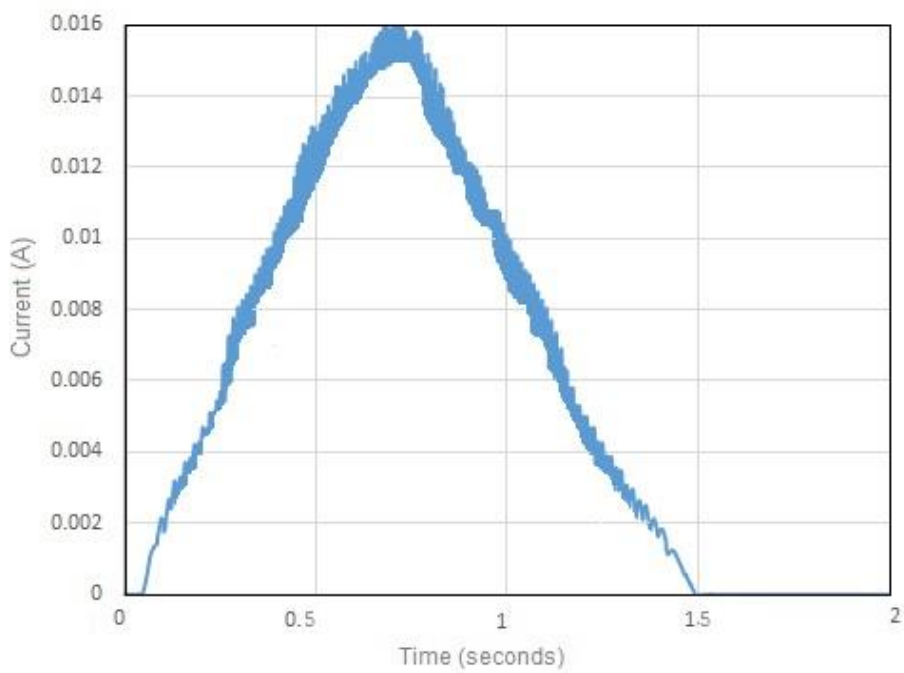

Figure G-3: Generated Current

Appendix H

Numerical Analysis – Case Studies on Design Parameters

Design parameters in in the electromechanical assembly design were varied and the resulting effect on the power generation capacities of the harvester system was studied. The original simulation parameters (Refer to Table 2.1) were used as a benchmark, and a design variable value was increased and decreased to observe its effects on power output. Some critical design values that largely influenced the power generation for a 24 hour harvesting period and a total temperature variation of 25°C are presented in this section.

H-1. Drivetrain: Pinion Radius, r_1, and Gear Ratio between Gears G_5 and G_6, R_{56}

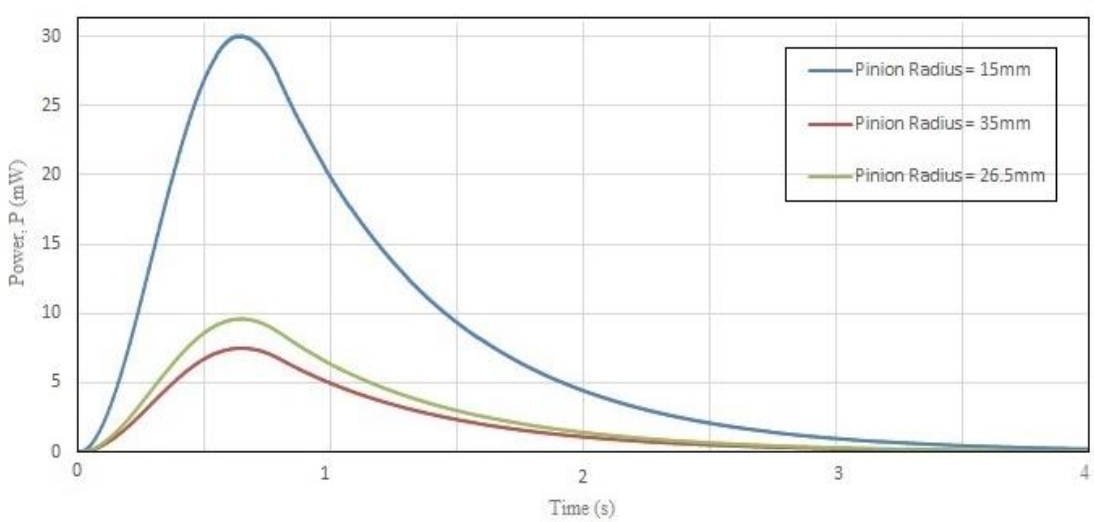

Figure H-1: Effect of Pinion Radius, r_1, on Generated Power, P

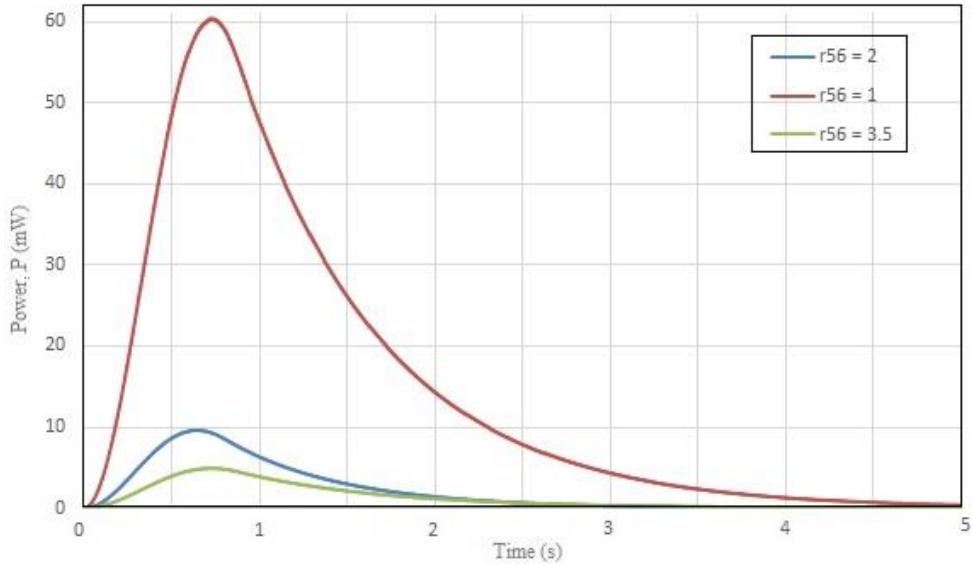

Figure H-2: Effect of Gear Ratio, R_{56}, on Generated Power, P

H-2. Spring: Coil Spring Stiffness, k_s

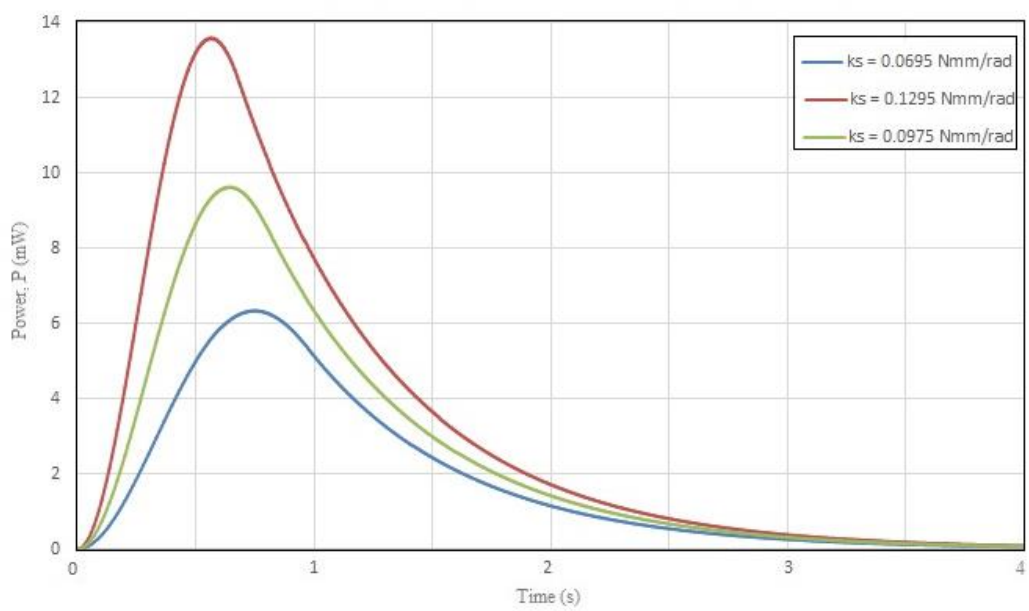

Figure H-3: Effect of Spring Coil Stiffness rate, k_s, on Generated Power, P

H-3. Power Generation Unit: Gear Ratio between Going Barrel Gear and Gear G_8, R_{78}, and Equivalent Generation Circuit Resistance, $\breve{R}$

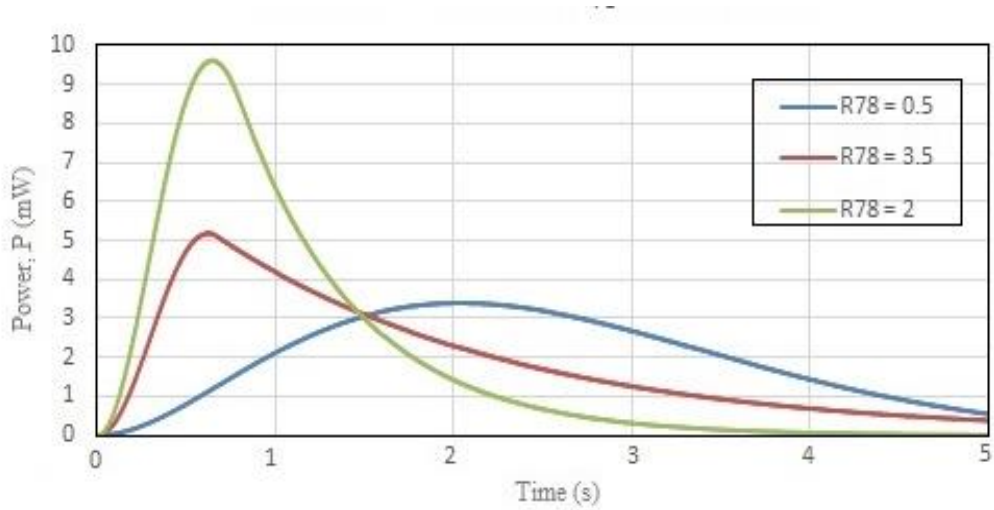

Figure H-4: Effect of Gear Ratio, R_{78}, on Generated Power, P

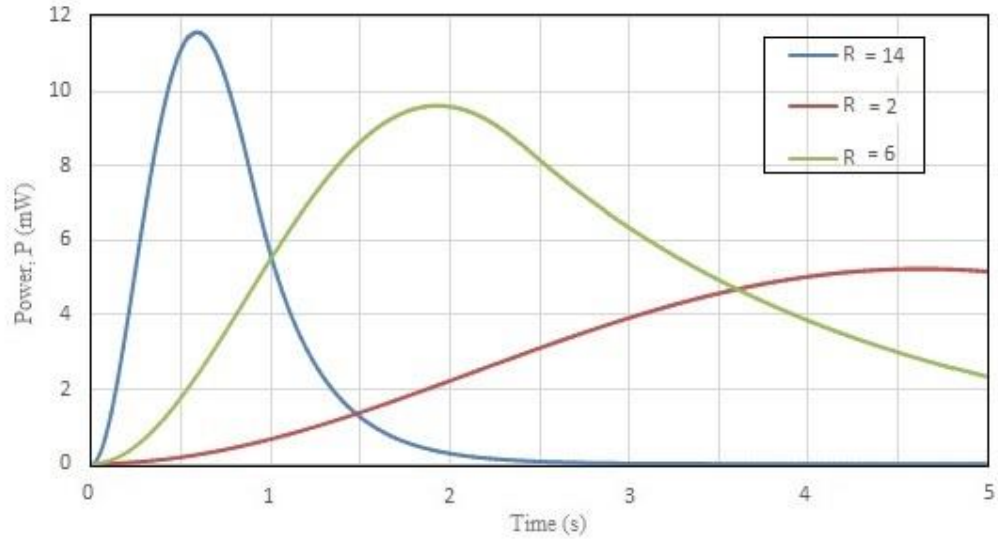

Figure H-5: Effect of Equivalent Generation Circuit Resistance, $\breve{R}$ on Generated Power, P

H-4. Power Generation Capacity with (Optimal) Parameters Borrowed from Design Case Studies

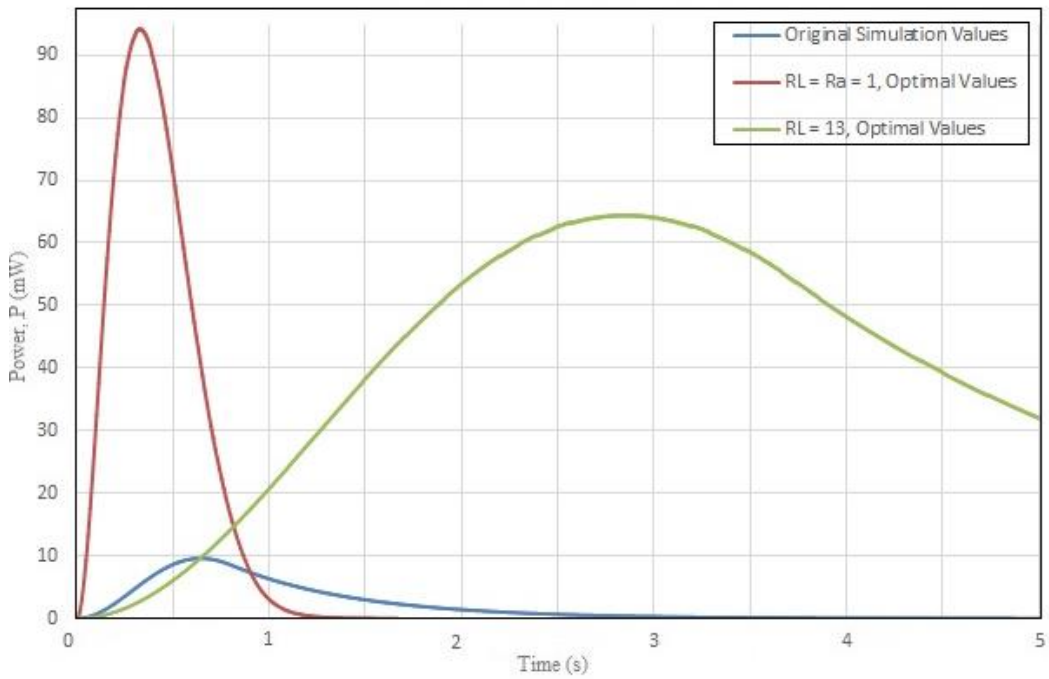

Figure H-6: Power Generation Capacities using Superior Parameters from Design Case Studies and Varying Load Resistance, R_L

Appendix I

Bill of Materials

The experimental prototype system parts are micro machined components made from lightweight materials. This section gives the parts list for the different components involved in the fabrication of the experimental electromechanical assembly and its accompanying test bench elements.

Table I.1: Parts List for Fabrication of Drivetrain

No.	Part	Supplier	Part No.	Description
1.	Rack Gear	Stock Drive Products and Sterling Instrument	A 1C 2-Y481	Material: Steel Pitch: 48 Pressure Angle: 20° Face Width: 0.125’’ Height: 0.125’’ Length: 6’’ Quantity: 1

2.	Pinion G_1, G_2	Stock Drive Products and Sterling Instrument	A 1P 2-Y48048A	Material: Acetal Brass Inserts Hub: Pin Hub Radius: 1.043’’ Pitch: 48 Pressure Angle: 20° Teeth: 48 Bore Diameter: 0.125’’ Hub Diameter: 0.625’’ Face Width: 0.125’’ Quantity: 2
3.	Gear G_3, G_4	Stock Drive Products and Sterling Instrument	A 1P 2-Y48060A	Material: Acetal Brass Inserts Hub: Pin Hub Radius: 1.276’’ Pitch: 48 Pressure Angle: 20° Teeth: 60 Bore Diameter: 0.125’’ Hub Diameter: 0.625’’ Face Width: 0.125’’ Quantity: 2

4.	Gear G_5	Stock Drive Products and Sterling Instrument	A 1T 2-Y48020	Material: Acetal Brass Inserts Hub: Pin Hub Radius: 0.450’’ Pitch: 48 Pressure Angle: 20° Teeth: 20 Bore Diameter: 0.125’’ Hub Diameter: 0.344’’ Face Width: 0.125’’ Quantity: 2
5.	Gear G_6	Stock Drive Products and Sterling Instrument	A 1P 2-Y48075A	Material: Acetal Brass Inserts Hub: Pin Hub Radius: 1.44’’ Pitch: 48 Pressure Angle: 20° Teeth: 75 Bore Diameter: 0.125’’ Hub Diameter: 0.750’’ Face Width: 0.125’’ Quantity: 2
6.	Shaft	McMaster-Carr	2575T1	Material: Brass Diameter: 0.125’’ Length: 36’’ Quantity: 1

7.	Mounted Pillow Block with Ball Bearing	McMaster-Carr	8600N1	Material: Aluminium, Steel Center Height: 0.375’’ Width: 0.2’’ Length: 1.43’’ Height: 0.75’’ Shaft Diameter: 0.125’’ Mounting Hole: 0.125’’ Quantity: 9
8.	One-Way Bearings	Amazon Supply (Koyo)	RC-02 (B007EE46PA)	Material: Plastic Width: 0.236’’ Outer Diameter: 0.281’’ Bore Diameter: 0.125’’ Quantity: 3
9.	Cup-Point Set Screws	McMaster-Carr	92311A078	Material: 18-8 Stainless Steel Head type: Headless Thread Type: UNC, Class 3A Size: 2-56 Length: 0.3125’’ Drive Size: 0.035’’ Quantity: 15

Table I.2: Part List and Description of Mainspring with Going Barrel

No.	Part	Supplier	Part No.	Description
1.	Spring	N/A	N/A	Material: Steel Thickness: 0.0035’’ Width: 0.235’’ Length: 42.5’’ Spring Rate: 6.95e-05 Nm/rad
2.	Barrel			Drum Diameter: 2.15’’ Barrel Gear Teeth: 102 Barrel Gear Radius: 2.20’’ Barrel Gear Pitch: 72

Table I.3: Description of the DC Micro Generator

No.	Part	Supplier	Part No.	Description
3.	Mechanical	eBay	ESCAP SR 581 A1	Internal Gear Ratio: 4.7:1 Shaft Outer Length: 0.125’’ Gear Pressure Angle: 20° Gear Teeth: 102
	Electrical			Rated Voltage: 1.5 V Rated Current: 20 mA Torque Constant: 6e-03 Vm/rad Voltage Constant: 7.6e-03 Vs/rad Internal Resistance: 1 Ω

Table I.4: Parts List for Encoder Circuit Components

No.	Part	Supplier	Part No.	Description
1.	IR LEDs	Amazon - SUNKEE	B00XPSIT3O	Type: Emitter-Collector Forward Voltage: 1.2-1.3V Wavelength: 940 nm Diameter: 0. 197’’ Quantity: 1
2.	Op-Amp	Texas Instruments	LM 741	Power Rating: 80 - 150mW Supply Voltage: 22 Input Voltage: 15 Current: 1.7 - 2.8mA Quantity: 1

Table I.5: Parts List of Supplementary Items

No.	Part	Supplier	Part No.	Description
1.	Gear G_8	Stock Drive Products and Sterling Instrument	S1063Z-072A048	Material: Aluminium Hub: Pin Hub Radius: 0.675’’ Pitch: 72 Pressure Angle: 20° Teeth: 48 Bore Diameter: 0.125’’ Hub Diameter: 0.312’’ Face Width: 0.125’’ Quantity: 2
2.	Retaining Rings	Amazon Supply	SH-12St PA (B006209X24)	Material: 1060-1090 Carbon Steel Phosphate Finish Outer Diameter: 0.135’’ Thickness: 0.010’’ Shaft Diameter: 0.125’’ Groove: 0.004’’ Groove Diameter: 0.117 Quantity:30

3.	Cap Screws	Amazon Supply	B005A0OENO	Material: Alloy Steel Zinc Plated Thread Type: UNC, Class 2A, Fully Threaded Size: 5-40 Length: 0.75’’ Head Diameter: 0.217’’ Head Height: 0.118’’ Quantity: 30
4.	Plate	McMaster-Carr	9057K127	Material: Aluminium Width: 6’’ Thickness: 0.125’’ Length: 12’’ Quantity: 1
5.	Insert Block	McMaster-Carr	8741K32	Material: Acetal Thickness: 1/4" Width: 1/4" Length: 1' Quantity: 1
6.	Adhesive	McMaster-Carr (Loctite)	7560A54	Acrylic structural adhesive Aerosol 7387 activator
7.	LED	Amazon	H&PC-54378 B005ONQ41W	Color: White Wattage: 1W Diameter: 0.197’’ Forward Voltage: 3.3 V Current: 30 mA

8.	DAQ	National Instruments	776844-01	NI SCB 68 Noise Rejecting, Shielded I/O Connector Block 0.125’’ Flathead Pins Power Supply: 5V – 30V

Table I.6: Parts List for Machining Tools

No.	Part	Supplier	Part No.	Description
1.	Internal Lathe Tool for Retaining Rings	McMaster-Carr	32335A82	Material: Carbide Groove: 0.017" Min Hole Diameter: 1/4" Max Hole Depth: 0.63" Offset: 0.05" Shank Type: Round Shank Diameter: 1/4" Length: 2-1/2" Quantity: 2

2.	End Mill	McMaster-Carr	3049A46	Material: High-Speed Steel Double Ended, Two Flute Center Cutting, Square End Mill Diameter: 0.281" Shank Diameter: 0.375" Cut Length: 0.563" Length: 3.125" Helix Angle: 30° Quantity: 1
3.	Through-Hole Threading Machine Tool Tap	McMaster-Carr	2726A-38	Double Flute Material: High-Speed Steel Titanium Nitride Coating Thread Size: 5-40 Thread Length: 0.625" Length: 1.06" Drill Bit Size: 38 Quantity: 2

REFERENCES

1. J. Conti, H. Paul, J. Diefenderfer, A. LaRose, J.T. Turnure, and L. Westfall, "International Energy Outlook 2016 With Projections to 2040", doi: 10.2172/1296780, United States, May 2016.

2. REN21, "Renewables 2016 Global Status Report", REN21 Secretariat, Paris, ISBN 978-3-9818107-0-7, June 2016.

3. S. Sojan and R.K. Kulkarni, "A Comprehensive Review of Energy Harvesting Techniques and its Potential Applications", *International Journal of Computer Applications*, vol. 139, no. 3, pp. 14-19, April 2016.

4. J. Paulo and P.D. gaspar, "Review and Future Trends of Energy Harvesting Methods for Portable Medical Devices", proceedings of the World Congress on Engineering, vol. 2, pp. 978-988, UK, June-July 2010.

5. IDTechEx,"Energy Harvesting", Available: http://www.idtechex.com/reports/topics/energy-harvesting-000007.asp, accessed: July 2016.

6. V. Bhatnagar and P. Owende, "Energy Harvesting for Assistive and Mobile Applications", *Energy Science and Engineering*, vol. 3, issue 3, pp. 153-173, May 2015.

7. Y. K. Tan and S. K. Panda, "Review of energy harvesting technologies for sustainable wireless sensor network in sustainable wireless sensor networks," Available: http://cdn.intechopen.com/pdfs/12418/InTech-Review_of_energy_harvesting_technologies_for_sustainable_wsn.pdf, accessed: January 2017.

8. Y. Li and R. Shi, "An Intelligent Solar Energy-harvesting System for Wireless Sensor Networks", *EURASIP Journal on Wireless Communications and Networking*, vol. 2015, no. 1, pp. 1-12, December 2015.

9. L. Li, X. Mu, W. Liu, Z. Mi, and C. Li, "Simple and Efficient System for Combined Solar Energy Harvesting and Reversible Hydrogen Storage", *Journal of American Chemical Society*, vol. 137, no. 24, pp. 7576-7579, June 2015.

10. S.K. Cushing and N. Wu, "Progress and Perspectives of Plasmon-Enhanced Solar Energy Conversion", *Journal of Physics Chemistry Letters*, vol. 7, no. 4, pp. 666-675, January 2016.

11. S. Roundy and P. Wright, “Energy Scavenging for Wireless Sensor Networks With Special Focus on Vibrations”, New York: Kluwer Academic Publishers, 2004.

12. D. Shen, “Piezoelectric Energy Harvesting Devices for Low Frequency Vibration Applications”, Doctoral Dissertation, Auburn University, May 2009.

13. B. Cavalier, P. Berthelot, H. Nouira, E. Foltete, L. Hirsinger, and S. Ballandras, “Energy Harvesting using Vibrating Structures Excited by Shock”, proceedings of the IEEE Ultrasonic Symposium, pp. 943-945, doi: 10.1109/ULTSYM.2005.1603006, Netherlands, September 2005.

14. J. M. Nelson, “Using Piezoelectric Generation to Harvest Energy from Turbulent Air Flow”, Master’s Thesis, Purdue University, May 2010.

15. M.J. Ramsey and W.W Clark, “Piezoelectric Energy Harvesting for Bio MEMS Applications”, proceedings of SPIE’s 8th Annual Smart Materials and Structures Conference, vol. 4332, pp. 429-438, CA, June 2001.

16. E. H. Callaway, Jr, “Wireless Sensor Networks – Architectures and Protocols”, Auerbach Publications: Boca Raton, FL, 2004.

17. S. Kim, S. Priya, and I. Kanno, “Piezoelectric MEMS for Energy Harvesting”, *MRS Bulletin*, vol. 37, no. 11, pp. 1039-1050, November 2012.

18. D. Guyomar and M. Lallart, “Recent Progress in Piezoelectric Conversion and Energy Harvesting Using Nonlinear Electronic Interfaces and Issues in Small Scale Implementation”, *Micromachines*, vol. 2, no.2, pp. 274-294, June 2011.

19. K. Makihara, Y. Yamamoto, K. Yoshimizu, C. Horiguchi, H. Sakaguchi, and K. Fujimoto, “A Novel Controller to Increase Harvested Energy from Negating Vibration-supression Effect”, *Smart Materials and Structures*, vol. 24, no. 3, pp. 037005, February 2015.

20. S. Chalasani and J. Conrad, “A Survey of Energy Harvesting Sources for Embedded Systems”, proceedings of IEEE SouthEastCon, pp. 442-447, Huntsville, AL, April 2008.

21. S. Boisseau, G. Despesse, and B. Ahmed Seddik, “Electrostatic Conversion of Vibrational Energy Harvesting, Small-Scale Energy Harvesting”, M. Lallart (Ed.), Intech, doi: 10.5772/51360, October 2012.

22. F.Wang and O Hansen, “Electrostatic Energy Harvesting Device with Out-of-plane Gap Closing Scheme”, *Sensors and Actuators A: Physical*, vol. 211, pp. 131-137, May 2014.

23. K. Tao, J. Wu, L. Tang, L. Hu, S.W. Lye, and J. Miao, "Enhanced Electrostatic Vibrational Energy harvesting using Integrated opposite-charged Electrets", *Journal of Micromechanics and Microengineering*, vol. 27, no. 4, pp **, March 2017.

24. F. Yildiz, "Potential Ambient Energy-Harvesting Sources and Techniques", *Journal of Technology Studies*, vol. 35, no. 1, pp. 40-48, September 2009.

25. B. Yang, C. Lee, W. Xiang, J. Xie, J.H. He, R.K. Kotlanka, S.P. Low, and H. Feng, "Electromagnetic Energy Harvesting from Vibrations of Multiple Frequencies", *Journal of Micromechanics and Microengineering*, vol. 19, no. 3, pp 1-8, March 2009.

26. V. Gupta, A. Kandhalu, and R. Ragunathan, "Energy Harvesting from Electromagnetic Energy Radiating from AC Power Lines", proceedings of the 6th Workshop on Hot Topics in Embedded Networked Sensors, vol. 10, no. 17, pp. 1-6, Ireland, June 2010.

27. H. Zhang, Y. Xie, X. Li, Z. Huang, S. Zhang, Y. Su, B. Wu, L. Hu, W. Yang, and Y. Lin, "Flexible Pyroelectric Generators for Scavenging Ambient Thermal Energy as Self-powered Themosensors", *Energy*, vol. 101, no.1, pp. 202-210, April 2016.

28. H. Wahid and H.A. Rahim, "A Review of Thermoelectric Energy Harvesters and Its Power Management Approach in Electronic Applications", *Journal Teknologi*, doi: 10.11113/jt.v73.4261, March 2015.

29. P. Wolas, "Thermoelectric Energy Harvesting from Small and Variable Temperature Gradients", proceedings of the Dresdner Sensor-Symposium 2015, vol. 12, pp. 83-88, December 2015.

30. Z.Yang, J. PradoGonjal, M. Phillips, S. Lan, A. Powell, P. Vaqueiro, M. Gao, R. Stobart, and R. Chen, "Improved Thermoelectric Generator Performance Using High Temperature Thermoelectric Materials", proceedings of the SAE World Congress Experience 2017, doi:10.4271/2017-01-0121, MI, USA, April 2017.

31. W. Zhu, Y. Deng, Y. Wang, S. Shen, and R. Gulfam, "High-performance Photovoltaic-thermoelectric Hybrid Power Generation System with Optimized Thermal Management", *Energy*, vol. 100, no.1, pp. 91-101, April 2016.

32. V. Leonov, "Thermoelectric Energy Harvesting of Human Body Heat for Wearable Sensors", *IEEE Sensors Journal*, vol. 13, no. 6, pp. 2284-2291, June 2013.

33. F. Zhang, Y. Zhang, J. Silver, Y. Shakhsheer, M. Nagaraju, A. Klinefelter, J.N. Pandey, J. Boley, E.J. Carlson, A. Shrivatsava, B.P. Otis, and B.B.H. Calhoun, "A Battery-less 19 μW MICS/ISM-band Energy Harvesting Body Area Sensor Node SoC", proceedings of the IEEE International Solid State Circuits Conference Digital Tech. Ppaers, pp. 298-300, CA, USA, February 2012.

34. V. Leonov, T.Torfs, N. Kukhar, C. Van Hoof, and R. Vullers, "Small-size BiTe Thermophiles and a Thermoelectric Generator for Wearable Sensor Nodes", proceedings of the 5th European Conference on Thermoelectrics, pp. 76-79, Ukraine, September 2007.

35. D. Moline and J. Wagner, "Operating Principles, Common Questions, and Performance Data for an Atmospheric Driven Atmos Clock", *NAWCC Bulletin – National Association of Clock and Watch Collectors In.*, vol. 57/1, no. 413, January 2015.

36. S. Patel, D. Moline, and J. Wagner, "Modeling and Analysis of Atmospheric Driven Atmos Clock with Mechanical Escapement Control", Proceeding of the European Control Conference, Zurich, Switzerland, pp. 281-287, July 2013.

37. G. Ali, J. Wagner, and T. Schweisinger, "Energy Harvesting from Atmospheric Temperature Variations – Theory and Test", *Renewable Energy*, vol. 74, no.14, pp. 528-535, August 2014.

38. C. Zhao, S. Yisrael, J. Smith, and S. Patel, "Powering Wireless Sensor Nodes with Ambient Temperature Changes", proceedings of UBICOMP'14, Seattle, WA, pp. 383-387, September 2014.

39. J. Wenck, J. Collier, J. Siebert, and R. Amirtharajah, "Scaling Self-Timed Systems Powered by Mechanical Vibration Energy Harvesting", *ACM Journal on Emerging Technologies in Computing Systems*, vol. 6, no. 2, Article 5, pp. 1-24, June 2010.

40. M. A. Weimer, T. S. Paing, and R. A. Zane, "Remote Area Wind Energy Harvesting for Low-power Autonomous Sensors", proceedings of the IEEE Power Electronics Specialist Conference, Jeju, South Korea, pp. 18–22, June 2006.

41. E. Sardini and M. Serpelloni, "Self-Powered Wireless Sensor for Air Temperature and Velocity Measurements With Energy Harvesting Capability", *IEEE Transactions on Instrumentation and Measurement*, vol. 60, no. 5, pp. 275-280, May 2011.

42. E. Cantatore and M. Ouwerkerk, "Energy Scavenging and Power Management in Networks of Autonomous Micro-sensors", *Microelectronics Journal*, vol. 37, issue 12, pp. 1584–1590, August 2006.

43. J. Lebet, "Living on Air: History of the Atmos Clock.", Jaeger-LeCoultre: Switzerland, 1997.

44. Anonymous, "The Atmos Clock", *The Horological Journal*, pp.14, 16, 56, 58, May and June 1934.

45. P. D. Mitcheson, P. Miao, B. H. Stark, E. M. Yeatman, A. S. Holmes, and T. C. Green, "MEMS Electrostatic Micro-power Generator for Low Frequency Operation", *Sensors and Actuators A: Physical*, vol. 115, no. 2-3, pp. 523-529, 2004.

46. E. Martt, "The Atmos Clock Ethyl Chloride as the Bellows Gas", National Association of Watch and Clock Collectors, Chapter #161, *Horological Science Newsletter*, issue 3, pp. 16, May 1998.

47. E. W. Otto, "Analysis of Gas-filled Bellows for Sensing Gas Density", *National Advisory Committee for Aeronautics*, Technical Note, no. 1538, March 1948.

48. H. Feng, Y. Song, Z. Zuo, J. Shang, Y. Wang, and A. P. Roskilly, "Stable Operation and Electricity Generating Characteristics of a Single-Cylinder Free Piston Engine Linear Generator: Simulation and Experiments", *Energies Journal*, vol. 8, no. 2, pp. 765-785, January 2015.

49. L. Riedel, "Eine neue universelle Dampfdruckformel Untersuchungen über eine Erweiterung des Theorems der übereinstimmenden Zustände. Teil I", *Chemie Ingenieur Technik 26*, pp. 83-89, doi:10.1002/cite.330260206, February 1954.

50. D. Paul, 'Thermoelectric Energy Harvesting", *ICT - Energy - Concepts Towards Zero - Power Information and Communication Technology*, Edited by G.Fagas, L.Gammationi and G.A.Berini, Chapter 4, INTECH, DOI: 10.5772/55410, February 2014.

51. J. Wang, "Potential Applications of Thermoelectric Waste Heat Recovery in the Automotive Industry", proceedings of the IEEE International Conference on Thermoelectrics, Clemson, SC, pp. 170-174, June 2005.

52. S. Ulukus, A. Yener, E. Erkip, O.Simeone, M. Zorzi, P. Grover, and K. Huang, "Energy Harvesting Wireless Communications: A Review of Recent Advances", *IEEE Journal on Selected Areas in Communication*, vol. 33, no. 3, pp. 360-381, March 2015.

53. Idtechex.com, "Energy Storage", Available: http://www.idtechex.com/research/topics/energy-storage.asp, accessed: July 2016.

54. Idtechex, "Thermoelectric Energy Harvesting 2016-2026", Available: http://www.idtechex.com/research/reports/thermoelectric-energy-harvesting-2016-2026-000473.asp, accessed: July 2016.

55. M. Raju and M. Grazier, "Energy Harvesting ULP Meets Energy Harvesting: A Game Changing Combination for Design Engineers", Texas Instruments white paper, SLYY018A, Texas, April 2010.

56. C. Gayner and K. Kar, "Recent Advances in Thermoelectric Materials", *Progress in Material Science*, vol. 83, pp. 330-382, October 2016.

57. F. Yildiz and K. Coogler, "Low Power Energy Harvesting with a Thermoelectric Generator through an Air Conditioning Condenser", proceedings of the 121st ASEE Annual Conference, paper ID 10552, Indianapolis, IN, June 2014.

58. M.M Kenisarin, "High Temperature Phase Change Materials for Thermal Energy Storage", *Renewable and Sustainable Energy Reviews*, vol. 14, issue 3, pp. 955-970, April 2010.

59. A. Gil, M. Medrano, I. Martorell, A. Lazaro, P. Dolado, B. Zalba, and L.F. Cabeza, "State of the Art on High Temperature Thermal Energy Storage for Power Generation. Part 1 – Concepts, Materials and Modellization", *Renewable and Sustainable Energy Reviews*, vol. 14, issue 1, pp. 31-55, January 2010.

60. B. Zalba, J.M. Marin, L. Cabeza, and H. Mehling, "Review on Thermal Energy Storage with Phase Change: Materials, Heat Transfer Analysis and Applications", *Applied Thermal Engineering*, vol. 23, issue 3, pp. 251-283, February 2003.

61. H. Im, T. Kim, H. Song, J. Choi, J. Park, R. Ovalle-Robles, H. Yang, K. Kihm, R. Baughman, H. Lee, T. Kang and Y. Kim, "High-efficiency Electrochemical Thermal Energy Harvester Using Carbon Nanotube Aerogel Sheet Electrodes", *Nature Communications*, article no. 10600, 2016.

62. S. Ganesh, G. Ali, D. Moline, T. Schweisinger, and J. Wagner, "Conversion of Low Frequency Temperature Variations into Electric Power – Design and Analysis of a Mechanical Driven Generator System", submitted to *Renewable Energy*, May 2017.

63. D. Salernon, "Ultralow Voltage Energy Harvester Uses Thermoelectric Generator for Battery-free Wireless Sensors", *Linear Technology Journal of Analog Innovation*, vol. 20, no. 3, pp. 1-11, October 2010.

64. National Center for Biotechnology Information, PubChem Compound Database; CID=6337, Available: htps://pubchem.ncbi.nlm.nih.gov/compound/6337, accessed: February 2017.